The effects of interfaces on the magnetic properties of ultra-thin ferromagnetic films

Inauguraldissertation

zur

Erlangung der Würde eines Doktors der Philosophie

vorgelegt der

Philosophisch-Naturwissenschaftlichen Fakultät

der

Universität Basel

von

Sridhar Reddy Avula Venkata

aus Hyderabad, Indien

Basel, 2018

Originaldokument gespeichert auf dem Dokumentenserver der Universität Basel

edoc.unibas.ch

Genehmigt von der Philosophisch-Naturwissenschaftlichen Fakultät auf Antrag von

Fakultätsverantwortlicher: Prof. Dr. Frithjof Nolting
Korreferent: Prof. Dr. Arantxa Fraile Rodríguez

Basel, den 24.04.2018

Prof. Dr. Martin Spiess
Dekan

Abstract

In this dissertation, the manipulation of the magnetic properties of ultra-thin ferromagnetic (FM) films by varying the interfacial coupling on both sides of the film, e.g. with the capping layer and with the substrate, has been studied by means of X-ray absorption spectroscopy (XAS) and X-ray magnetic circular dichroism (XMCD).

Firstly, XAS and XMCD measurements were carried out at the Fe $L_{2,3}$ absorption edges of an ultra-thin iron wedge grown on a ferroelectric $[Pb(Mg_{1/3}Nb_{2/3})O_3]_{0.68}$-$[PbTiO_3]_{0.32}$ (PMN-PT) (001) substrate using the total electron yield mode. Upon switching the ferroelectric polarization of the substrate from P_{up} to P_{down}, we observe a strong change of approximately 20% of the Fe total magnetic moment for a film thickness of 1.5 *nm*. However, when the dimensionality of the system increases, i.e. for a film thickness of 3 *nm*, the same FE polarization only weakly affect the Fe magnetic moments. Taking the sampling depth of the measurement method into account, this difference is compatible with a magnetic anisotropy change taking place only in the first interfacial layer in contact with the ferroelectric substrate. We attribute this interfacial coupling to a charge accumulation or depletion at the interface. Similar measurements were carried out for different systems such as Pd/Fe/PMN-PT system in which the 3 *nm* Cr capping was replaced by the 3 *nm* Pd capping. In this heterostructure system, we did not observe a strong anisotropy for P_{up} as the remanent moments are observed along both the in-plane

and out-of-plane directions. Upon switching the FE polarization of the PMN-PT to down in Pd/Fe/PMN-PT system, the remanence magnetic moments increase along the in-plane direction while they decrease along the out-of-plane direction. Further, we report an increase in the saturation moments for the Pd/Fe/PMN-PT system compared to the bcc Fe.

In order to gain further insight into the magnetic properties at the interface between oxides and metals, we investigated ultra-thin films of 1.2 *nm* thickness $Co_{40}Fe_{40}B_{20}$ (CoFeB), using the XMCD technique, by probing at the Fe and Co $L_{2,3}$ absorption edges. Systems with different oxide interfaces such as Ta/CoFeB/MgO, Ta/CoFeB/$BaTiO_3$ (BTO) and Ta/CoFeB/$Ba_{0.1}Sr_{0.9}TiO_3$ (BSTO) samples have been investigated. For the CoFeB/MgO system, the XMCD measurement revealed that magnetization along in-plane and out-of-plane direction are similar, i.e., the system is very isotropic. However, when the same thickness of CoFeB is grown on BSTO and BTO substrates, the easy axis of the magnetization aligns along the in-plane direction. The magnetic moments for Fe and Co shown by all the three systems are less than the bulk bcc Fe and bulk hcp Co, which is attributed to a dead layer at the CoFeB/Ta interface. We also report an enhancement in the orbital moments for Fe and Co atoms in comparison to bulk bcc Fe and bulk hcp Co due to the interface with different oxides.

Lastly, the effect of capping layers of Tantalum (Ta), Platinum (Pt) and Ruthenium (Ru) on the CoFeB/MgO system has been studied. The Ta/CoFeB/MgO system shows an isotropic behavior, while the Pt/Ru capped/CoFeB/MgO systems show an in-plane magnetization. The Fe and Co magnetic moments were calculated using the XMCD sum rules, in which we clearly observed the change in moments among the three systems. Pt/CoFeB/MgO system shows an increase in the magnetic moments of Fe and Co atoms as compared to the Ta/CoFeB/MgO system. On the other hand, Ru/CoFeB/MgO system shows a decrease in the Fe moments

as compared to Ta/CoFeB/MgO. The Pt/CoFeB/MgO system shows Co moments similar to the bulk hcp Co. XAS spectra at the Fe and Co $L_{2,3}$ edges, show a shift in the energy of the XAS peak when capped with Pt and Ru in comparison to Ta capped films. In addition the Ru/CoFeB/MgO systems shows a shoulder at the Fe L_3-edge due to the interaction of Ru and Fe orbitals. Whereas, the Pt/CoFeB/MgO system shows a shift of the Co L_3-edge to lower energy in comparison to the Ta/CoFeB/MgO system which can be the result of interaction between Pt and Co orbitals.

Contents

List of Abbreviations

AFFE	antiferromagnet ferroelectric
AFM	antiferromagnet
bcc	body centered cubic
BFO	$BiFeO_3$
BSTO	$Ba_xSr_{1-x}TiO_3$
BTO	BaTiO3
CoFeB	$Co_{40}Fe_{40}B_{20}$
hcp	hexagonal close packed
FE	ferroelectric
FM	ferromagnet
IL	interfacial layer
J_{ex}	exchange integral
LSMO	$La_{0.8}Sr_{0.2}MnO_3$
ML	monolayer
MOKE	magneto-optic Kerr effect
MPB	morphotropic phase boundary
MTJ	magnetic tunnel junction
PMA	perpendicular magnetic anisotropy
PMN-PT	$[Pb(Mg_{1/3}Nb_{2/3}O_3]_{(1-x)}$-$[PbTiO_3]x$
PZT	$PbZrTiO_3$

SQUID	superconducting quantum interference device
STM	scanning tunnel microscopy
T_c	curie temperature
TEY	total electron yield
TFY	total fluorescence yield
TL	top layer
UHV	ultra high vacuum
XAS	X-ray absorption spectra
XMCD	X-ray magnetic circular dichroism

1 Introduction

In the present world, the ambition to develop new functional devices is ever increasing. These devices have to be miniaturized, energy efficient and enduring for present and future applications in many different areas of technology. In the process of advancing technology, new scientific breakthroughs have been made. Such breakthroughs can be found in the field of magnetism at smaller dimensions. Ultra thin magnetic films are key constituents of magnetic tunnel junctions (MTJ) in magnetic sensors and memory elements.

Modern growth techniques such as e-beam evaporation, magnetron sputtering and pulsed laser deposition make it possible to develop ultra-thin magnetic films, whereby the limit is of the order 20-30 monolayers [1]. In ultra-thin films the surface or interface is dominant over the bulk leading to new magnetic properties. However, the underlying mechanisms leading to such new properties are still unclear which provides an interesting opportunity to explore the physics of ultra-thin magnetic films. To understand the physical origin of the film properties, it is important to understand the magnetic properties (magnetic anisotropy, spin and orbital moments) of the individual elements present in the magnetic materials. By using X-ray absorption spectroscopy (XAS), it is possible to explore for each element its contribution to the properties of the material. XAS spectra are element specific and electronic properties of the elements can be investigated [2]. The magnetic properties of the magnetic material can be determined by X-ray magnetic circular

dichroism, which is the difference between oppositely circularly polarized XAS [3].

This thesis focuses on the basic understanding of the physical origin of the magnetic properties in ultra-thin magnetic materials when they are coupled to an oxide and/or metal interface. To interpret the properties of ultra-thin films, this thesis targets three main questions. (i) Is it possible to modify the ferromagnetic (FM) properties of the ultra-thin films by switching the ferroelectric (FE) polarization at the FM/FE interface? (ii) How do the magnetic properties change in ultra thin magnetic films by having an interface with different oxides? and (iii) What happens to the magnetic properties, when the ultra-thin magnetic films have an interface with various metals?

The properties of ultra-thin magnetic films can be controlled using an electric field. One example is artificial multiferroics, where a ferromagnet (FM) and ferroelectric (FE) are coupled through a interface, leading to interaction of magnetic and electric polarizations. This coupling is magnetoelectric, where the magnetic properties can be controlled by electric field and vice versa [4]. Most of the FE materials are oxides with a pervoskite structure such as Barium titanate ($BaTiO_3$), lead zirconate ($PbTiO_3$), and lead magnesium niobate- lead titanate (PMN-PT) etc. Controlling magnetic properties of a FM with a pervoskite oxide is very interesting and complex process. By application of an electric field, the pervoskite FE oxide induces a strain or charge or interfacial exchange bias on the FM leading to modification of magnetic properties. Valencia *et al.* [5] demonstrate that the spin polarization of ultra-thin Fe and Co films (2 *nm* thin) having an interface with BTO can be controlled by FE polarization. In the first part of this thesis, the change in magnetic properties of ultra-thin Fe films ($0.3 - 3$ *nm*) by switching the FE polarization of PMN-PT is addressed. By measuring the XMCD signal at different thicknesses of the wedge, the change in magnetic moments of ultra-thin Fe films with FE polarization is elucidated.

In 3*d* transition metals, spin orbit coupling (SOC) exists, which is of growing interest due to spin-orbit effects when layers are brought together in a device. SOC depends on the coupling strength between spin and orbital moments and also on the size of the spin and orbital moments. SOC is small for ultra-thin magnetic films as the orbital moment is quenched and it changes depending upon the interfaces. One such example is perpendicularly magnetized ultra thin magnetic film deposited on oxide film. Monso *et al.* [6] first demonstrated the interfacial perpendicular magnetic anisotropy (PMA) at the interface between ferromagnets (CoFe) and oxides. Ikeda *et al.* [7] developed a MTJ of CoFeB with MgO as tunnel barrier which shows a PMA and has high thermal stability, low current for switching and large TMR effect. Since then lots of works have been carried out to understand the origin of PMA in CoFeB/MgO systems [8, 9]. In the second part of this thesis, the influence of the interface with different oxides on the PMA of CoFeB is studied by measuring the magnetic moments of Fe and Co atoms using XMCD.

The capping layer on the CoFeB/MgO system has a strong influence on the PMA and magnetoresistance as reported by previous works [10, 11, 12]. Ta is the most common capping metal used to obtain PMA in CoFeB/MgO system. In the last part of this thesis, the effect of Ru and Pt capping is shown on the PMA in CoFeB/MgO by comparing it to the Ta/CoFeB/MgO system. The effect of capping layers on the moments of Fe and Co atoms and on the electronic state of Fe and Co atoms are elucidated.

The thesis structure is as follows:

Chapter 2: In this chapter, the properties of the materials used in this thesis are discussed with a brief introduction to different mechanisms in artificial multiferroics. The factors responsible for PMA in CoFeB/MgO systems are briefly discussed.

Chapter 3: A theoretical basis of XAS and XMCD including the data analysis are explained. The different sample growth techniques and experimental set-ups to

characterize the grown samples are discussed in this chapter.

Chapter 4: The magneto-electric coupling between ultra-thin Fe films and PMN-PT is studied. Here, the change in the magnetic anisotropy of Fe by FE polarization at the Fe/PMN-PT is shown. This change in anisotropy is attributed to the charge modulation at the interface.

Chapter 5: This chapter discusses the effect on the magnetic properties of CoFeB with an interface to different oxides. The magnetic moments of Fe and Co atoms of CoFeB on BTO and $BaSrTiO_3$ (BSTO) are compared to the corresponding moments of CoFeB/MgO.

Chapter 6: The effect of Ta, Ru and Pt capping layers on the magnetic properties of CoFeB/MgO system is investigated. We show that Ru reduces the magnetic moments of Fe and Co atoms, whereas Pt increases the moments of Fe and Co atoms as compared to the Ta capped/CoFeB/MgO system. The XAS spectra at the Fe and Co edges, show a shift in the energy for Pt capping.

Chapter 7: A summary of the main results is given.

2 Materials and their characteristic properties

Understanding the interfacial coupling between ferromagnetic materials and different oxides is important for the development of new materials and combination of materials for device applications. To pursue the development of interfacial coupling, materials have to be chosen which show characteristic properties: ferromagnetic (FM) materials, ferroelectric (FE) materials and materials having perpendicular magnetic anisotropy (PMA). In order to manipulate magnetism by using ferroelectricity, an in-depth understanding of the underlying mechanisms is necessary. It is also essential to interpret the physical origin of PMA in different magnetic materials.

This chapter is dedicated to a brief introduction to the materials used in this thesis to understand the aforesaid physical phenomena. As interfacial effects lead to different properties of ferromagnets, a short introduction about ferromagnetism is given in section 2.1 including the various factors contributing to the ground state energy in ferromagnetic materials. This is followed by describing the different contributions to the total magnetic anisotropy. In section 2.2, a brief summary about ferroelectricity is provided with a background on the different ferroelectric materials. Ferroelectric materials used in this thesis are $[Pb(Mg_{1/3}Nb_{2/3})O_3]_{(1-x)} - [PbTiO_3]_x$ (PMN-PT), $BaTiO_3$ (BTO), and $Ba_xSr_{1-x}TiO_3$ (BSTO) which are discussed

in the subsequent section. A synopsis on the topic of artificial multiferroics and the different coupling mechanisms leading to the magnetoelectric coupling between a FM and FE is given in section 2.3. In the last section, an introduction is given to the origin of PMA in the CoFeB/MgO system, and the factors responsible for PMA are reviewed.

2.1 Ferromagnetism

Ferromagnetic materials are characterized by spontaneous magnetization, which is caused by the long range ordering of the magnetic moments. The magnetic moment is associated with the electron's spin and orbital motion. Weiss postulated that within ferromagnetic materials a molecular field exists that orders the magnetic moments against the thermal motion and in the demagnetized state, the ferromagnetic material is divided into magnetic domains [13]. Heisenberg took a step forward to explain the microscopic origin of the molecular field using laws of quantum mechanics by exchange interaction. When two neighboring atoms overlap, it leads to the correlation of electrons which results in exchange interaction [14]. The exchange interaction depends on the spin orientation localized on the neighboring atoms. Exchange interaction is responsible for parallel alignment of spins (ferromagnetic) and antiparallel alignment of spins (antiferromagnetic) and can be described by the Heisenberg exchange Hamiltonian:

$$H = -\Sigma J_{ex} \mathbf{S}_a . \mathbf{S}_b \tag{2.1}$$

where J_{ex} is the exchange integral and $\mathbf{S}_a, \mathbf{S}_b$ are atomic spins. Direct exchange interaction between two neighboring spin moments arises due to overlap between the magnetic orbitals of two atoms close to each other. Direct exchange interaction is strong for $3d$ metals due to their large $3d$ electron cloud. Slater [15, 16] found

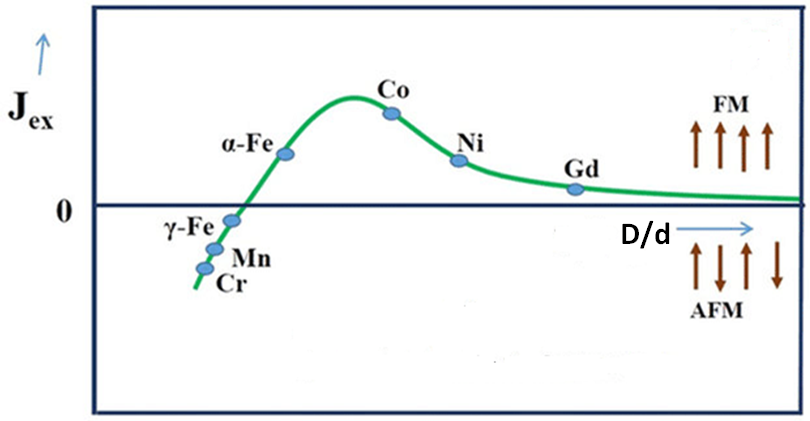

Figure 2.1 Bethe-Slater diagram showing the change in J_{ex} with increase in the atomic number for the 3*d* transition metals. Figure take from [19].

the interplay between J_{ex} and D/d which is depicted by Bethe-Slater diagram as shown in Fig. 2.1, where D is atomic separation of the interacting atoms and d is the diameter of the interacting d orbitals. From Fig. 2.1 it can be seen that J_{ex} can have either positive sign i.e. parallel alignment of spin or negative sign i.e. antiparallel alignment depending on D (orbital overlap). Direct exchange is a short-range interaction. When D is too large the overlapping of the orbitals is too weak and the direct exchange coupling is not strong enough to overcome the thermal excitations leading to paramagnetism. Of all of the 3d transition metals, only Fe, Co and Ni have positive J_{ex}, making them ferromagnetic 3d transition elements [17]. Above the Curie temperature (T_c), the ferromagnetic ordering is overcome by thermal fluctuations and below T_c the magnetic moments align due to exchange interactions [18].

In the following section, an overview of the different energy contributions in ferromagnetic materials such as exchange, magnetostatic and anisotropy energies are reviewed.

2.1.1 Exchange Energy

The exchange energy is a short range interaction, and results in the adjacent magnetic moments aligning parallel to each other in the ferromagnetic materials. The exchange energy density (E_x (m(r))) arises from the exchange interaction and is expressed by the following equation:

$$E_x(m(r)) = A((\nabla m_x)^2 + (\nabla m_y)^2 + (\nabla m_z)^2) \tag{2.2}$$

where $m(r)$ is the ratio of remanence magnetization (M_r) to saturation magnetization (M_s), and A is the exchange stiffness constant. The exchange energy is an isotropic quantity as it depends only on the angle between neighbor magnetic moments and not on the crystallographic axis.

2.1.2 Magnetostatic Energy

Magnetostatic energy originates from the free surface magnetic poles at an interface. When a sample is uniformly magnetized a demagnetizing field is created within the sample and stray fields outside the magnetic material. Magnetostatic energy operates over long range and is dependent on the geometry of the magnetic material. The magnetostatic energy ($E_{m,s}$) density due to the magnetic stray fields at the interface can be expressed as [20]:

$$E_{m,s} = (\frac{\mu_0}{2})H_d M \tag{2.3}$$

where H_d is the anisotropic demagnetizing field, M is the magnetization and μ_0 is the permeability in the free space.

2.1.3 Magnetic Anisotropy

Magnetic anisotropy is the preference for the magnetization to align in a particular direction of the sample. It is the dependence of the internal energy of a system on the direction of the spontaneous magnetization which is termed as magnetic anisotropy energy. The anisotropy energy (E_a) represents the tendency for magnetization to lie along an easy axis and is given by:

$$E_a = K_1 \sin^2 \theta \tag{2.4}$$

where θ is the angle between magnetization (M) and the anisotropy axis. K_1 is the anisotropy constant. Magnetic anisotropy depends on temperature and will be zero at critical temperature (T_c) at zero magnetic field [21].

The main contributions to magnetic anisotropy comes from shape anisotropy, magnetocrystalline anisotropy, magnetoelastic anisotropy and induced anisotropy. In chapter 4, the change in magnetic anisotropy for Fe by switching the ferroelectric polarization is discussed. In chapter 5 and 6, the change in perpendicular magnetic anisotropy (PMA) of CoFeB grown on different oxides and the effect of capping layers on CoFeB/MgO system is examined. In the following discussion, a brief review of shape, magnetocrystalline, induced, magnetoelastic and surface-interface anisotropy is given. The following description is adapted from reference [22].

Shape Anisotropy: The shape anisotropy comes from the long range magnetic dipolar interaction. In non spherical samples (ellipsoidal), the easy magnetization axis has one or more specific directions which are solely caused by the shape. The shape effect of the dipolar interaction in ellipsoidal samples can be described with an anisotropic H_d (anisotropic demagnetizing field) and is given by:

$$H_d = -NM \tag{2.5}$$

Table 2.2 Magneto crystalline anisotropy constants K_1 for Fe, Co, Ni at 4.2 K [24].

	bcc-Fe	fcc-Ni	hcp-Co
$K_1[J/m^3]$	$5.48.10^4$	$-12.63.10^4$	$7.66.10^5$

Here M is the magnetization and N is the shape-dependent demagnetizing tensor. The anisotropy energy density (E_s) is given by [23]:

$$E_s = \frac{1}{2}\mu_0 M_s^2 \cos^2\theta \tag{2.6}$$

Here the magnetization is assumed to be uniform with a magnitude equal to the saturation magnetization M_S, and θ is the angle between magnetization and film normal. For example, Fe has a shape anisotropy of 1.92×10^6 J/m^3 [24] resulting in an in-plane magnetization for thin film systems.

Magnetocrystalline Anisotropy: Spin-orbit interaction of the electrons is the main cause of magnetocrystalline anisotropy. The crystallographic structure is linked to electron orbitals. The spin and angular momentum couple via the electrostatic potential of the charges and it energetically favors the anisotropy to align along a well defined crystallographic axis. Therefore, magnetic materials have preferred directions to magnetize easily, for example bcc Fe has the easy magnetization direction along (001), fcc Ni along (111), and hcp Co along (0001) [25]. Though the magnetocrystalline energy is small compared to exchange energy, the direction of the magnetization is only determined by anisotropy as the exchange interaction just tries to align the magnetic moments parallel, no matter in which direction. The magnetocrystalline anisotropy constant K_1 is given in the table 2.2 for aforesaid crystallographic orientation of Fe, Ni and Co.

Induced Anisotropy: Induced anisotropy is not intrinsic to the material but it is achieved by magnetic annealing which has directional characteristics. There are

other ways to induce anisotropy in a magnetic film, for example by applying a magnetic field during deposition [26]. Prerequisites for induced anisotropy in crystals are a disordered distribution of the atoms in the crystal lattice and a high T_c which allows rapid site exchange processes in the magnetic state. The anisotropy energy density (E_{ind}) for the isotropic system is given by:

$$E_{ind} = -K\cos^2(\theta - \theta_{ann}) \tag{2.7}$$

where K is the anisotropy constant describing the induced magnetic anisotropy leading to a uniaxial alignment and $(\theta - \theta_{ann})$ being the angle between the magnetization during the measurement and during annealing.

Magnetoelastic Anisotropy: Applying strain to the lattice changes the distance between the magnetic atoms leading to change in magnetocrystalline anisotropy and thereby alters the direction of the magnetization. This effect is the inverse of the magnetostriction, the phenomenon by which the sample dimensions change when the direction of the magnetization is altered. The strength of the magnetoelastic anisotropy is proportional to the stress σ and magnetostriction constant λ_s of the material [27]. The energy per unit volume (E_{me}) for isotropic medium i.e. isotropic magnetostriction can be written as:

$$E_{me} = -\frac{3}{2}\lambda_s\, \sigma\, \cos^2\theta_s \tag{2.8}$$

where the angle θ_s measures the direction of the magnetization relative to the direction of uniform stress. Strain in thin films can be induced due to thermal gradients associated with difference in thermal expansion coefficient, intrinsic strain developed by the nature of the deposition process and due to lattice mismatch of the adjacent layers. The sign of λ_s is rather important and it depends on the crystallographic orientation. In the case of Fe, the λ_s along (100) is positive ($24 \times 10^{-6}\ J/m^3$) and along (111) is negative ($-23 \times 10^{-6}\ J/m^3$) [24] which is rather

complex behavior. As the easy magnetization direction for Fe is along (100), a simple dilatation occurs leading to a distortion from a cubic to tetragonal crystal lattice.

Surface and Interface Anisotropy: The above discussed anisotropies for the volume systems neglect interfaces and surfaces. Here, the interface and surface anisotropy for ultra-thin films is discussed. The presence of symmetry-breaking elements are underlying factors for the preferred magnetic moment orientation in ultra-thin magnetic films. By choosing appropriate materials and varying the thicknesses of the individual layers it is possible to tailor magnetic anisotropy. The most striking example is the change of in-plane orientation of the magnetization (commonly observed) to the out of plane direction (perpendicular) to the plane. This phenomenon is called perpendicular magnetic anisotropy (PMA) and is a promising characteristic for applications in storage and magnetic recording devices [23].

The effective magnetic anisotropy energy (K_{eff}) can be separated into a bulk contribution K_b (consisting of the demagnetizing term as well as the magneto-crystalline terms) and interface contribution K_s and can be written as:

$$K_{eff} = K_b + 2K_s/t \tag{2.9}$$

The above expression gives the average magnetic anisotropy energy (MAE) of the interface atoms (present at the surface) and the inner atoms (present in the bulk) of a magnetic layer of thickness t. The second term exhibits an inverse dependence on the t and the factor of two is due to the creation of two surfaces. Therefore, it is only important for thin films.

PMA is purely the magnetic anisotropy which originates from the interface which differs from the magnetic anisotropy in the bulk. In 1954 Néel [28] predicted the lowered symmetry at the surface and interface and called this type of anisotropy

surface or interface anisotropy. The surface anisotropy was first revealed by Gradmann and Müller [29] in 1968 on ultra-thin NiFe films on Cu(111), where 1.8 monolayers (ML) of NiFe shows a PMA and upon increasing the film thickness PMA diminishes. PMA in multilayers was first observed by Carcia *et al.* [30] in the Co/Pd system and later in many other Co-based multilayers: Co/Pt, Co/Au and Co/Ir [31, 32]. Later, PMA was observed in annealed ferromagnetic metal/oxide thin film stacks, such as Pt/CoFe/AlO_x [6] and Ta/CoFeB/MgO [33]. Chapter 5 and 6 of this thesis focuses on understanding the PMA behavior of CoFeB on different substrates and the effect of capping layers. The factors responsible for PMA in the CoFeB/MgO system are discussed in the section 2.4.

2.2 Ferroelectricity

Ferroelectrics are materials which are characterized by spontaneous polarization of the electric charge in the absence of an electric field and the polarization can be switched by applying an external electric field. The spontaneous polarization can occur only in materials which possess a unique polar axis [34]. Ferroelectricity is not an intrinsic property of an atom but it is connected to the structural properties of a material. The mechanism which gives rise to ferroelectricity is due to order-disorder in the system leading to displacements of ions.

The phenomenon of ferroelectricity was first observed in Rochelle salt by Valasek in 1921 [35]. Since then, development of new ferroelectric materials composed of inorganic elements came into the limelight, for example barium titanate ($BaTiO_3$ and the lead zirconate titanate ($Pb[Zr_xTi_{1-x}]O_3$) as they are easy to fabricate and have great ferroelectric properties. These materials exhibit spontaneous polarization over a temperature range and become paraelectric above a critical T_c due to a structural phase transition. Ferroelectrics have their T_c distributed over a wide

range of temperature (e.g. 763 K for $PbTiO_3$ and 393 K for $BaTiO_3$) [36].

The ferroelectric material used in this thesis to investigate the heterostructures discussed in chapter 4 is $[Pb(Mg_{1/3}Nb_{2/3})O_3]_{(1-x)} - [PbTiO_3]_x$ (PMN-PT). In chapter 5, the ferromagnet CoFeB was deposited on the ferroelectrics $BaxSr_{1-x}TiO_3$ and $BaTiO_3$ to understand the interfacial effect on the properties of CoFeB. In the subsequent section a brief introduction about PMN-PT, BTO and BSTO is given.

2.2.1 $[Pb(Mg_{1/3}Nb_{2/3})O_3]_{(1-x)} - [PbTiO_3]_x$ (PMN-PT)

Single crystals of relaxor-ferroelectric solid solutions $[Pb(Mg_{1/3}Nb_{2/3})O_3]_{(1-x)}$ (PMN) – $[PbTiO_3]_x$ (PT) are well-known to be a high performance ferroelectric material. For example the piezoelectric constant (d_{33}) for PMN-32% PT along (001) is 3500pC/N [37]. Pure PMN is a typical relaxor material and PT is a typical ferroelectric material. A relaxor material exhibits a large electrostriction, which means the structure changes with applied electric field. More details about relaxor PMN can be found in this paper [38].

PMN-PT is a complex oxide with pervoskite structure and general formula: ABO_3. In PMN-PT the A site is occupied by Pb^{2+}, B site by Mg^{2+}, Nb^{5+} or Ti^{4+} as shown in Fig. 2.3 (a) [39]. As seen in Fig. 2.3 (a), the B site cations are in the center of the cube surrounded by an oxygen octahedron and the A site cations are located in the space between octahedra. In applied electric field, the two equilibrium orientations of the spontaneous polarization can be switched as shown in Fig. 2.3 (b) and (c).

Pure PMN has a trigonal ferroelectric structure and pure PT has a tetragonal ferroelectric structure at room temperature, which is below the T_c for both materials as shown in Fig. 2.4. The addition of ferroelectric PT strongly affects the host lattice polarizability and in consequence changes the characteristic relaxor behavior of PMN. The Ti from the PT transforms the typical relaxor behavior into the normal

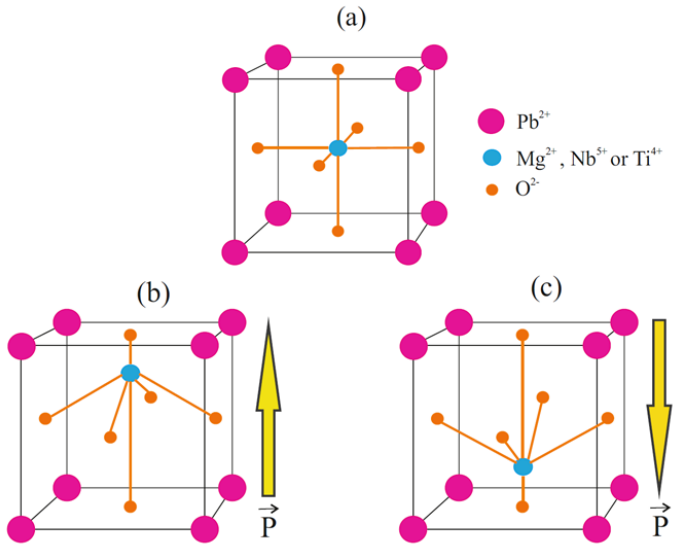

Figure 2.3 A typical pervoskite cubic structure,(a) Pb^{2+} occupying the corners of the cube, Mg^{2+}, Nb^{5+} or Ti^{4+} at the center of the cube surrounded by O^{2-} octahedra. (b) and (c) shows the relative displacement of Ti ions with respect to O^{2-} ions depending on the polarization (P) direction.

ferroelectric leading to several structural phase transitions as a function of x and temperature as seen in phase diagram in Fig. 2.4. The T_c can be changed from 320 K to 500 K by varying the composition of PT ($0 - 50\%$). Fig. 2.4, shows the phase diagram of PMN-PT, which has a morphotropic phase boundary (MPB) between the rhombohedral and tetragonal ferroelectric phases at $x = 31 - 37\%$. At the MPB, the electrical poling field can easily switch between tetragonal and rhombohedral domain states as the free energy of the rhombohedral and tetragonal phases are equal. In PMN-PT, the largest piezoelectric coefficients are observed on the rhombohedral side $x = 0.33$ at the MPB and in single crystals in the (001) direction [40].

In this thesis, PMN-PT with a doping of $x = 0.32$ is used (in the region of MPB) and cut along (001) crystallographic orientation. The PMN-32%PT has a d_{33} of about $3500pC/N$ and T_c of 423 K. The spontaneous polarization for this composition

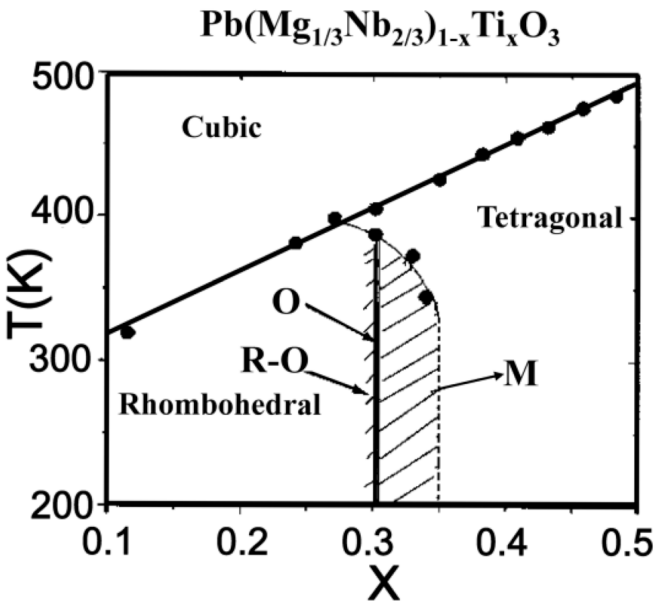

Figure 2.4 PMN-PT phase diagram. The composition of 31-37% PT is the morphotropic phase boundary (MPB). At this composition there is co-existence of monoclinic (M), orthorhombic (O) and rhombohedral (R) phases, where the polarization is high. Figure taken from [41].

and (001) crystallographic orientation is 22.7 μCcm^{-2} [42]. PMN-PT (001) has a rhombohedral structure and has eight possible polarization directions along the (111) directions. Upon applying an electric field, the four polar vectors along the (111) directions incline at an angle of $-54.7°$ from the poling direction and giving rise to an isotropic piezoelectric response in the plane [43, 44].

2.2.2 $BaTiO_3$ (BTO)

$BaTiO_3$ also belongs to the pervoskite family like PMN-PT. In BTO, the Ti^{4+} ion is at the center of the octahedra, Ba^{2+} ions occupy the corners of the cube and O^{2-} ions are at the face-center positions. The spontaneous polarization of BTO at room temperature is 26 μCcm^{-2} [45].

BTO undergoes structural phase changes with temperature. Below a temperature of 393 K, BTO is ferroelectric and it gains an elongation along the c-axis leading to tetragonal structure at room temperature. The spontaneous polarization in BTO is due to the small displacements of the ions which cause a net electric dipole, i.e. the displacement of Ti^{4+} ions with respect to the O^{2-} in the tetragonal BTO unit cell [46]. Above its T_c, BTO is cubic and paraelectric, exhibiting no spontaneous polarization. At 278 K, BTO undergoes a second phase transition from tetragonal to orthorhombic, where the O^{2-} ions are displaced in the direction of the polarization towards the nearest Ti^{4+} ion. The final phase transition from orthorhombic to rhombohedral occurs at 183 K. At this temperature the O^{2-} ions are displaced in the direction of the polarization and the Ti^{4+} ion is displaced anti-parallel.

At room temperature tetragonal BTO exhibits ferroelectric and dielectric properties, which makes it a great material for potential applications [47]. For applications in microelectronics, thin films of BTO are of interest. Recently, ultra-thin BTO films of 3-30 nm thickness have been obtained [48]. The properties of these epitaxially grown ultra-thin films deviate from the bulk. These diverging properties come from the strain and stress within the ultra-thin BTO films, which arises from the interfaces proposed by theoretical studies [49, 50]. The ferroelectric response is modified due to the interface boundary conditions and film thickness and researchers have observed an increase of the coercive electric field for decreasing thickness of BTO [51, 52]. In this thesis chapter 5, the BTO/$SrTiO_3$ (STO) system was used, as BTO can be grown on STO epitaxially due to their lattice mismatch of nearly 3% [53]. Due to lattice mismatch there is lattice deformation leading to large dielectric constant (ε_r = 900 for 2 unit cells of BTO and STO each) compared to the single layer thin films such as BTO and STO [53, 54].

2.2.3 $Ba_x\ Sr_{1-x}\ TiO_3$ (BSTO)

Pervoskite $Ba_x\ Sr_{1-x}\ TiO_3$ is a solid solution of ferroelectric BTO and paraelectric STO. BSTO thin films have a high dielectric constant at room temperature compared to BTO and are thermally stable compared to lead-based ferroelectrics [55, 56]. BSTO thin films have been considered as the most important candidates for development of tunable microwave components due to its high dielectric constant [57, 58]. The T_c of BSTO thin films varies over a broad range depending on the ratio of Ba/Sr in BSTO. Depending on the concentration of Ba in STO, there are changes in electrical and optical properties of BSTO [59, 60]. The BSTO used in this thesis has a composition of $x = 0.10$.

2.3 Artificial Multiferroics

Multiferroic materials are those materials in which more than one ferroic order coexists. However, the term multiferroic usually refers to materials that display coexistence of magnetic and electric order. In these materials coupling between the two (magnetic and electric) ferroic orders can occur which is called magnetoelectric coupling. Due to this coupling, it is possible to control magnetic properties by electric field for device applications like transducers, sensors and magnetic memories [4, 61]. Multiferroics exist in two forms: single-phase multiferroics (intrinsically exhibit more than one ferroic order parameter) and multiferroic heterostructures (artificially created by coupling two ferroic materials through an interface). One approach to achieve multiferroic behavior is by combining ferroelectric and ferromagnetic materials into a heterostructure. The design of artificial multiferroics to manipulate the magnetic state is derived from the concept of ferroelectric field transistors (FET). The control of magnetism with ferroelectrics is both reversible and non-volatile, which is useful for device applications like FET and

multiferroic tunnel junctions (MFTJ). By choosing a wider variety of ferroelectric and ferromagnetic materials, multiferroic heterostructures can be designed by modifying the crystal orientation, lattice strain, electronic state, domain pattern and defect structure at the interface between the ferroic materials [62, 63, 64, 65, 66, 67, 68, 69]. Compared to single-phase multiferroics, the origin of the magnetoelectric coupling in artificial multiferroics is much simpler to address since the origin of the ferroelectric and magnetic order can be dissociated from the coupling mechanism between them, which itself is limited to a smaller number of possibilities: (i) strain transfer (ii) direct (spin) exchange, and (iii) charge coupling [70]. In the following sections, a brief summary of the aforesaid mechanisms in the magnetoelectrically coupled heterostructures is discussed.

2.3.1 Strain Mediated

Modulation of magnetization in artificial multiferroic heterostructures by applying electric field can be realized by means of elastic coupling between a magnetic thin film and a ferroelectric substrate. The lattice structure of the ferroelectric is modified with an electric field which leads to a controllable strain in the adjacent magnetic film as shown in Fig. 2.5. Via inverse magnetostriction, the magnetoelastic energy in the magnetic film is controlled by the electric field. In piezoelectric and ferroelectric materials the nature of strain is quite different. Changes in magnetic order using piezostrain-induced strain are volatile but using the FE the changes induced are non-volatile. Strain transfer coupling using ferroelectric materials has been successfully used to control the magnetic configuration of ferromagnetic properties like magnetic anisotropy, magnetization rotation, and coercivity.

Sahoo *et al.* [71] have experimentally shown the change in the coercive field by interfacial strain transfer of Fe deposited on BTO and it is a good demonstration to show that the magnetic properties of 3*d* transition metal ferromagnetic thin film

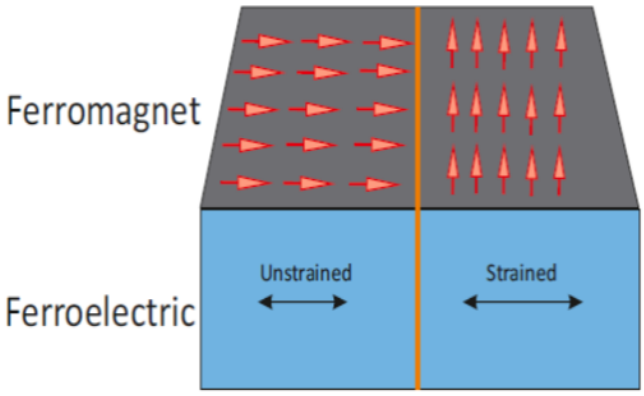

Figure 2.5 Magnetoelectric coupling through strain. The strain developed in the FE substrate by application of electric field is transferred to the magnetic thin film deposited on top of it through inverse magnetostriction and a change in magnetic state is observed.

can be strongly altered with a single-crystal ferroelectric. Further, Thiele *et al.* [63] have clearly demonstrated the role of strain in the manipulation of magnetization during the paramagnetic-ferromagnetic phase transition of $La_{0.7}Sr_{0.3}$ MnO_3, by applying in-plane electric field on PMN-PT (001) substrate. A reversible change in magnetization was observed in several oxide systems by strain-mediated electrical control of magnetism [72, 73, 74, 75].

2.3.2 Exchange Bias Mediated

Exchange coupling at the interface between FM and antiferromagnet (AFM) shows an exchange bias effect, where the exchange coupling leads to a shift in the magnetic hysteresis from the center of symmetry at zero magnetic field. By combining the exchange bias effect with the ME coupling between a FM and a antiferromagnet ferroelectric (AFFE), the magnetization of FM can be manipulated by application of electric field to the AFFE as shown in Fig. 2.6.

Many single phase multiferroics have FE and AFM orders like $YMnO_3$, $LuMnO_3$ and $BiFeO_3$(BFO) which serve as the AFFE layer. BFO has a weak magnetoelectric

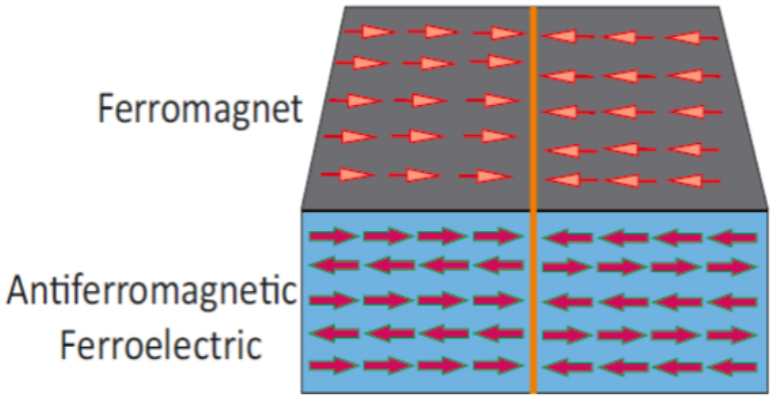

Figure 2.6 Magnetoelectric coupling through exchange bias. The AFM order of the moments in the FE are coupled to the magnetic moments of the FM. Upon switching the electric field, the AFM moments are reversed, which causes a change in the magnetic order through exchange bias.

coupling but exhibits multiferroic properties at room temperature and therefore it is a widely used single phase multiferroic. For thin BFO films the net magnetic moment is too small (0.01 μ_B/Fe) to be used in practical devices [76], but the AFM order in BFO can be altered by electric polarization. This provides a mechanism to control the magnetic properties of the FM deposited on BFO through exchange bias. Chu *et al.* [77] reported change in magnetic domain state of CoFe thin film deposited on BFO by electrical switching. Photo emission electron microscopy (PEEM) images at the Co *L* edges shows a rotation of magnetization of the structure by 90° by application of an electric field to the BFO film .

2.3.3 Charge Mediated

The magnetic properties of the FM which is coupled to a FE can be manipulated by modulating the charge at the interface by application of an electric field as shown in Fig. 2.7. Since the FE materials possess a higher charge modulation compared to silicon oxide or zirconium oxide, FE materials are more suitable to manipulate the

magnetism by charge modulation at the interface in artificial multiferroics.

First principles calculations by Duan *et al.* [78] in 2006 predicted a magnetoelectric coupling at the Fe/BTO interface, showing a sizable difference in magnetic moments of Fe and Ti at the FM-FE interface when the electric polarization reverses. Theoretical calculations also predicted induced magnetic moments for Ti and O in BTO at the interface with Fe [79]. Experiments performed on Fe and Co/BTO system show a change in the spin-polarization by the direction of FE polarization in BTO. The experiments using X-ray resonant magnetic scattering (XMRS) also revealed induced magnetic moments on Ti and O as predicted by the theoretical calculations [5]. Control of magnetism in FM oxide films by charge modulation at the interface with a FE substrate has also been reported by Molegraaf *et al.* [80] on LSMO (4 nm)/PZT (250 nm) system. This system exhibits a magnetoelectric hysteresis curve as demonstrated by magneto-optic Kerr effect (MOKE). Many systems exhibit magnetoelectric coupling through a charge effect and the nature of the effect can be distinguished as : (i) modification of the density of states near the Fermi level and electronic bonding at the interface, (ii) changes in magnetic exchange interaction, (iii) change in magnetic anisotropy. More information can be found in these review articles [81, 70, 82].

Chapter 4 of this thesis focuses on the magnetoelectric coupling between Fe and PMN-PT. Our results show that, by switching the ferroelectric polarization of PMN-PT, the accumulation/depletion of charge at the interface leads to a change in magnetic moments of ultra-thin Fe films.

2.4 Origin of PMA in CoFeB/MgO system

Ikeda *et al.* [7] developed magnetic tunnel junctions (MTJs) with a tunnel barrier of MgO sandwiched between CoFeB electrodes. They show that the MTJ has a PMA

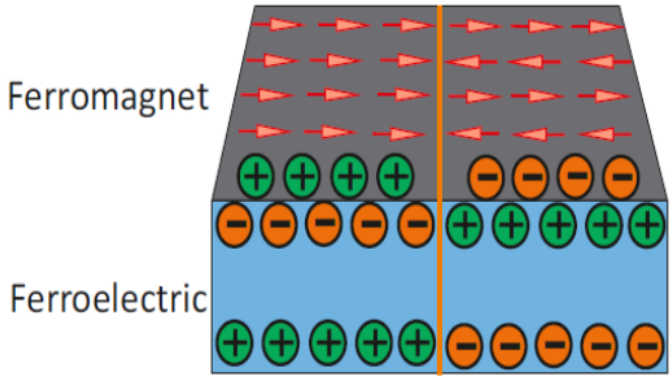

Figure 2.7 Magnetoelectric coupling through charge modulation. By manipulating the charge at the interface between the FM and FE, the magnetic order is controlled by switching the electric polarization of the FE.

for thickness of CoFeB of 1.3 *nm* and the PMA disappears for larger thicknesses of CoFeB. It was also shown that a perpendicular MTJ consisting of CoFeB/MgO shows a high tunnel magnetoresistance ratio, over 120%, high thermal stability at very low dimensions and very low switching current. The physical origin for PMA in CoFeB/MgO is not completely understood yet, but previous experimental findings have shown that three factors contribute to the PMA: (i) thickness of CoFeB, (ii) annealing temperature of CoFeB/MgO, and (iii) effect of capping layers, the details are discussed in the following sections. In this thesis chapter 5 is dedicated to understand the change in magnetic properties of CoFeB deposited on different oxides, and using XMCD for their characterization. Chapter 6 is allocated to understand the effect of capping layers on the magnetic anisotropy of CoFeB/MgO system, again studying their properties by using XMCD.

2.4.1 Thickness of CoFeB

As discussed above, PMA occurs due to symmetry breaking at the interfaces and surfaces [23], and it is observed in the CoFeB/MgO system. Therefore, the CoFeB

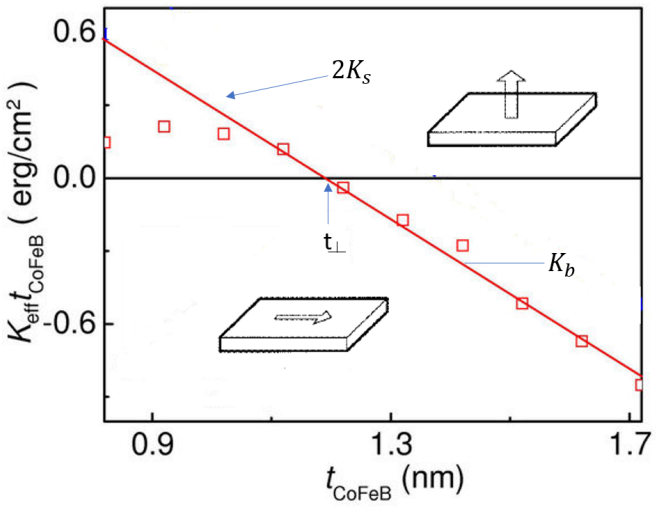

Figure 2.8 $K_{eff}.t_{CoFeB}$ value depending on the thickness of CoFeB. Positive K_{eff} shows out of plane magnetization and negative K_{eff} shows in-plane magnetization. Adapted from [83].

film must be below a certain thickness in order for the magnetization to point out of plane. In general for ultra-thin magnetic films, strong demagnetizing fields are created when the magnetization is rotated to out-of-plane from in-plane and these fields are responsible for the magnetization to be in-plane. This is also the case with CoFeB. These demagnetizing fields are the major contribution to K_b (shown in Eq. 2.9). Below a certain critical thickness, K_b is superseded by K_s resulting in PMA in the system. The influence of the surface anisotropy together with the thickness of CoFeB on the K_{eff} is described by equation 2.9 (on page 12) and the dependence of $K_{eff}.t_{CoFeB}$ with respect to t_{CoFeB} is shown in Fig. 2.8. A positive value of K_{eff} describes the preferred orientation of magnetization perpendicular to the plane and a negative value favoring in-plane magnetization. Below a certain thickness $t_\perp$ the interface anisotropy dominates the volume contribution resulting in a PMA in the system. In the case of CoFeB/MgO the $t_\perp$ is 1.3 nm.

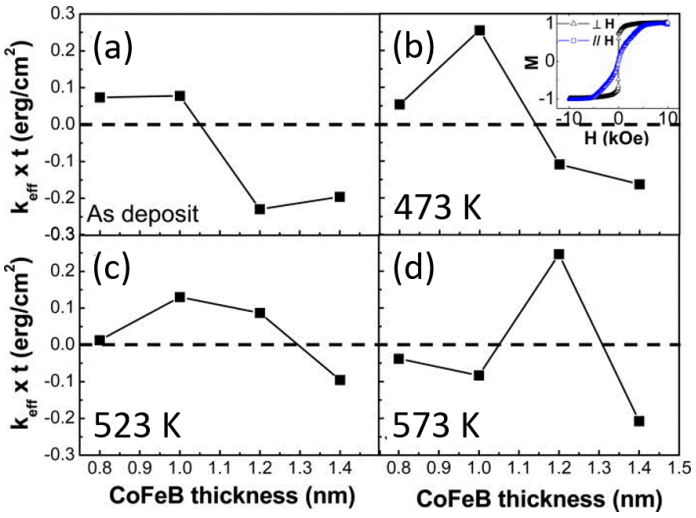

Figure 2.9 Dependence of $K_{eff} \times t$ on the CoFeB thickness for as deposited samples and annealed at different temperatures. The annealing temperature is indicated in each figure. Figure taken from [86].

2.4.2 Effect of Annealing

The PMA of the CoFeB/MgO systems also depends strongly on the annealing temperature and it is an important factor. Shimabukuro *et al.* [84] attributed the PMA in Fe/MgO to the hybridization between Fe 3d and O 2p orbitals. Annealing converts amorphous CoFeB to more crystalline CoFe, which in turn improves the PMA of CoFeB. But annealing at too high temperatures, causes the disruption of the hybridization between Fe 3*d* and O 2*p* orbitals due to B diffusion to the interface leading to poor PMA. The enthalpy for the formation of Fe-O bond i.e. FeO is lower compared to Co-O bond i.e. CoO, therefore the oxidation is more readily at the interfacial Fe site in comparison to Co [85]. Upon annealing to higher temperatures the B present in the CoFeB at the interface weakens the bond between Fe-O, forming a Fe-B or Co-B in-plane bond. So it is crucial to anneal at a temperature for bonding between Fe and O to be favorable.

As shown in Fig. 2.9 (a) the K_{eff} for as-deposited CoFeB shows low positive K_{eff} for

thickness of less than 1 nm and does not fit with Eq. 2.9. It is possible that the PMA in the system does not originate from interface but from other mechanisms. An increase in PMA was reported for all thicknesses except for 0.8 nm after annealing at 473 K as shown in Fig. 2.9 (b). The inset of Fig. 2.9 (b) shows the hysteresis loops for 1 nm CoFeB for in-plane and out-of-plane applied field measurements. The K_{eff} reached the maximum value for 1 nm thick CoFeB compared to the as deposited state for the same thickness. Upon further annealing to 523 K, the PMA was achieved for larger thickness range i.e. from 0.8 nm to 1.2 nm as shown in Fig. 2.9 (c) and larger thickness range provides more flexibility for perpendicular MTJ optimization. Annealing at 573 K, the K_{eff} becomes narrower and shows a maximum value for 1.2 nm thick CoFeB as shown in Fig. 2.9 (d). In general, a thicker CoFeB layer requires a higher annealing temperature to setup PMA.

2.4.3 Capping Layers

The capping layer adjacent to CoFeB has a decisive influence on the PMA value. The PMA in the capping layer/CoFeB/MgO system comes from the CoFeB/MgO interface (discussed in the above section) and capping layer/CoFeB interface. The PMA varies for different capping materials and is attributed to the different hybridization of both d and p orbitals via spin-orbit coupling. The most common capping layer used for the CoFeB/MgO system is Ta. Previous experiments revealed that changing the capping layer from Ta to Hf increases the interfacial PMA and with Ru it dramatically decreases [87, 88]. The PMA strength increases with increasing thickness of the capping layer [89]. First principles computation by Peng *et al.* [90] calculated the magnetic anisotropy energy (MAE) of the X/CoFe/MgO system with X including Ru, Ta and Hf. By calculating the layer- and orbital-resolved MAE, they confirm that the origin of PMA in these interfaces can be divided into two parts (i) CoFe/MgO, and (ii) X/CoFe interfaces. They calculate that the Hf has the

highest MAE for X/CoFe interface compared to Ta and Ru.

3 Experimental methods and instrumentation

In this chapter the details about the sample growth methods and main experimental techniques used are discussed. X-ray absorption spectroscopy (XAS) was used to understand the origin of the interface effect between the FM and different oxides and to observe the changes in magnetic properties. In XAS, the density of unoccupied states of the elements are probed. To match the atom-specific absorption edges the X-ray energy can be resonantly tuned at synchrotron sources. In this thesis the main technique used is XAS to probe the unoccupied states of Fe and Co. The basic principle and the theoretical basis for the XAS is discussed in section 3.1 followed by the concept of total electron yield detection mode for the XAS signal. By making paired measurements with the circularly polarized X-rays set to $c+$ and $c-$, and taking the difference between the measurements, the X-ray magnetic circular dichroism (XMCD) signal is measured. Using XMCD, element and shell-selective magnetic properties can be probed. In this thesis, the magnetic properties (spin and orbital moments) of Fe and Co were determined using XMCD. A detailed analysis of the XMCD spectra which extracts the information about the spin and orbital moments is discussed in section 3.2. The samples were pre-characterized using SQUID to determine the bulk magnetic moments. A short introduction about the superconducting quantum interference device (SQUID) is given in section 3.3.3.

Most of the XAS and XMCD experiments were carried out at the X-Treme beamline which is described in section 3.3.1. The description of XAS and XMCD is adapted from [2, 91].

Samples characterized in this thesis were grown using two techniques (i) electron beam evaporation, and (ii) magnetron sputtering. Fe/PMN-PT with Cr and Pd capping layers were grown by e-beam evaporation in the X-Treme sample preparation chamber and an introduction to the preparation chamber is given in section 3.3.1. The CoFeB, MgO, Ta, Pt and Ru were grown using magnetron sputtering. An introduction to the principle and the sputtering machine used for the thin film growth is given in section 3.3.2.

3.1 X-ray Absorption Spectroscopy (XAS)

In X-ray absorption, the incident X-rays excite the core-level electrons with their element specific binding energies. The XAS technique investigates the unoccupied electronic states, unlike X-ray photo electron spectroscopy (XPS) which investigates the occupied states. XAS measures the X-ray absorption coefficient ($\mu(E)$) near the absorption edge of a particular element which depends on the energy of the X-rays, the atomic number of the absorbing atom (Z), density (ρ) and atomic mass (m), $\mu(E) = \rho Z^4/E^3 m$. The extent of absorption depends on the photon energy E and the sample thickness t as shown in Fig. 3.1 (a) when X-rays of intensity I_0 impinge on the sample.

The intensity of the transmitted X-ray beam I_t is described by Beer's law:

$$I_t = I_0(E)e^{-\mu(E)t} \tag{3.1}$$

$\mu(E)$ decreases with increasing photon energy and increases with atomic number. When the photon energy exceeds the binding energy of a core electron, a new

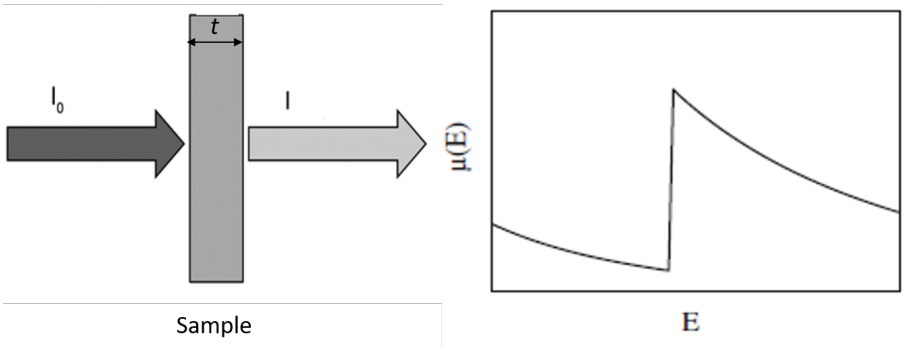

Figure 3.1 (a) Schematic of incident and transmitted X-rays referring to variation of $\mu(E)$. (b) $\mu(E)$ as a function of X-ray energy around the absorption edge. Figures taken from [92]

absorption channel is available in which a photoelectron and core hole are created by annihilation of the photon which leads to a sharp increase in absorption coefficient as shown in Fig. 3.1 (b) [93]. $\mu(E)$ continues to decrease with increasing photon energy above the absorption edge as the difference between the photon energy and the binding energy is converted into kinetic energy. The $\mu(E)$ is proportional to the absorption cross section σ_{abs}, that is, the transition probability per unit time P_{fi} to the photon flux I_{ph}:

$$\mu \propto \sigma_{ab} = \frac{P_{fi}}{I_{ph}} \tag{3.2}$$

The P_{fi} from initial state $|\psi_i\rangle$ to a final energy state $|\psi_f\rangle$ can be calculated from Fermi's Golden Rule:

$$P_{fi} = \int \frac{2\pi}{\hbar} |M_{fi}|^2 \, (1 - n(E_f)) \, \delta \, (\hbar\omega - (E_f - E_i)) \tag{3.3}$$

where δ function shows the conservation of energy in the absorption process and $(1 - n(E_f))$ is the density of unoccupied states. $M_{fi}|^2 = |\langle f|P \, \mathbf{A}|i\rangle|^2$ represents the

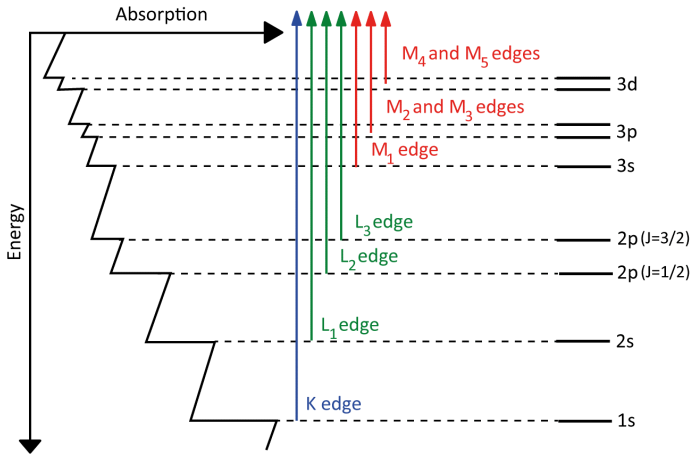

Figure 3.2 Transitions of the *K*, *L*, and *M* edges that contribute to XAS edges. Figure downloaded from *Wikimedia Commons*, https://en.wikipedia.org/wiki/X-ray_absorption_spectroscopy.

transition matrix from $|\psi_i\rangle$ to $|\psi_f\rangle$, where P is the momentum operator of the electron and $\mathbf{A}$ is the vector of the electric field containing the polarization of X-rays. Usually one electron transition is involved and together with *dipole approximation* for $P\,\mathbf{A}$, the P_{fi} can be written as:

$$P_{fi} = \int \frac{2\pi}{\hbar} |\langle f|\hat{\varepsilon}.\mathbf{r}|i\rangle|^2 \,(1 - n(E_f))\,\delta(\hbar\omega - (E_f - E_i)) \tag{3.4}$$

where $\hat{\varepsilon}$ represents the X-ray polarization vector and $\mathbf{r}$ is the position operator. The photon transfers angular momentum $q\hbar$ to the inner shell electron, where $q = +1$ and $q = -1$ refers to the right circularly polarized light ($c+$) and left circularly polarized light ($c-$), respectively, while $q = 0$ refers to linearly polarized light. The matrix element in Eq. 3.4 for transitions are allowed according to the dipole selection rules i.e. $\Delta l = \pm 1, \Delta m_l = q = 0, \pm 1$, and $\Delta m_s = 0$ for electric dipole interactions. Here l and m denote the orbital angular momentum quantum number.

At synchrotron sources the photon energy can be tuned to match the element specific binding energy, which makes XAS element specific. For instance, the

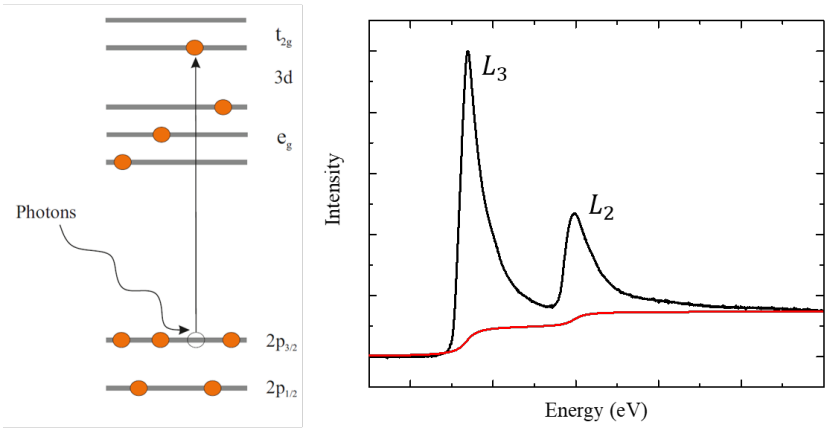

Figure 3.3 (a) Electronic configuration diagram showing the resonant XAS process at the *L*-edge. (b) Measured energy dependent resonant XAS showing a characteristic XAS line shape with two peaks L_3 and L_2 edges due to spin-orbit split of the 2*p* states.

electron transition from the occupied 2*p* orbitals to unoccupied 3*d* orbitals at the $L_{2,3}$-edges and transitions from the 1*s* to p states at the *K* edge. In this thesis, the XAS of the magnetic 3*d* transition metal elements Fe and Co are measured. These metals have valence electrons in 3*d* orbitals which determine their magnetic properties. The *d*-shell properties are best probed by *L*-edge absorption (2*p* to 3*d*) as the XAS is governed by dipole selection rules.

In the ground state the 2*p* orbitals are completely occupied, while the excited state exhibits a 2*p* core hole with angular momentum (transferred from the incoming X-rays) which couples to the spin via spin-orbit coupling. In the presence of the core hole the 2*p* states are split into $2p_{3/2}$ and $2p_{1/2}$ as shown in Fig. 3.3(a). This is reflected as a separation of the experimental *L*-edge XAS spectrum into two main peaks L_3 and L_2 as shown in Fig. 3.3(b). A polarization dependent absorption behavior is called dichroism. There are two types of dichroism: (i) Linear dichroism is defined as the difference between absorption of the X-rays polarized parallel and polarized perpendicular to an orientation axis, and (ii) circular dichroism, is the

difference between absorption of the two oppositely circularly polarized X-rays. In section 3.2, more details about XMCD are discussed.

Detection Methods of XAS- Total electron yield (TEY)

Using the transmitted X-rays it is possible to measure the absorption intensity for thin samples ($5 - 100\ nm$), but not possible for thicker samples. The samples used in this thesis have $\sim 0.5\ mm$ thick substrate and therefore total electron yield (TEY) detection mode was employed for measuring the absorption intensity. When the absorbed X-rays excite the core level electron, the core-hole will be occupied by the electrons from the higher energy state accompanied by the emission of a fluorescence photon or Auger electron. In TEY mode, the Auger electrons and outpouring secondary electrons with an energy high enough to leave the sample are detected. TEY mode is surface sensitive as the probing depth of the secondary electrons is nearly 2 nm [94]. TEY can be detected using channeltrons and by recording the sample drain current. The latter method was chosen to detect TEY with the help of an electro-meter in the range of picoampere. However, TEY signal may not accurately reflect the rate of absorption, as will be discussed below.

In Fig. 3.4(a), the θ_i is the X-ray incidence angle from the surface normal, λ_x is the X-ray penetration length (attenuation length) which is inverse of the $\mu(E)$, $\lambda_x \cos\theta$ is the X-ray penetration depth, and λ_e is the electron sampling depth. The probability of an electron to escape from the surface (dY_e) decreases exponentially with increasing depth of the absorption of the photon from the surface (z) as shown in Fig. 3.4(b) and the number of electrons reaching the surface is given by:

$$dY_e = dY_0 \ \exp[-z/\lambda_e] \tag{3.5}$$

The above Eq. 3.5 shows that the TEY is a surface sensitive method to measure the XAS. dY_0 is the number of secondary electrons created in layer of thickness dz and described by the following expression [2]:

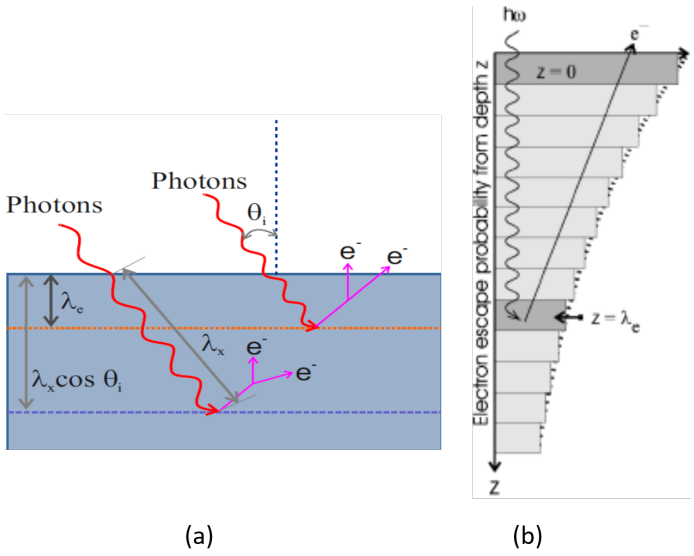

Figure 3.4 (a) Emission of electrons from the surface when $\lambda_e \ll \lambda_x$ after absorption of X-rays under grazing incidence on a infinite sample. (b) The probability of electron escape as a function of the depth z. The escape probability decreases exponentially with increasing z. Figure taken from [95]

$$dY_0 = I_0 G \frac{\mu}{\cos\theta} \exp[-\mu z/\cos\theta]\, dz \tag{3.6}$$

The absorption is angular-dependent $\mu(\theta, E) = \mu(E)/\cos\theta = \mu/\cos\theta$ and the factor G is the average number of secondary electrons. Upon integrating Eq. 3.7 over dz from $z = 0$ to $z = \infty$ the TEY intensity is calculated and can be written as:

$$I_{TEY} = \frac{I_0 G \mu \lambda_e}{\cos\theta} \frac{1}{\mu\lambda_e/\cos\theta + 1} = \frac{I_0 G \mu \lambda_e}{\lambda_x} \frac{1}{\lambda_e/\lambda_x + 1} \tag{3.7}$$

For $\lambda_x >> \lambda_e$, the TEY signal is proportional to $\mu(E)$ and can be written as $I_{TEY} = I_0 G \lambda_e \mu/\cos\theta$ and for $\lambda_x << \lambda_e$, the TEY signal is independent of the $\mu(E)$, which means the signal is saturated. To avoid saturation in our experiments, the incidence angle ranges from 0° to 60° with respect to the surface normal. More details about saturation effects in TEY can be found in this paper for Fe, Co and Ni [95].

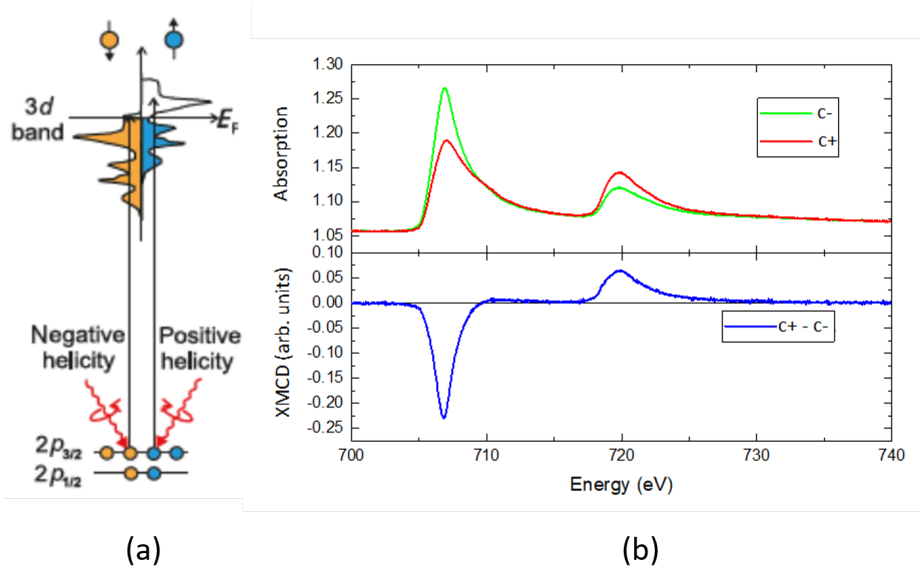

Figure 3.5 (a) Illustration of the XMCD effect at the L-edge absorption for Fe metal showing density of states for the spin-up and spin-down. Figure taken from [96]. (b) The experimental data at the Fe edge, showing the XAS for $c+$ and $c-$ polarization and the difference between them is the XMCD (blue line).

3.2 X-ray magnetic circular dichroism (XMCD)

XAS using synchrotron radiation is a well established technique providing information on electronic and structural states of atoms, surfaces, molecules and solids. X-ray magnetic circular dichroism (XMCD) is the measure of difference between circularly polarized light ($c+$ and $c-$). The XMCD intensity is proportional to the magnetization M of the sample projected to the photon propagation direction and the angular momentum L_{ph} of the photons.

$$\Delta I_{XMCD} = I^{\sigma+} - I^{\sigma-} = I^{\uparrow L_{ph} \uparrow M} - I^{\downarrow L_{ph} \uparrow M} \tag{3.8}$$

For maximum XMCD effect, the M and L_{ph} have to be parallel to each other. The dichroism effect for Fe is illustrated in Fig. 3.5 (a), where the difference between the positive angular momentum i.e $q = +1$, L_{ph} points in the direction of wavevector

k and negative angular momentum i.e. $q = -1$, L_{ph} points in the direction of wavevector $-k$ for $p \longrightarrow d$ aligned along the fixed direction of the magnetization (Eq. 3.8) . In Fig. 3.5 (b) on the top, an illustration of experimental XAS at $L_{2,3}$-edge of Fe for $c+$ and $c-$ with XMCD on the bottom is shown.

3.2.1 Origin of XMCD effect- Two-step model

The XMCD effect at the $L_{2,3}$-edges of $3d$ metals is explained by the two-step model proposed by Stöhr and Wu [3]. In the first step, the core electron (p-shell) is excited (to the $3d$ shell) by circularly polarized X-ray photons ($c+$ and $c-$) that carry the angular momentum $\pm q\hbar$ which obeys the dipole selection rules in Eq. 3.4 and the excited photoelectrons are spin polarized. The spin polarization of excited photoelectrons is opposite for incident X-rays with positive or negative spin. In the case of $2p_{3/2}(L_3)$ and $2p_{1/2}(L_2)$ levels have opposite spin polarization at the two edges as they have opposite spin-orbit coupling i.e. $l + s$ and $l - s$, where l and s are the orbital and spin moment, respectively. For the specific case as shown in Fig. 3.6, a photoelectron is excited from a spin-orbit split level of $2p$ core shell to the partially unfilled $3d$ valence shell by an X-ray photon with $q = +1$. This may lead to electron transitions probabilities, which are given by Clebsch-Gordon coefficients [97, 98]. These excitations yield an orbital polarization of excited electrons with their related probabilities (same for electrons from $2p_{3/2}(L_3)$ or $2p_{1/2}$ core levels) and summing up all their excitations on their probabilities, the spin polarization of the excited electron is found. For positive angular momentum ($q = +1$) of the X-rays at the L_3-edge 62.5% spin-up electrons are excited and for negative angular momentum of X-rays ($q = -1$) excite 37.5% spin up electrons, whereas at the L_2-edge for $q = +1$ excites 25% of spin-up electrons and the X-rays with $q = -1$ excites 75% of spin up electrons. In the second step, the unequal spin-up and spin-down bands present in the exchange split valence shell acts as spin dependent detectors. Hence, the

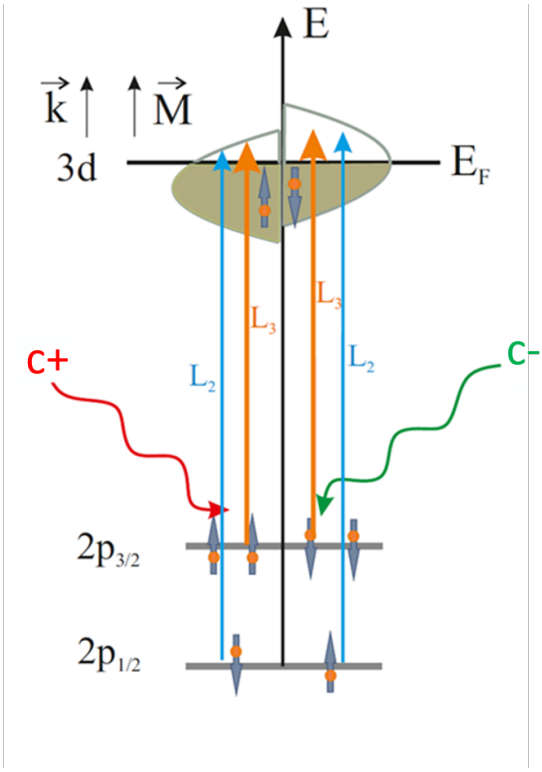

Figure 3.6 Two-step model of XMCD. In first step, depending on the helicity of the incoming X-rays the spin-orbit split $2p_{3/2}$ and $2p_{1/2}$ core levels acts as spin-polarized source. In second step, the polarized photoelectrons are used to analyze the spin-split density of valence states, thus the valence band acts as the spin-sensitive detector. Figure adapted from [99].

observed dichroism comes from the imbalance in either spin or orbital momentum in the empty bands.

3.2.2 Sum rules and data analysis

By using the sum rules derived by Thole *et al.* [100] and Carra *et al.* [101] it is possible to distinguish the spin and orbital contributions to a dichroic signal. For the spin-orbit split absorptions of the $2p_{3/2}$ and $2p_{1/2}$, the spin (m_s) and orbital (m_{orb}) magnetic moments for unoccupied final state is determined by the following

equations [102]:

$$m_s = -\frac{6\int_{L_3}(\mu_+ - \mu_-)\,d\omega - 4\int_{L_3+L_2}(\mu_+ - \mu_-)\,d\omega}{\int_{L_3+L_2}(\mu_+ + \mu_-)\,d\omega}\, n_h \left(1 + \frac{7\langle T_z\rangle}{2\langle S_z\rangle}\right)^{-1} \tag{3.9}$$

$$m_{orb} = -\frac{4\int_{L_3+L_2}(\mu_+ - \mu_-)\,d\omega}{3\int_{L_3+L_2}(\mu_+ + \mu_-)\,d\omega}\, n_h \tag{3.10}$$

where $\mu+$, $\mu-$ denote the absorption coefficient of the XAS spectra taken with $c+$ and $c-$ polarized light, respectively and n_h is the number of holes in $3d$ shell. The L_3 and L_2 denote the integration range. $\langle S_z\rangle$ is the expectation value of the spin moment projected along the X-rays direction. $\langle T_z\rangle$ is the expectation value of the intra-atomic magnetic dipolar operator, accounting for a possible asphericity of the spin density distribution due to crystal field strength, charge transfer effects, the $3d$ spin-orbit coupling and the magnetic field [103]. The $\langle T_z\rangle$ can be neglected for metallic systems as the spin-orbit coupling is weak.

Using Eq. 3.9 and 3.10, the spin and orbital moments for Fe and Co are calculated. The (n_h) for Fe and Co are taken at 6.61 and 7.51 respectively [102]. In Fig. 3.7 (a), (b) and (c), the resulting $\mu+$ and $\mu-$, $\mu + +\mu-$ (the XAS spectra) and $\mu + -\mu-$ (the XMCD spectra) at the Fe $L_{3,2}$ edges are shown, respectively. The unoccupied s, p orbitals gives rise to a step-like background. The step function is subtracted at the L_3 and L_2-edges representing 2/3 (1/3) of the complete edge jump in equivalence to the degeneracy of the initial states $L_3/L_2 \sim 4/2$ as shown in Fig. 3.7 (b) (red line). The resultant XAS is normalized to the jump of the L_3-edge, then step function is subtracted and the XAS is integrated in the range of the considered edges, blue line in Fig. 3.7 (b). The XMCD is normalized to the jump of the XAS and then integrated (blue line) as illustrated in Fig. 3.7 (c). Similarly, the sum rules were calculated at the Co edge as illustrated in Fig. 3.8. In the later chapters the XMCD is shown as $(c + -c-)/(c + +c-)$ and is shown as percentage.

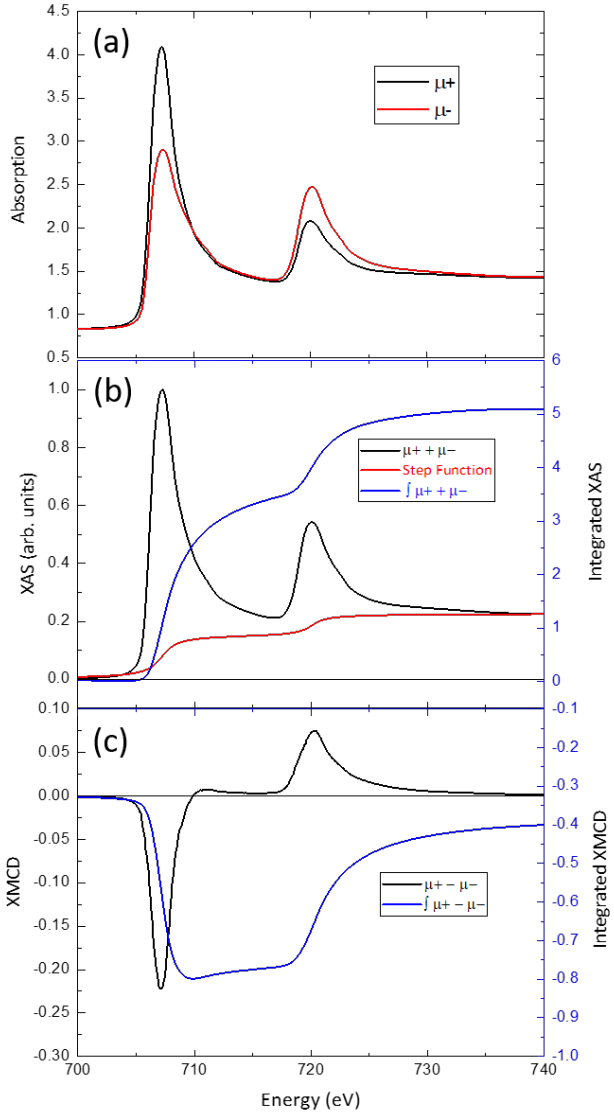

Figure 3.7 Illustration of sum rule analysis at the Fe $L_{3,2}$ edges (a) absorption spectra for two X-ray polarizations (b) XAS, sum of the two polarizations (black), step function (red line) and the integrated XAS after subtracting the step function (blue line) (c) XMCD and integrated XMCD (blue line).

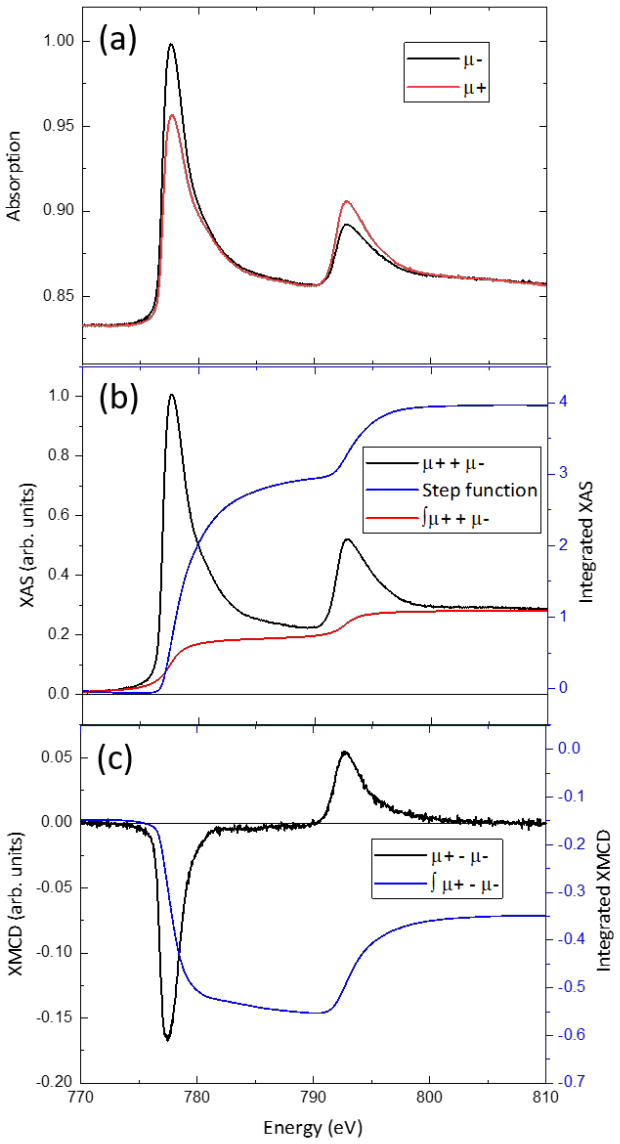

Figure 3.8 Illustration of sum rule analysis at the Co $L_{3,2}$ edges (a) absorption spectra for two X-ray polarizations (b) XAS, sum of the two polarizations (black), step function (red line) and the integrated XAS after subtracting the step function (blue line) (c) XMCD and integrated XMCD (blue line).

The sum rule error bar is usually 10% of the calculated moments. The error for Fe atom was determined by integrating the XMCD upto 740 eV, 750 eV and 760 eV, then taking the standard deviation of the integrated XMCD at these energy values. Similarly, the Co sum rule error bar is also determined.

3.3 Experimental Instrumentation

The samples discussed in chapter 4 were grown using an e-beam evaporator in the sample preparation chamber and were studied by XMCD at the X-Treme beamline at the Swiss Light Source (SLS), Paul Scherrer Institut (PSI). An introduction to the sample preparation and beamline is given in section 3.3.1. The CoFeB samples (discussed in chapter 5 and 6) were grown by magnetron sputtering and were characterized using superconducting quantum interference device (SQUID)[1]. Later, the samples were studied using XMCD at the X-Treme beamline and Surface interface: Microscopy (SIM) beamline at the SLS. The following sections will give a description about the instruments used for thin film growth and characterization.

3.3.1 X-Treme beamline

To characterize magnetic materials, polarized X-rays have appeared as distinctive study due to their specific interaction with magnetic materials. Today's synchrotrons of the third generation bright light source have characteristic parts called insertion devices (IDs) installed in straight sections of the storage ring. Undulators are one of the types of IDs. They are used to set the polarization of the X-rays by the idea proposed by Sasaki *et al.* [104]. Undulators have a periodic array of magnets. To produce polarized X-rays, the undulator forces the electrons beam to follow a helical trajectory. An undulator provides better brilliance and order of magnitude

[1]Both deposition and magnetic characterization were done at the Mesoscopic system group at PSI

photon flux connected to a bending magnet. A monochromater is used to select a narrow band of wavelength of radiation chosen from a wider range of wavelength available.

The X-Treme beamline is equipped with an Apple-2 elliptical UE54 undulator that allows the switching of the X-ray helicity to obtain XMCD. X-Treme beamline involves measurements of XMCD and X-ray linear dichroism at transition metal $L_{2,3}$ -edges, lanthanide $M_{4,5}$ -edges and oxygen or nitrogen K edges. The X-ray energy range is $400-2000\,eV$. The emission from the undulator in the first harmonic gives the X-rays in the energy range to probe the $L_{3,2}$-edges of the $3d$ transition metals for XAS and XMCD. The energy scans were measured in the fly-mode where the monochromater and undulator are scanned continuously and simultaneously. Below an introduction to the X-Treme endstation which includes the measurement chamber and the sample preparation chamber is given.

XMCD measurement chamber:

The end-station has a superconducting vector magnet, where 7 T of magnetic field can be applied parallel to beam direction and 2 T of magnetic field perpendicular to the beam direction. The remanent field is in the range of $4-10\,mT$ depending on the maximum field used. The sample temperature can be varied from $2\,K-370\,K$. The pressure in the cryostat is in the low $10^{-11}\,mbar$ range. The end-station has five SMA feedthroughs, one allowing the XAS detection through total electron yield (TEY) and the other four for electrical contacts connecting the sample holder. These four contacts can be used to apply a voltage of below $300\,V$. At X-Treme, the XAS signal can be detected by TEY, total fluorescence yield (TFY) and transmission. We used TEY detection mode to measure the XAS. Mentioned in section 3.1, the sample drain current was used to detect TEY. In TEY detection mode, the sample is highly electrically insulated. The beam spot for the measurements of sample (Cr capped/Fe/PMN-PT) discussed in chapter 4 (section 4.1) has a width of 220 μm,

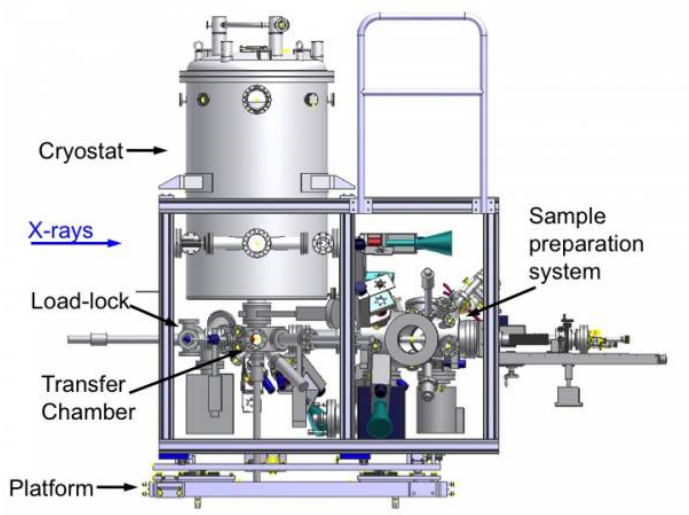

Figure 3.9 Schematic of the X-Treme end-station. Figure taken from [105].

while the height of the exit slit (adjustable) is 30 μm. For the measurements of Pd capped/Fe/PMN-PT and CoFeB/different oxides discussed in chapter 4 (section 4.2) and chapter 5, respectively, the beam spot was unfocussed. A schematic of the end-station with preparation chamber is shown in Fig. 3.9. More details about the beamline are described in this paper [105].

Preparation chamber

X-Treme end-station is equipped with UHV chamber for *in-situ* sample preparation, where samples from thin films to molecules can be grown. The base pressure in the chamber is usually around low 10^{-9} mbar. The preparation chamber is equipped with scanning tunnel microscope (STM) to characterize the growth of the molecules or thin films on metallic substrates. The chamber has also a quartz balance to monitor the growth rate of the evaporants. A picture is shown in Fig. 3.10, where three different evaporators can be mounted simultaneously. A poling stage is also built in the chamber to electrically switch the samples. The sample chamber is connected to the super-conducting magnet where the XMCD measurements are carried out, where the prepared samples can be transferred in the UHV without exposing the samples to the atmosphere.

A Omicron Triple EFM metal evaporator was used to evaporate Fe, Cr and Pd. Triple EFM features three independent cells for the evaporation of a wide range of materials from wires, rods or crucibles. Fe, Cr and Pd rods were mounted in Triple EFM for evaporation. Each cell in evaporator is equipped with a filament, flux monitor and high voltage (HV) supply. After the rods are loaded in the evaporator, it is connected to the preparation chamber and pumped down to UHV. The rods are degassed for few hours to clean them by application of filament current and HV till a small flux current is observed. Later, the evaporator is opened to the preparation chamber and the samples can be grown by monitoring the flux rate with adjustment of filament current and HV. In our case, the STM was used to precisely calibrate the Fe deposition rate on the monolayer (ML) range. For means of calibration a Au/Mica substrate was used. After the calibration was done, the real deposition on PMN-PT was carried out. Quartz balance was used to determine the thickness of Cr or Pd as higher growth rates were used in comparison to Fe (lower flux rate). More details about the sample preparation are described in chapter 4.

3.3.2 Magnetron Sputtering

Magnetron sputtering uses heavy-element (Ar gas) plasma to bombard a target material, which vaporizes and condenses onto a substrate as shown in Fig. 3.11 (a). Electrically neutral Ar atoms are introduced into a vacuum chamber at a pressure of 2×10^{-7} *mbar*. A DC voltage is placed between the target (cathode) and substrate (anode) which ionizes Ar atoms and creates plasma, hot gas-like phase consisting of ions and electrons, in the chamber. The charged Ar collide with the target ejecting atoms, which are accelerated by DC voltage to settle on the substrate surface. Electrons released during Ar ionization are accelerated to the anode substrate, subsequently colliding with additional Ar atoms, creating more ions and free electrons in the process. Magnetrons make use of the fact that

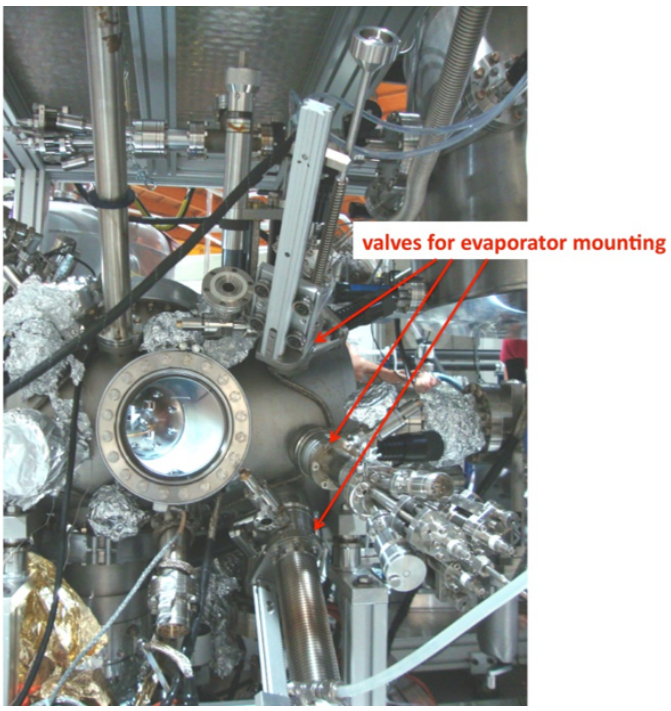

Figure 3.10 A picture of the sample preparation chamber at the X-Treme beamline.

a magnetic field configured parallel to the target surface can confine the plasma above the target. The increased ion efficiency results in a dense plasma in the target region. This in turn leads to increased ion bombardment of the target, resulting in higher sputtering rates and therefore, higher deposition rates at the substrate. As the bombardment process continuously ionizes Ar atoms the pressure is about 2 *mbar* during sputtering. To initiate the plasma formation process, a critical voltage is required [106, 107].

Two parameters control the rate of growth of the thin film; the process gas pressure and the voltage applied to the target. Using higher gas pressure increases the ionization events which in turn decreases critical voltage. This increase in pressure decreases the growth rate as the mean free path of target atoms is decreased. By increasing the voltage above the critical value the Ar ions gain more energy increasing the growth rate, which further increases the evaporation events on the target surface.

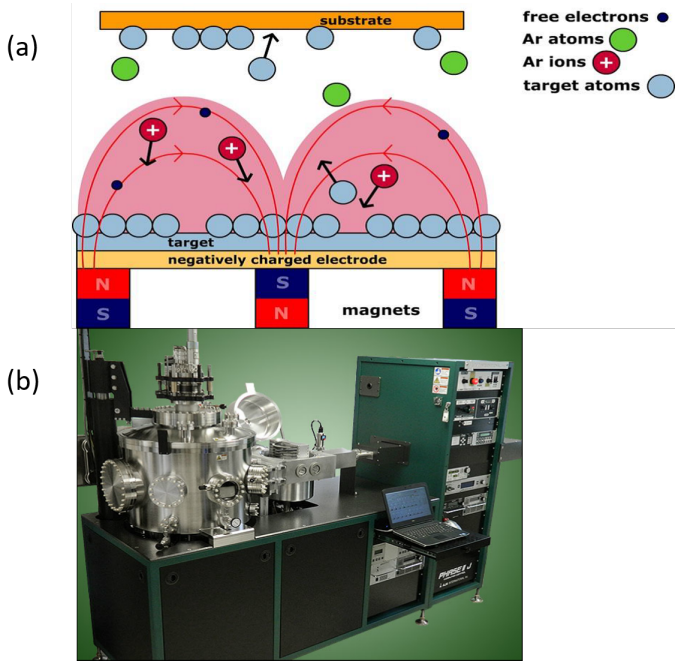

Figure 3.11 (a) Magnetron Sputtering principle, (b) Sputtering Machine. Both images taken from http://www.polifab.polimi.it/equipments/orion-8/

Fig. 3.11 (b) shows the AJA ATC Orion 8 sputtering system at the Mesoscopic Systems group, PSI, which was used to grow thin films of CoFeB, MgO, Ta, Pt and Ru. The sputtering system has a mechanized shutter to control the exposure of the substrate to the vaporized target material. Initially, the shutter is closed when the plasma production starts and impurities on the target material surface are evaporated. After the initialization is complete the rate of evaporation is constant and film thickness is controlled by setting the total sputter time. The samples can be annealed up to 1000 K.

3.3.3 Superconducting quantum interference device (SQUID)

SQUID magnetometry uses a combination of superconducting materials and Josephson junctions to measure magnetic fields with resolution up to 10^{-14} T as shown in Fig. 3.12 (a). The superconducting rings enclose magnetic flux as a

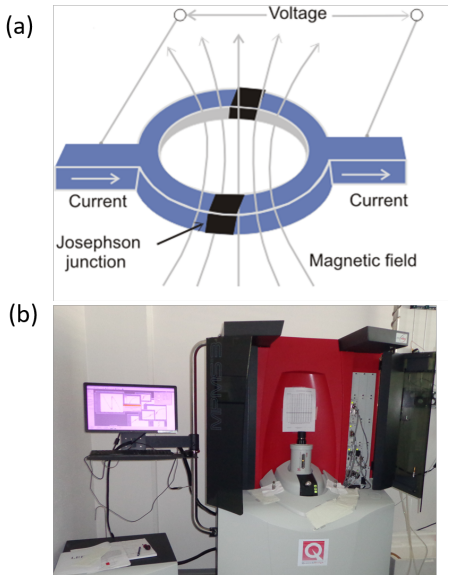

Figure 3.12 (a) SQUID principle, (b) MPMS3, SQUID magnetometer. Image taken from http://www.geocities.ws/pranab_muduli/squid.html#clarcke1994sa

constant called flux quantum. As the flux quantum is very small, the physical effect can be used to produce a sensitive magnetic detector known as the SQUID. The Joseph junctions have two superconductors separated by a thin insulator layer which can experience tunneling of Copper pairs of electrons through the junction. This junction provides a weak link between the two superconductors which can support a supercurrent below a critical current [108, 109].

To characterize the CoFeB samples discussed in chapter 5 and 6, a MPMS SQUID was used located at Mesoscopic systems group at PSI as shown in Fig. 3.12 (b). This SQUID uses a AC Josephson effect, where the voltage across the junction is proportional to the Josephson junction which oscillates with a characteristic frequency. It has a sensitivity of nearly 5×10^{-8} *emu*. The sample temperature can be stabilized in the range $1.8 - 400$ *K* and the maximum applied field is 7 *T*.

4 Study of magnetoelectric coupling between ultra-thin Fe films and PMN-PT by XMCD

In section 2.3.3, an introduction to the charge mediated magnetoelectric coupling in different system is reviewed. Heidler *et al.* [110] have reported the co-existence of strain and charge effect in magnetoelectrically coupled Co-wedge/PMN-PT (011). Switching the FE polarization of PMN-PT from P_{up} to P_{down} a change in magnetic anisotropy of the thin part of Co ($\sim 3.5\ nm$) was observed but no change in magnetic anisotropy at the thick part of Co ($\sim 6\ nm$). In this chapter, the magneto-electric coupling between an ultra-thin Fe film and PMN-PT (001) is studied. The observed change in magnetic properties of Fe by switching the FE polarization of PMN-PT is discussed.

X-ray absorption spectra and magnetic circular dichroism were measured at the Fe $L_{3,2}$-edges of an iron wedge with a Cr layer on a ferroelectric substrate in total electron yield mode. Upon switching the ferroelectric polarization from P_{up} to P_{down}, a relative change in total magnetic moment of 20% for 1.5 *nm* thin Fe is observed. For 3 *nm* thin Fe the relative change is within the sum rule error bar as discussed in section 4.1.2. Taking the sampling depth of the measurement method into account, this difference is compatible with a magnetic anisotropy change taking

place in the first interfacial layer in contact with the ferroelectric substrate which is discussed in section 4.1.3. By changing the capping layer to Pd, the magnetization of 1.5 *nm* thin Fe lies in between out-of-plane and in-plane direction. By switching the FE polarization the out-of-plane magnetization decreases and the magnetization is tending towards in plane direction as examined in section 4.2.2. The observed change in magnetic anisotropy is attributed to interfacial coupling to a charge accumulation or depletion at the interface.

4.1 Cr/Fe/PMN-PT (001)

4.1.1 Sample fabrication and experimental details

The sample was grown in the X-Treme beamline preparation chamber as presented in section 3.3.1. Fe and Cr were loaded in the triple e-beam evaporator. The growth rate of Fe was determined by using the scanning tunnel microscope (STM) available at the preparation chamber. Initially, the Fe was evaporated using a flux of 15 *nA* for 1 min on the pre-sputtered and annealed Au/Mica at room temperature in UHV conditions. The STM image shown in Fig. 4.1 shows the Fe coverage on Au/Mica. By doing the particle and pore analysis, the Fe coverage is nearly 10% of the monolayer (ML) for the parameters used for evaporation. Similarly, the Cr calibration was done with the help of in-built quartz balance at the preparation chamber as a higher flux of 110 *nA* was used. The above mentioned flux parameters were used to grow Fe and Cr on PMN-PT (001).

As discusses in section 2.2.1, relaxor (001)-oriented PMN-PT (Atom Optics Co. LTD) was chosen as the FE substrate. First a bottom contact of 30 *nm* thick Au layer was deposited on the back of the PMN-PT for switching the FE polarization. Next, the substrate was introduced in a UHV sample preparation chamber. Inside

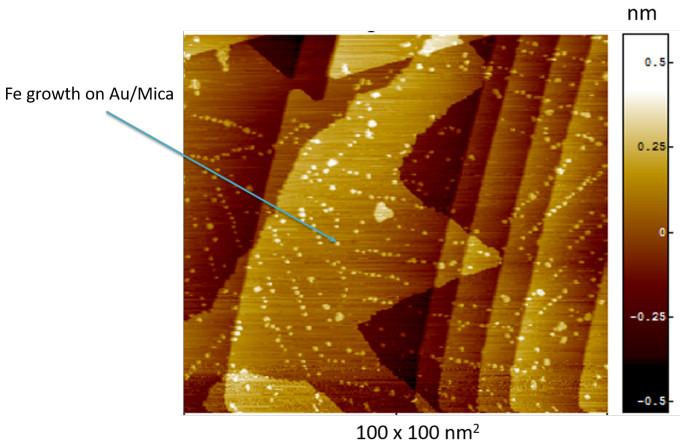

Figure 4.1 STM image of Fe growth on Au/Mica. By applying particle to pore analysis, the coverage is detemined to be 10% of a monolayer.

the chamber the substrate was heated up to 383*K* for 30 minutes to remove the water from the surface. A continuous wedge of Fe with thickness varying from 0.3 *nm* to 3 *nm* was grown on 0.5 *mm* PMN-PT with a help of a manual shutter under UHV conditions with the substrate held at room temperature. A 3 *nm* thick Cr film was grown on top of Fe wedge to provide a continuous conductive layer acting as top electrode. The schematic of the sample can be seen in Fig. 4.2 (a). The FE polarization was switched in the beamline's sample preparation chamber as mentioned in the previous chapter, by ramping the electric field to a maximum of ± 2.2 *kV*/*cm* and the I-V curve was recorded to confirm the switching (shown in Fig. 4.2 (b)); P_{up} refers to positive charge at the PMN-PT interface and P_{down} refers to negative charge at the PMN-PT interface (shown in Fig. 4.2 (a)). After switching the FE polarization the sample was transferred in UHV conditions to the measurement chamber.

The XAS and XMCD experiments were carried out at the X-Treme beamline at Swiss Light Source (see section 3.3.1). The spectra were acquired in TEY mode and without applied electric field to have better signal to noise ratio. Due to high electric susceptibility (2.2.1) the polarization remains unaffected throughout

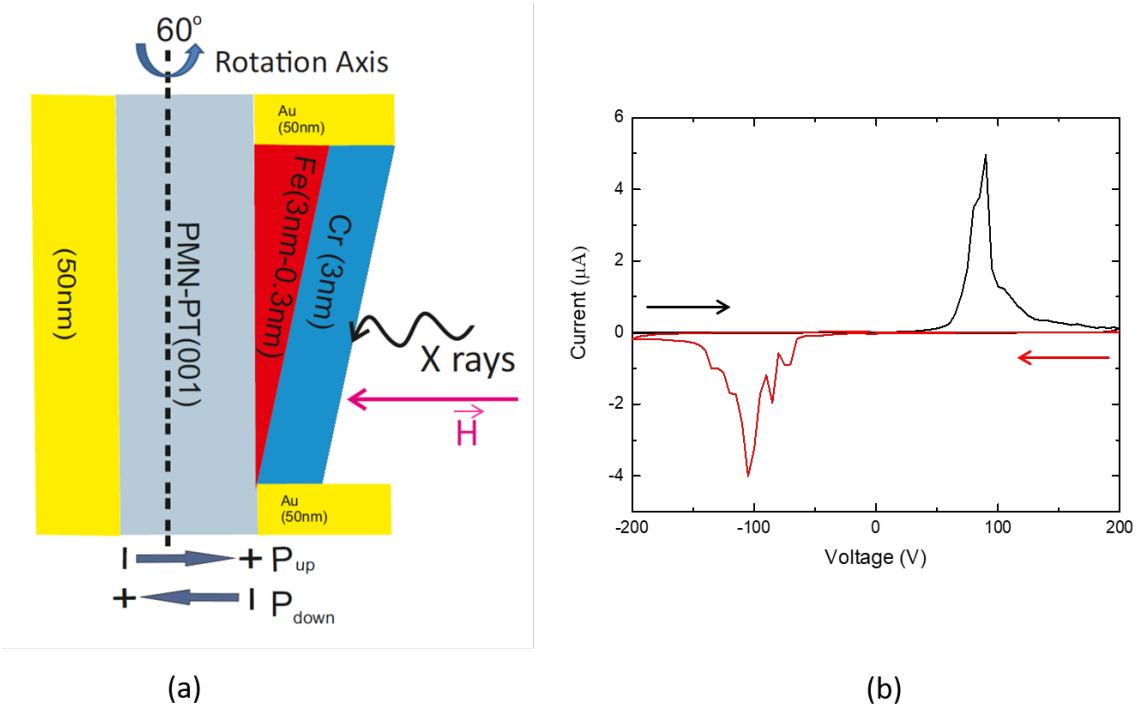

Figure 4.2 (a) Schematic of the Cr (3 *nm*)/Fe (0.3 *nm* – 3*nm*)/PMN-PT (001) sample with marked directions of the FE polarization vector. The X-rays impinge the sample at grazing or normal incidence (b) I-V curve of the sample. The black arrows represent the polarization with positive voltage and the red arrows show the polarization with negative voltage. Upon integrating the displacement current, the total charge (± 15 $\mu C/cm^2$) accumulated or depleted at the interface is calculated.

the measurements. The measurements were performed at a base temperature of ~ 1.5 *K* at the cold finger which corresponds to 2 – 3 *K* at the sample. The spectra were measured at 0.3 *nm*, 1.5 *nm* and 3 *nm* film thickness, corresponding to 1 ML, 5 ML, 10 ML, respectively [111]. The absorption spectra were recorded at the Fe $L_{3,2}$ - edges and Cr $L_{3,2}$ - edges in two geometries: with X-rays at an angle of 60° to the surface normal (i.e. 30° of grazing incidence), and parallel to the surface normal (normal incidence) (shown in Fig. 4.2 (a)). The XMCD measurements were first taken in an applied magnetic field of 6.8 *T* and then in remanence. The results of the XAS and XMCD spectra for both FE polarizations are shown in the next section.

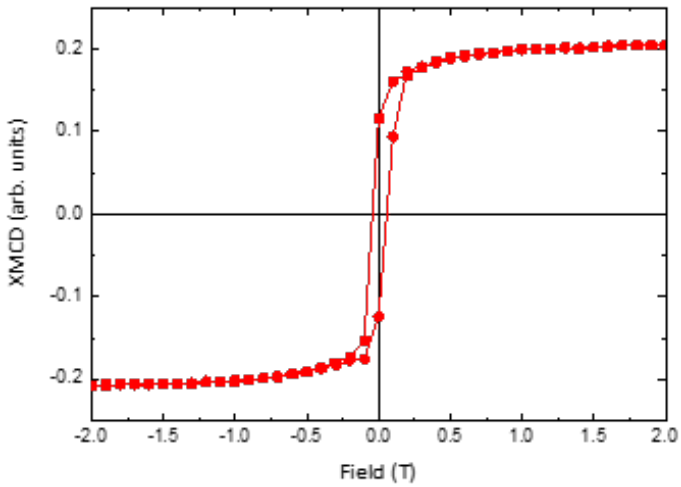

Figure 4.3 Hysteresis curve for 1.5 *nm* thin Fe on PMN-PT (011) measured along grazing incidence at 3 *K*.

4.1.2 Results

A maximum field available of 6.8*T* was applied as the field required to saturate the 0.3 *nm* was not known. But a field of 0.5 *T* was enough to saturate the 1.5 *nm* thin Fe. The saturation field was determined by measuring a hysteresis curve using XMCD on a Cr capped/Fe (1.5 *nm*)/PMN-PT (011) [1] along grazing incidence at 3*K* as shown in Fig. 4.3. The field required to saturate the 1.5 *nm* is 0.5 *T*.

The magnetization direction of the Fe film was probed by measuring the XMCD signal at grazing and normal incidence at different Fe film thickness. No remanent magnetization was detected for 0.3 *nm* thin Fe, while a clear in-plane magnetization was observed for 1.5 *nm* thin Fe as shown in Fig. 4.4 (b). The small XMCD observed along normal incidence of the film as show in Fig. 4.4 (a) is attributed to the small remanence from the superconducting magnets, as mentioned in section 3.3.1. The magnetization was along the in-plane direction for 3 *nm* thin Fe also.

In order to study the effect on the Fe magnetization due to the PMN-PT FE polarization, XMCD measurements were performed with FE polarization P_{up} and

[1] The text presented is partly adapted from our recent publication [112]

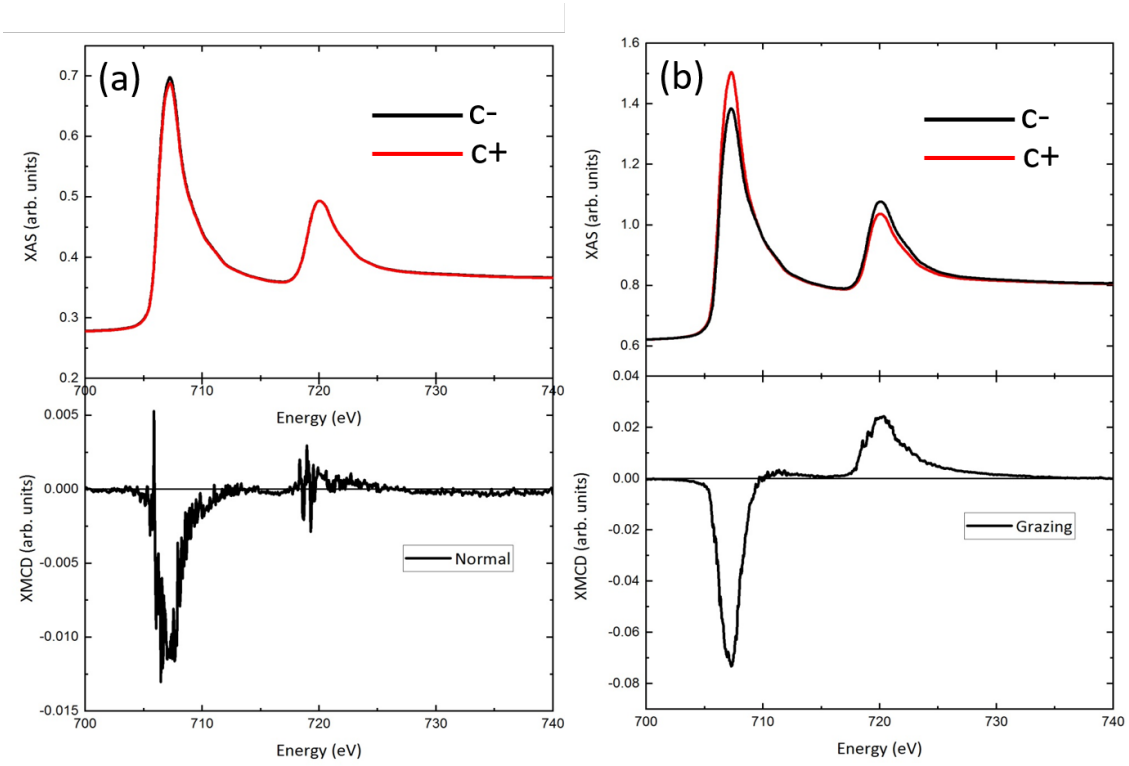

Figure 4.4 The XAS and XMCD measured at the $L_{3,2}$-edges at 1.5 *nm* thin Fe in remanence at 3*K* (a) at normal incidence (b) at 60° to the surface normal.

P_{down} as shown in Fig. 4.2 (a) in applied magnetic field of 6.8 *T* and in remanence. The data are shown in Fig. 4.5 (a), (b) and (c) for applied magnetic field and in Fig. 4.5 (d), (e) and (f) in remanence, for 0.3 *nm*, 1.5 *nm* and 3 *nm* thin Fe, respectively. No change in XMCD is observed for measurements in applied magnetic field for the aforesaid thicknesses of Fe. No remanence was observed for 0.3 *nm* thin Fe for both FE polarizations as shown in Fig. 4.5 (d). As no oxidation was observed at the Fe $L_{3,2}$-edges as shown in Fig. 4.6 (a), we believe that ultra-thin Fe film does not show remanence because it grows in the form of nano-islands which will be superparamagentic at 3 *K*. This Fe nano-island growth has been observed by Radaelli *et al.* [113] for Fe on $BaTiO_3$. Their TEM results show that Fe grows in the form of nano-islands in the thickness range of 1-4 ML. A clear change for the XMCD measured in remanence was observed for 1.5 *nm* thin Fe film. As shown

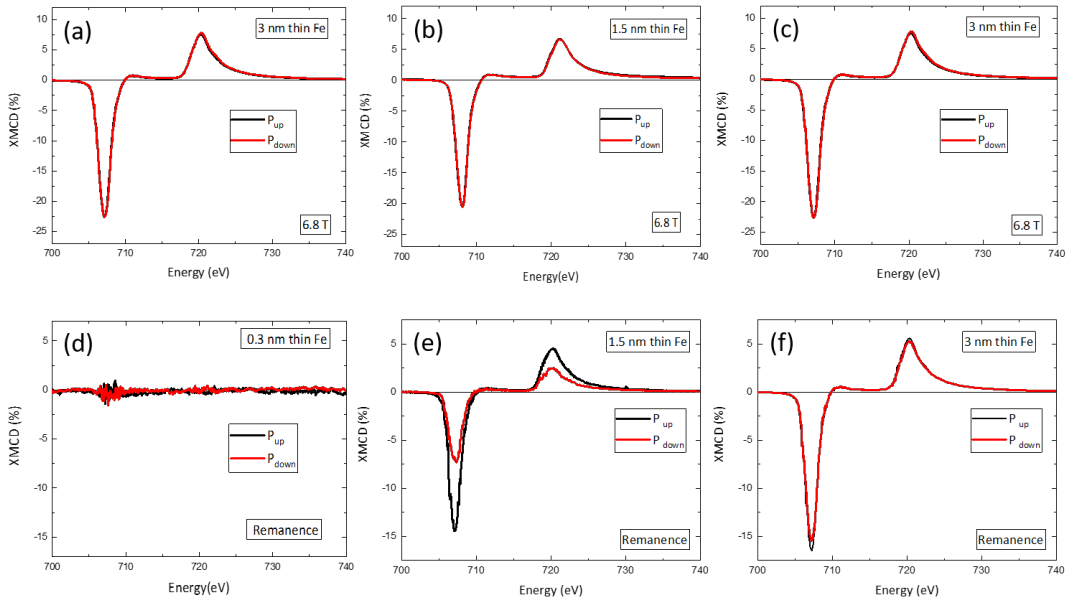

Figure 4.5 XMCD measured at Fe $L_{3,2}$-edges for 0.3 *nm* (a), 1.5 *nm* (b) and 3 *nm* (c) thin Fe in saturation at 6.8 *T*, and 0.3 *nm* (d), 1.5 *nm* (e) and 3 *nm* (f) in remanence for both FE polarizations at 3 *K*. The measurements were performed at 60° to the surface normal.

in Fig. 4.5 (e) for 1.5 *nm* thin Fe film, the XMCD in remanence is nearly 14% of the Fe L_3 XAS for P_{up} polarization and decreases to 8% for P_{down} polarization. For the 3 *nm* thin Fe film, a much smaller change in XMCD between P_{up} and P_{down} of nearly 1% of the Fe L_3 XAS is observed as shown in Fig. 4.5 (f).

Fig. 4.6 (a), (b) and (c) show the XAS for both FE polarizations of PMN-PT measured for 0.3 *nm*, 1.5 *nm* and 3 *nm* thin Fe. For the whole thickness range along the wedge, the XAS measured for Fe agrees with a metallic valence state. Comparing different FE polarization directions no change in the Fe $L_{3,2}$-edges XAS shape is observed. The observed results are therefore different from what was previously observed in Fe/MgO/Fe interface [114], where a clear oxidation of Fe is observed. In Fe/BTO interface [113] an additional peak at the Fe L_3-edge is observed and is attributed to the Fe-O hybridization.

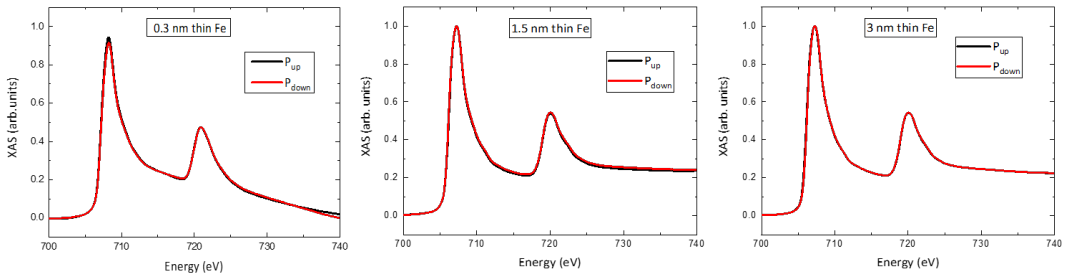

Figure 4.6 XAS measured at Fe $L_{3,2}$-edges for 0.3 *nm* (a), 1.5 *nm* (b) and 3 *nm* (c) thin Fe for both FE polarizations at 3 *K*.

The sum rules as discussed in section 3.2.2 were applied to XMCD spectra with number of 3*d* electrons in Fe of 6.61 [102] and the results are shown in Table 4.7. For the 0.3 *nm* thin Fe, the total moment is zero for both FE polarizations, and very small moment is observed in applied magnetic field. It can be seen from these values that the total remanent moment for 1.5 *nm* thin Fe is much smaller than 2.06 μ_B which was previously measured for thicker Fe films [102]. It is believed that this difference comes from the fact that Fe grows initially in islands which are not connected for the smallest thicknesses. For 1.5 *nm* thin Fe in remanence, the moment decreases from 0.90(8) μ_B to 0.71(8) μ_B by switching the FE polarization from P_{up} to P_{down}. For the 3 *nm* thin Fe film, a small change is visible in the XMCD spectra (shown in Fig. 4.5 (f)), however the calculated change in the magnetic moment from 1.95(5) μ_B to 1.85(8) μ_B is within the error bar. The saturation moments for 1.5 *nm* and 3 *nm* for both FE polarizations are shown in Table 4.7. The change in magnetic moments at the interface with charge modulation at the interface can be shown by separating the total XAS signal into two layers, which is discussed below.

Table 4.7 The effective spin moment ($m_{s,eff}$), orbital moment (m_l), and total magnetic moment (m_{tot}) per atom of Fe for 0.3 *nm*, 1.5 *nm* and 3 *nm* thin Fe in remanence and applied field for both FE polarizations along grazing incidence and at 3 *K*.

Fe nominal thickness (nm)	FE polarization	Applied Field (T)	m_l (μ_B)	$m_{s,eff}$ (μ_B)	m_{tot} (μ_B)
0.3	P_{up}	6.8	0.03(3)	0.30(6)	0.33(6)
	P_{down}		0.02(4)	0.28(4)	0.30(5)
1.5	P_{up}	0.0	0.06(5)	0.84(8)	0.90(8)
	P_{down}		0.03(5)	0.68(7)	0.71(8)
	P_{up}	6.8	0.08(4)	1.80(6)	1.88(7)
	P_{down}		0.07(5)	1.77(4)	1.84(7)
3	P_{up}	0.0	0.15(5)	1.75(3)	1.90(5)
	P_{down}		0.14(5)	1.71(7)	1.85(8)
	P_{up}	6.8	0.17(4)	1.93(2)	2.10(4)
	P_{down}		0.15(6)	1.90(3)	2.05(6)

4.1.3 Discussion

To prove the change in the magnetic moments is coming from the interface, the TEY X-ray absorption spectrum expression derived by Regan *et al.* [115] taking into account the limited probing depth from the Eq. 3.7 is used. The total XAS signal ($N(E)^{total}$) measured by TEY can be divided into the contribution from two layers, where E is the photon energy. The total signal is separated into the contribution of the top layers (TL), not affected by charge accumulation/depletion and the interfacial layer (IL), where charge accumulation/depletion may occur. Since the charge screening length of Fe is 0.13 *nm* [116], the IL is assumed to be 0.3 *nm* thin corresponding to 1 ML. So the total XAS signal is:

$$N(E)^{total} = N(E)^{TL} + N(E)^{IL} \tag{4.1}$$

The expression used to calculate the XAS signal from the top layer is given by:

$$N(E)^{TL} = I_0\ \lambda_e\ G(E)\ \mu(E)\ (1 - e^{-t_{TL}/\lambda_e}) \tag{4.2}$$

In Eq. 4.2, I_0 is the number of incident photons on the sample, $G(E)$ is the number of electrons produced per photon and t_{TL} is the thickness of the TL. Eq. 4.2 was derived by Regan *et al.* [115] for the unsaturated TEY signal since λ_e is much smaller than the X-ray penetration length give by $1/\mu(E)$. $\mu(E)$ varies between 0.5 μm and 0.04 μm in the Fe energy range from 690 eV to 750 eV. The following expression was used to calculate the XAS signal from the interfacial layer:

$$N(E)^{IL} = I_0\ G(E)\ \mu(E)\ t_{IL}\left(1 - \frac{t_{IL}}{2\lambda}\right) e^{-t_{TL}/\lambda_e} \tag{4.3}$$

In the above Eq. 4.3, t_{TL} is the thickness of the IL. Eq. 4.3 for the IL was obtained by expanding the exponential term in Eq. 4.2 up to second order. This is justified, since t_{TL} is approximately 0.3 nm which is much smaller than $\lambda_e = 1.75\ nm$. Moreover, the XAS signal from the IL is further attenuated by a factor of e^{-t_{TL}/λ_e} representing the effect from the TL. For 1.5 nm and 3 nm thickness of Fe, the TL thickness is 1.2 nm and 2.7 nm as shown in Fig. 4.8 (a) and (b), respectively. Using these values for t_{TL} and t_{IL} in the above Eq. 4.2 and 4.3, the relative contribution of the IL signal to the total signal is 12% and 4% for 1.5 nm and 3 nm thin Fe, respectively.

The total magnetic moment can also be divided into a contribution from the TL and the IL as:

$$M^{Total} = \frac{Z}{Z+1} M^{TL} + \frac{1}{Z+1} M^{IL} \tag{4.4}$$

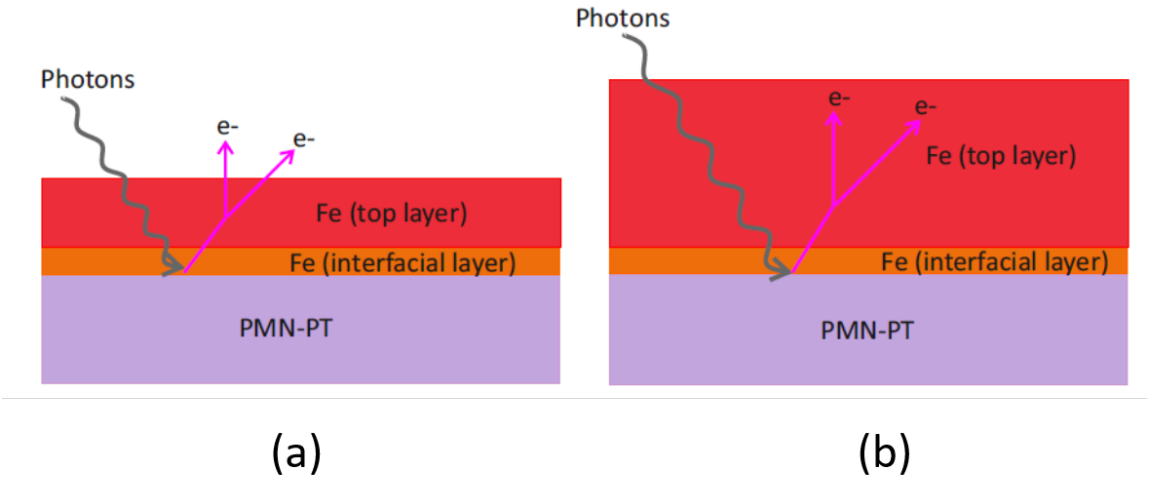

Figure 4.8 (a) TEY signal contribution from interfacial layer and top layer for (a) 1.5 *nm* and (b) 3 *nm* thin Fe.

In the above Eq. 4.4, $Z = \frac{N(E)^{TL}}{N(E)^{IL}}$, M^{TL} is the magnetic moment of TL and M^{IL} is the magnetic moment of IL. The total observed change in XMCD with FE polarization from P_{up} to P_{down} (ΔM^{Total}) i.e., $\Delta M^{Total} = M^{Total}_{P_{up}} - M^{Total}_{P_{down}}$ can be written in terms of change in magnetic moment of top layer (ΔM^{TL}) and interfacial layer (ΔM^{IL}) with FE polarization:

$$\Delta M^{Total} = \frac{Z}{Z+1}\,\Delta M^{TL} + \frac{1}{Z+1}\,\Delta M^{IL} \tag{4.5}$$

Our model assumes that the change in total magnetic moment comes from the IL only and not from the TL. Therefore, ΔM^{TL} is zero and the expression above reduces to:

$$\Delta M^{Total} = \frac{1}{Z+1}\,\Delta M^{IL} \tag{4.6}$$

Using Eq. 4.2 and 4.3, we obtain $Z \sim 7$ for 1.5 *nm* and 24 for 3 *nm*. By using the measured ΔM^{Total} for 1.5 *nm* and $Z = 7$ in Eq. 4.6 we obtain $\Delta M^{IL} = 1.52\mu_B$. Since

ΔM^{IL} is independent of the film thickness, we then obtain $\Delta M^{Total} = 0.06\ \mu_B$ for 3 nm thin Fe film. This total change of moment for 3 nm(0.06 μ_B) is comparable to the total change in moment from the sum rules (0.05 μ_B) obtained from the experiments. Therefore, the initial hypothesis that the change in magnetic moment measured occurs only at the *IL* in contact with the FE is in agreement with these calculations. As the charge accumulation and depletion is an interfacial effect due to the charge screening length of Fe, this infers that the magnetoelectric coupling observed is driven by charge modulation at the Fe/PMN-PT interface.

Since this thesis focuses on the interface effect on the magnetic properties of ultra-thin magnetic films, we extend our study by changing the capping layer to Palladium (Pd). As 1.5 nm thin Fe capped Cr show the change in magnetic moment with charge modulation at the interface by switching the FE polarization, we study the Pd capped/1.5 nm Fe/PMN-PT system in the subsequent section.

4.2 Pd capped/Fe/PMN-PT

4.2.1 Sample fabrication

The sample was grown in the X-Treme beamline preparation chamber like the Cr capped sample. Pure rods of 99.99% Fe and 99.5% Pd were loaded in the triple e-beam evaporator. In order to calibrate the evaporation rate, Fe first was evaporated using a flux of 33.3nA for 5 minutes on Au/Mica. The coverage of Fe on Au/Mica was determined using STM. An example image is shown in Fig. 4.9. Analyzing the STM image reveals that the Fe coverage is 45% of the monolayer, resulting in a deposition rate of 0.06 nm/min. The same deposition rate, just increasing the deposition time, was used to deposit Fe on PMN-PT. The Pd deposition rate was determined using a quartz balance. The flux of 140 nA was used to calibrate the

growth rate of Pd and this flux rate shows a change in frequency of $-0.84 Hz/min$ in the quartz balance, which corresponds to 0.12 nm/min. Pd was grown on Fe/PMN-PT at a flux of 140 nA for 25 minutes to get a 3 nm capping layer on the top of Fe.

Prior to the introduction in the sample preparation chamber, a bottom contact of 30 nm thick Au layer was deposited on the back of the 0.5 mm thick PMN-PT for switching the FE polarization. Inside the UHV chamber the substrate was heated up to 383 K for 30 minutes to remove the water from the surface. A Fe thickness of 1.5 nm was grown on PMN-PT with the substrate held at room temperature. The pressure during the Fe evaporation was 2×10^{-9} $mbar$. A 3 nm Pd film was grown on top of Fe to provide a continuous conductive layer acting as top electrode. The schematic of the samples is shown in Fig. 4.10. The FE polarization was switched in the preparation chamber as mentioned in the section 3.3.1, by ramping the electric field to a maximum of ± 2.2 kV/cm and the I-V curve was recorded to confirm the switching (an example of I-V curve is shown in Fig. 4.2 (b). The terms used for the FE polarization are P_{up} and P_{down} which are defined in section 4.1.1. After switching the FE polarization the sample was transferred *in-situ* to the measurement chamber. The XAS and XMCD measurements were carried out at the X-Treme beamline at SLS (discussed in section 3.3.1). The spectra were acquired in TEY mode without applied electric field to have better signal to noise ratio. The measurements were performed at a base temperature of $\sim$ 1.5 K at the cold finger which corresponds to $2-3$ K at the sample. The XAS were recorded at the Fe $L_{3,2}$ -edges in two geometries: with X-rays at an angle of 60° to the surface normal (referred as grazing incidence) and parallel to the surface normal (referred as normal incidence). The XMCD measurements were first taken in an applied magnetic field and then in remanence. The results of the XAS and XMCD spectra for both FE polarizations are discussed in next section.

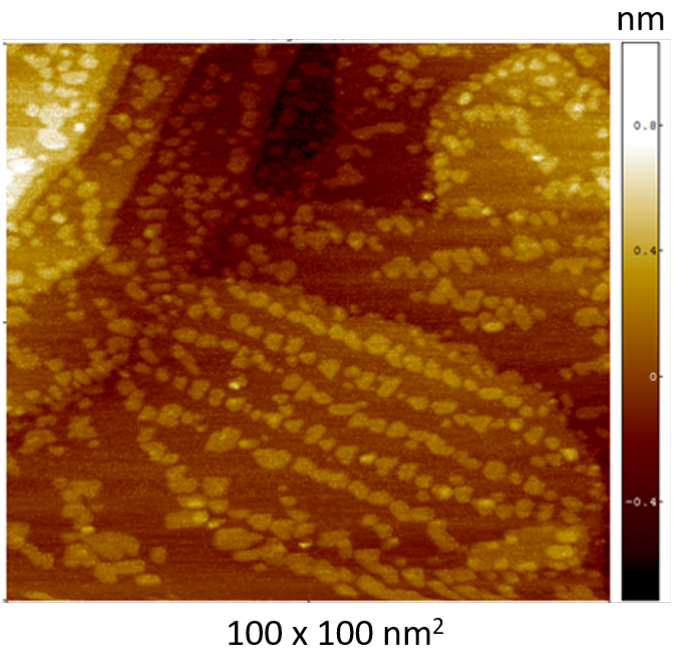

Figure 4.9 STM image of Fe on Au/Mica. The coverage of Fe is 44% of a monolayer.

4.2.2 Results and Discussion

The XAS and XMCD spectra measured along normal and grazing incidence in remanence are shown in Fig. 4.11. Along normal incidence (Fig. 4.11 (a)), the XMCD is 9.5% of the XAS maximum and along grazing incidence the XMCD is nearly 10.5% of the XAS maximum (Fig. 4.11 (b)). Fig. 4.12 depicts the hysteresis curve measured at the Fe L_3 edge along the normal and grazing incidence. No strong anisotropy is observed for Pd capped/1.5 *nm* thin Fe/PMN-PT, whereas for the Cr capped/1.5 *nm*/PMN-PT the magnetization is along the in-plane direction (discussed in section 4.1.2). From the hysteresis curve (Fig. 4.12), the saturation field along the grazing and normal incidence is 0.5 T which is the same as the Cr capped/1.5 *nm* Fe/PMN-PT.

In order to study the effect on the Fe magnetization due to the PMN-PT FE polarization, XMCD measurements were performed with FE polarization P_{up} and

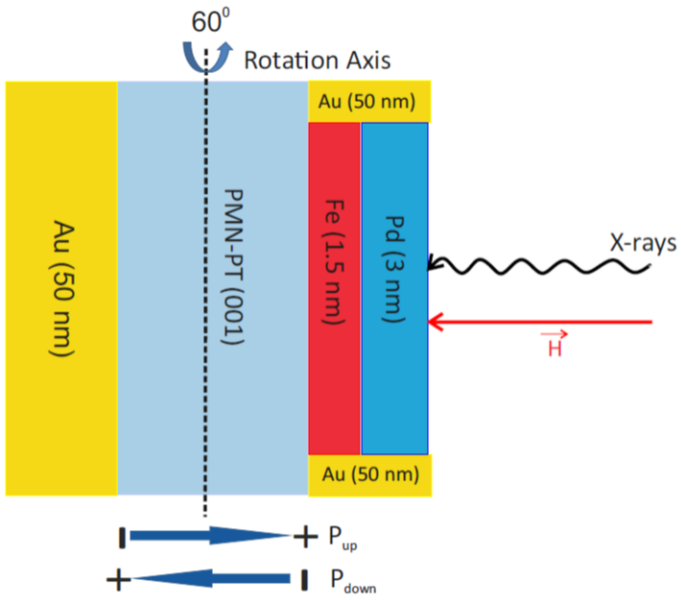

Figure 4.10 Schematic of Pd (3 *nm*)/Fe (1.5 *nm*)/PMN-PT (001) with marked directions of FE polarization vector. The X-rays impinge the sample at grazing or normal incidence

P_{down} as delineated in Fig. 4.10 in applied magnetic field of 6.8 *T* and in remanence. For P_{up} polarization, the XMCD is nearly 45% both along the normal and grazing incidence in applied magnetic field as shown in Fig. 4.13 (a). By switching the FE polarization to P_{down} (shown in Fig. 4.13 (b)), the XMCD does not change both along normal and grazing incidence in applied magnetic field.

Fig. 4.13 (c) shows that the XMCD along normal and grazing incidence is about 9.5% and 10.5%, respectively, for P_{up} polarization. By switching the FE polarization to P_{down}, the XMCD along the normal incidence reduces to 6% and the XMCD along grazing incidence increases to 12.5%. This indicates that the FE polarization is inducing an in-plane easy axis to the system. Previous work on Fe/Pd (001) have shown a PMA for Fe films with a thickness less than 2 *ML*($\sim$ 0.6 *nm*) [117, 118, 119].

The XAS for the both FE polarizations measured along the grazing and normal incidence are shown in Fig. 4.14. It is clearly seen that the XAS measured at the Fe-edge does not show any oxidation. No change in XAS shape at the Fe $L_{3,2}$-edge

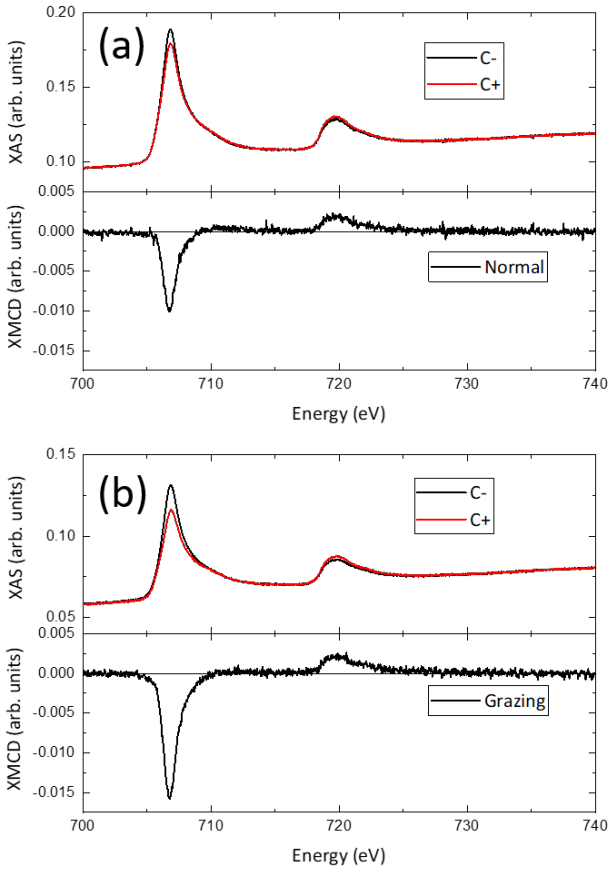

Figure 4.11 XAS and XMCD measured at the $L_{3,2}$-edges at 1.5 *nm* thin Fe with Pd capping in remanence at 3 *K* (a) at normal incidence (b) at grazing incidence.

is observed for both FE polarizations.

Sum rules were applied to the XMCD spectra using the number of 3*d* electrons of 6.61 [102] and the results are shown in table 4.15. The Fe moments in remanence are smaller compared to the moments of 1.5 *nm* and 3 *nm* thin Fe as shown for Cr capped/Fe/PMN-PT (shown in table 4.7) and as argued before we believe this comes from the Fe growth on PMN-PT i.e. Fe grows in the form of islands on the PMN-PT surface. But the saturation moments are much larger compared to the thick Fe films as discussed in section 4.1.2. In normal incidence the spin moment decreases by 27% when FE polarization is switched from P_{up} to P_{down}. On the other hand,

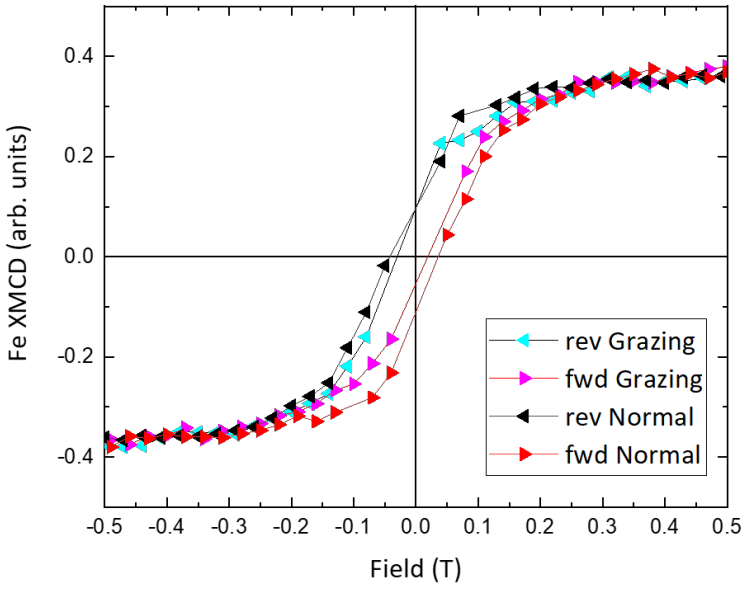

Figure 4.12 Hysteresis curve measured at the Fe L_3-edge along the normal (red line) and grazing (black) incidence.

along the grazing incidence the moment increases by 32% by switching the FE polarization from P_{up} to P_{down}. There is no significant change in the orbital moment with FE polarization switching along the grazing and normal incidence. In applied magnetic field, the $m_{s,eff}$ is the same within the error bar along normal and grazing for both FE polarizations. The total moment is larger compared to bcc Fe (2.03 μ_B). But the m_{total} is in good agreement with the previously reported results for the Pd/Fe interface [120, 121, 122]. Stoeffler *et al.* [123] performed theoretical calculations for Pd/Fe super lattices, where they predict the increase in the Fe magnetic moments at the Pd/Fe interface. This increase in moments is related to hybridization between 3*d* orbital of Fe with the 4*d* orbitals of Pd. It has also been shown that for the Fe/Pd system, there is an induced moments on the Pd [119].

Our hypothesis is that the Pd may form an alloy at the interface with the Fe as reported by Ueno *et al.* [119], which shows a PMA as predicted by Kamp *et al.*

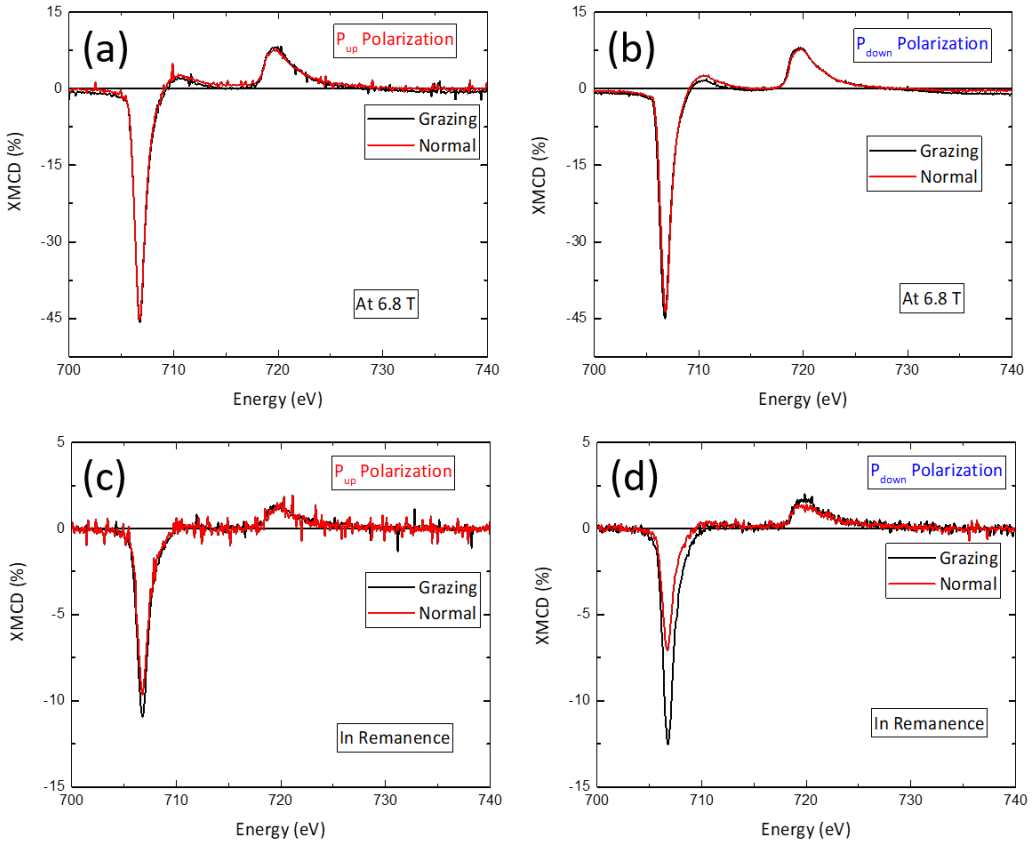

Figure 4.13 XMCD measured at the Fe $L_{3,2}$-edges for (a) P_{up} and (b) P_{down} polarization in saturation at 0.5 T. XMCD measured at the Fe $L_{3,2}$-edges for (c) P_{up} and (d) P_{down} polarization in remanence. The measurements were performed at grazing incidence (black line) and normal incidence (red line) and at 3 K

[124] and an increase in magnetic moments. We believe that the Fe thickness is critical in setting the easy axis in between the out-of-plane and in-plane direction. This behavior is quite interesting and enables to manipulate the easy axis with the FE polarization. As observed from our results, the P_{down} polarization tries to put the easy axis along the in-plane direction as observed from our results. More measurements should be carried out at different probing angles to determine the orientation of the easy axis.

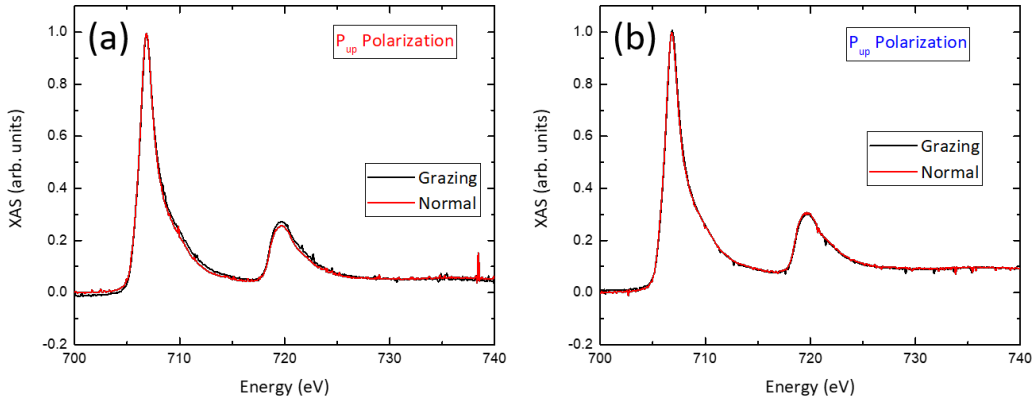

Figure 4.14 XAS measured at Fe $L_{3,2}$-edges for (a) P_{up} and (b) P_{down} polarization along grazing and normal incidence.

Table 4.15 The effective spin moment ($m_{s,eff}$), orbital moment (m_l), and total magnetic moment (m_{total}) per atom of Fe in applied field and remanence for both FE polarization along normal and grazing incidence at 3 K.

Direction	Field (T)	FE Polarization	$m_{s,eff}(\mu_B)$	$m_l(\mu_B)$	$m_{total}(\mu_B)$
Normal	0.5	P_{up}	2.16(3)	0.27(5)	2.47(5)
		P_{down}	2.13(4)	0.26(5)	2.39(6)
Grazing	0.5	P_{up}	2.20(3)	0.25(4)	2.45(5)
		P_{down}	2.28(8)	0.27(6)	2.55(9)
Normal	0.0	P_{up}	0.33(2)	0.07(6)	0.40(6)
		P_{down}	0.24(3)	0.03(4)	0.27(5)
Grazing	0.0	P_{up}	0.35(4)	0.08(4)	0.43(5)
		P_{down}	0.52(5)	0.10(1)	0.62(5)

4.3 Conclusions

The Fe/PMN-PT system shows a magneto-electrical coupling. For the Cr/Fe/PMN-PT, the in-plane magnetic moment of Fe decreases by switching the ferroelectric polarization of PMN-PT from P_{up} to P_{down}. Due to the difference in thickness of Fe and same probing depth of X-rays, the measured moment change is larger for the thinner part of the wedge as compared to the thicker part. The analysis shows that the Fe interface layer to PMN-PT is affected by the FE polarization and its magnetic moment changes by 1.50 μ_B. No change in the saturation moment but only in remanent moment is observed for 1.5 nm thin Fe, which is in agreement with a change in magnetic anisotropy. As the change in magnetic moment occurs at the interfacial layer, we attribute this effect to charge accumulation and depletion at the Fe/PMN-PT interface.

The charge accumulation and depletion at the Fe/PMN-PT interface was further studied by changing the capping layers to Pd. The Pd/Fe/PMN-PT has no strong anisotropy for P_{up} polarization. This behavior can be related to the interaction of Pd orbitals with Fe orbitals. Upon switching the ferroelectric polarization from P_{up} to P_{down} the easy axis goes towards the in-plane direction. The magnetic moments are much smaller in remanence and larger in saturation field compared to the Fe bcc. We observe a change of the magnetic anisotropy with charge modulation of the FE at the interface.

5 Effect of interfacial anisotropy in CoFeB grown on different oxides

The factors responsible for PMA in CoFeB/MgO systems were reviewed in Chapter 2.4. Endo *et al.* [33] first showed a change in coercive field for the perpendicularly magnetic system of CoFeB/MgO by electrical switching. Later, Baldrati *et al.* [125] demonstrated the electrical switching of magnetization in the artificial multiferroic CoFeB/$BaTiO_3$. These findings have motivated us to study the interfacial effect on the PMA of $Co_{40}Fe_{40}B_{20}$ (CoFeB) deposited on different oxide materials i.e. magnesium oxide (MgO), $BaTiO_3$ (BTO) and $BaxSr_{1-x}TiO_3$ (x = 0.1) (BSTO). MgO has a cubic structure and it is a dielectric, whereas BTO and BSTO have pervoskite structure and are ferroelectric materials. We observed PMA on CoFeB/MgO, and we did not observe it by depositing CoFeB on either BTO/BSTO. We explore the reasons, why we observed it on MgO but not on the pervoskite oxides. We measure the XAS and XMCD at the Fe and Co-edges for all the three systems i.e. CoFeB/MgO, CoFeB/BSTO and CoFeB/BTO at room temperature. A brief summary of the sample fabrication is first of all given in section 5.1.1. Following this, the optimization of PMA in CoFeB/MgO is described in section 5.1.2. Finally, in section 5.2, the XAS and XMCD at Fe and Co $L_{3,2}$-edges of the CoFeB/MgO system is discussed and a comparison of the XAS and XMCD of CoFeB/MgO with CoFeB/BTO and CoFeB/BSTO is shown with detailed sum rules analysis for Fe and Co atoms.

5.1 Experimental details

5.1.1 Sample growth

A 2 *nm* layer of MgO was grown on thermally oxidized Si wafer by dc magnetron sputtering (as shown in section 3.3.2) using a power of 40 *W* for 20 minutes. On top of 2 *nm* MgO, CoFeB layers with thickness of either 1.2 *nm* or 1.5 *nm* were sputtered *in-situ* using a power of 79 *W* for 36 *s* and 40 *s*, respectively. Before breaking vacuum the CoFeB was capped with 3 *nm* thick tantalum (Ta) by sputtering with a power of 79 *W* for 50 *s*. The specimens containing 1.2 *nm* and 1.5 *nm* CoFeB were cut into two pieces. One piece of each 1.2 *nm* and 1.5 *nm* CoFeB specimen were annealed at 523 *K* for half an hour on the heating stage of the sputtering machine in vacuum conditions of 2×10^{-8} *mbar*. Further, a piece of 1.2 *nm* thin CoFeB sample was annealed up to 523 *K* in magnetic field of 100 *mT*.

TiO_2 terminated BTO and BSTO thin films of thickness 8 *nm* and 7.8 *nm*, respectively, were deposited on STO (001) using pulsed laser deposition [126]. These thin films were annealed up to 873 *K* in a furnace with an O_2 pressure of 1*bar* for 2 hours to fill the oxygen vacancies on the surface of the thin films. Later, 1.2 *nm* thin CoFeB was deposited on BTO and BSTO substrates with the same parameters used for depositing CoFeB on MgO and annealed in magnetic field at 723 *K*. A schematic of the samples is shown in Fig. 5.1.

5.1.2 Optimization of PMA in CoFeB/MgO system

The XAS and XMCD were measured at the X-Treme end-station (section 3.3.1) in TEY mode to study magnetization in the CoFeB/MgO samples. The magnetization direction of the as-deposited and annealed samples with 1.2 *nm* and 1.5 *nm* thin CoFeB deposited on 2 *nm* MgO were probed by measuring the XMCD signal at

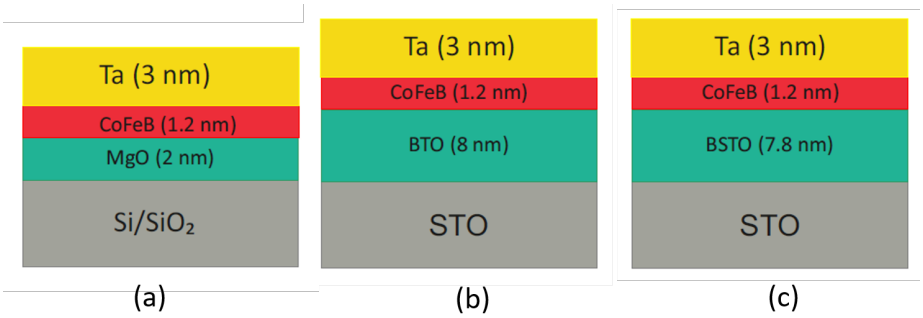

Figure 5.1 Schematic of the samples measured.

the Fe $L_{3,2}$-edges along normal and grazing incidence (60° to the surface normal). As shown in Fig. 5.2 (a), XMCD along the normal incidence measured at 0.1 T for 1.2 nm and 1.5 nm CoFeB is respectively 7% and 2% of the XAS maximum. Upon annealing, we observe an increase in the XMCD measured in normal incidence for annealed 1.2 nm thin CoFeB/MgO to 15% and no change in XMCD for 1.5 nm thin CoFeB/MgO. Along the grazing incidence the XMCD for 1.2 nm and 1.5 nm thin CoFeB is 12.5% and 25%, respectively, as shown in Fig. 5.2 (b). Upon annealing, no change in XMCD along the grazing incidence is observed for either thickness of CoFeB/MgO. This clearly shows that the 1.5 nm thin CoFeB has strong in-plane magnetization, whereas the 1.2 nm thin CoFeB has part of the magnetization along the out-of-plane direction which is in agreement with the results observed for 1.2 nm thin CoFeB/MgO [127, 128]. The as-deposited CoFeB is amorphous in nature [86]. By annealing at 523 K CoFeB crystallizes (discussed in section 2.9) leading to a PMA [129].

Fig. 5.2 (c), shows the XAS at Fe $L_{3,2}$-edges for the two thicknesses of CoFeB. By calculating the full width half width maximum (FWHM) of Fe XAS for 1.2 nm and 1.5 nm thin CoFeB/MgO, we show that for 1.2 CoFeB/MgO the Fe L_3-edge is broader i.e. 3.34 (4) compared to the Fe L_3 edge in 1.5 nm CoFeB/MgO i.e. 2.93(4). This broadening observed at the Fe XAS could be due to oxidation at the interface i.e. a Fe-O hybridization which is in agreement with previous observed results [85, 130].

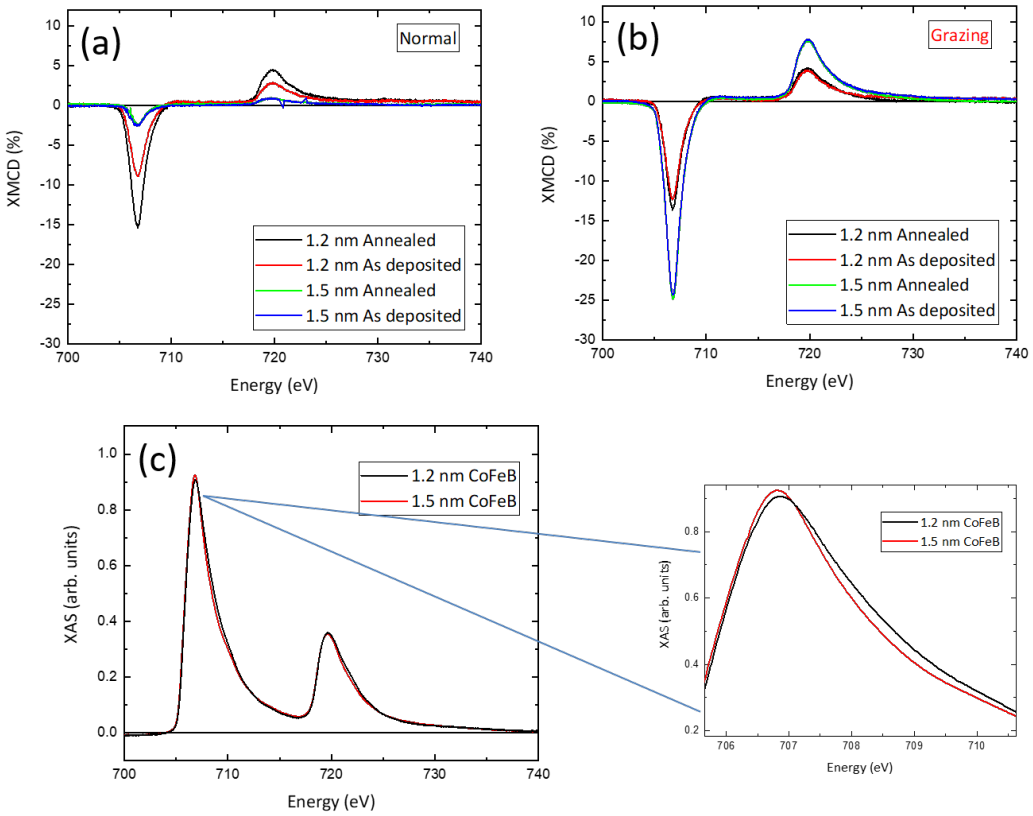

Figure 5.2 Comparison of XMCD along (a) normal incidence (b) grazing incidence for as deposited and annealed 1.2 *nm* and 1.5 *nm* thin CoFeB/MgO at room temperature and in magnetic field of 0.1 *T*, and (c) XAS for both thickness of CoFeB.

Sum rules were applied to calculate the Fe moments for both thicknesses of CoFeB/MgO by assuming the number of holes in Fe as 3.39 [102]. M/M_s is shown as a function of magnetic field in Fig. 5.3 (a) and (b) for 1.2 *nm* and 1.5 *nm* thickness of CoFeB/MgO for, as-deposited and annealed, along the grazing and normal incidence. M is the total magnetic moment by applying the sum rules to the 0.1 T data and M_s is the total magnetic moment in saturation field of 1 T. It can be seen from Fig. 5.3 (a) that at 0.1 T, M/M_s for 1.2 *nm* thin CoFeB/MgO along normal incidence clearly increases with annealing. The M/M_s ratio along the grazing incidence is the same for annealed and as deposited 1.2 *nm* thin CoFeB/MgO. For

1.5 *nm* thin CoFeB/MgO, the ratio of M/M_s is higher along the grazing incidence for the as deposited and annealed in comparison to the normal incidence. The total moment measured at 1 *T* as a function of the thickness is shown in Fig. 5.3 (c). The calculated moments are lower compared to the bulk bcc Fe and also compared to observations in other CoFeB/MgO systems [131]. The reason for low moments is attributed to a magnetic dead layer of about 0.5 *nm* at the interface between CoFeB and Ta [132, 133].

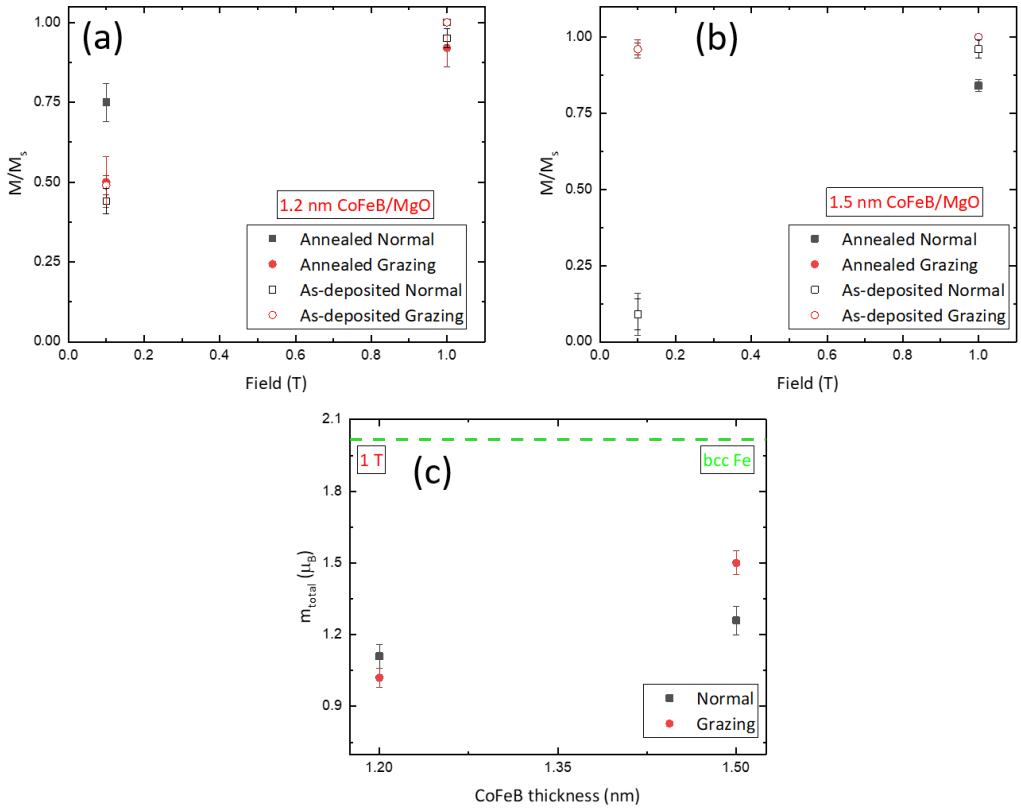

Figure 5.3 m_{total}/m_s as a function of field for as deposited and annealed (a) 1.2 *nm* and (b) 1.5 *nm* thickness of CoFeB/MgO along the normal and grazing incidence. (c) total moment as a function of thickness measured at 1 *T* along normal and grazing incidence, the green line shows the total moment of bcc Fe [102].

Annealing in magnetic field further improves the PMA of CoFeB/MgO as demon-

strated by previous work [88, 134, 135, 136, 137]. As shown in Fig. 5.4, we observe an increase in the out-of-plane remanent moments for magnetic field annealing in comparison to zero magnetic field annealing of 1.2 *nm* thin CoFeB/MgO measured using SQUID magnetometry. The saturation field is nearly 0.2 *T* for the magnetic field annealed CoFeB/MgO.

The conditions which give strongest out-of-plane magnetization are therefore a thickness of 1.2 *nm* for CoFeB, annealed at 523 *K* in magnetic field of 100 *mT*. This deposition and annealing procedure was used for all samples discussed in the subsequent section.

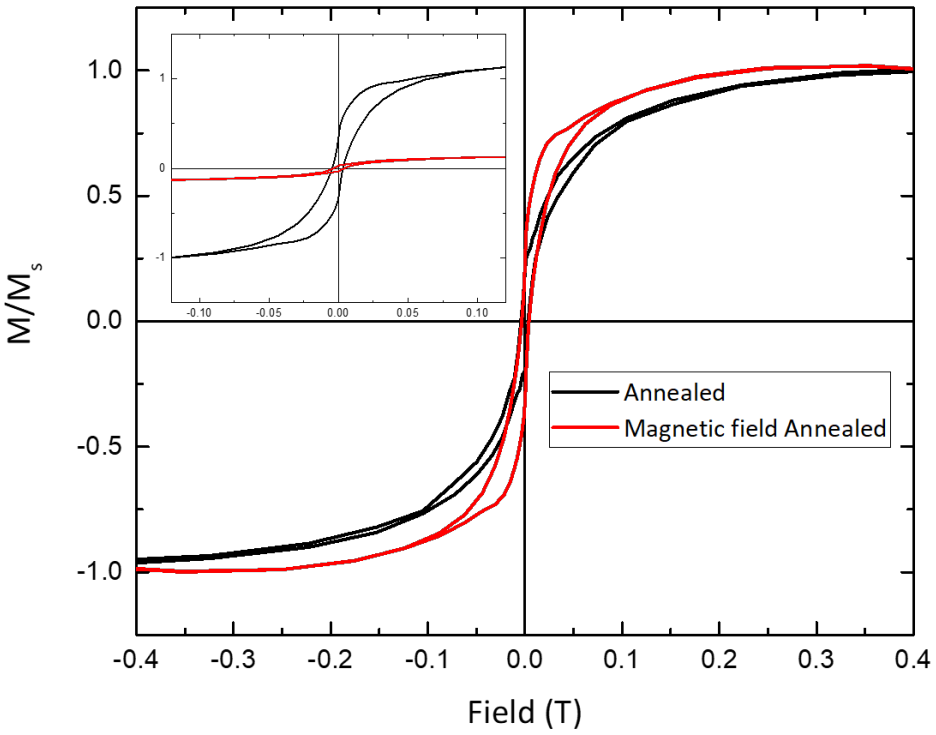

Figure 5.4 SQUID magnetization measurements along the out-of-plane direction at room temperature. The increase in remanent moments for magnetic annealing (red) in comparison to zero field annealing (black).

5.2 Results and discussion

In this section we discuss the magnetic properties of CoFeB/MgO, CoFeB/BTO and CoFeB/BSTO. All samples were prepared under the conditions which most improve the out-of-plane moments, as discussed in the previous section. XMCD was measured at Fe and Co edges in saturation field of 0.2 T and at 0.05 T. The saturation field was determined from the SQUID measurements. Since the remanence magnetic field of the superconducting magnetic coils is around $3-10\,mT$, we measured at applied field of 0.05 T, to minimize the uncertainty on the magnetic field applied to the sample. The measured XMCD and XAS at Fe and Co edges in CoFeB/BSTO and BTO are compared to the corresponding Fe and Co XMCD in CoFeB/MgO, which will be discussed in the following section.

5.2.1 Comparison of XAS and XMCD spectra for CoFeB on different oxides

Fig. 5.5 shows the XAS and XMCD measured at the Fe edge for CoFeB/MgO, BSTO and BTO. Along normal incidence, the XMCD at the Fe edge is 10% and 7.5% for CoFeB/BTO and CoFeB/BSTO, respectively, which is smaller than XMCD at the Fe for CoFeB/MgO (22%) as shown in Fig. 5.5 (b). Whereas, along the grazing incidence as shown in Fig. 5.5 (c), the XMCD of Fe for CoFeB/MgO system is smaller than the Fe XMCD for CoFeB/BSTO and BTO systems. Fig. 5.5 (a), shows the XAS at the Fe-edge for all the three systems. We do not observe any shift in energy at the Fe edge among the different samples.

Co XAS and XMCD were measured for CoFeB/BSTO and BTO and compared to the Co edge for CoFeB/MgO system as depicted in Fig. 5.6. Along the normal incidence (see Fig. 5.6(b)), the Co XMCD is 5% and 10% for CoFeB/BSTO and BTO, respectively, compared to the CoFeB/MgO system with Co XMCD signal of nearly

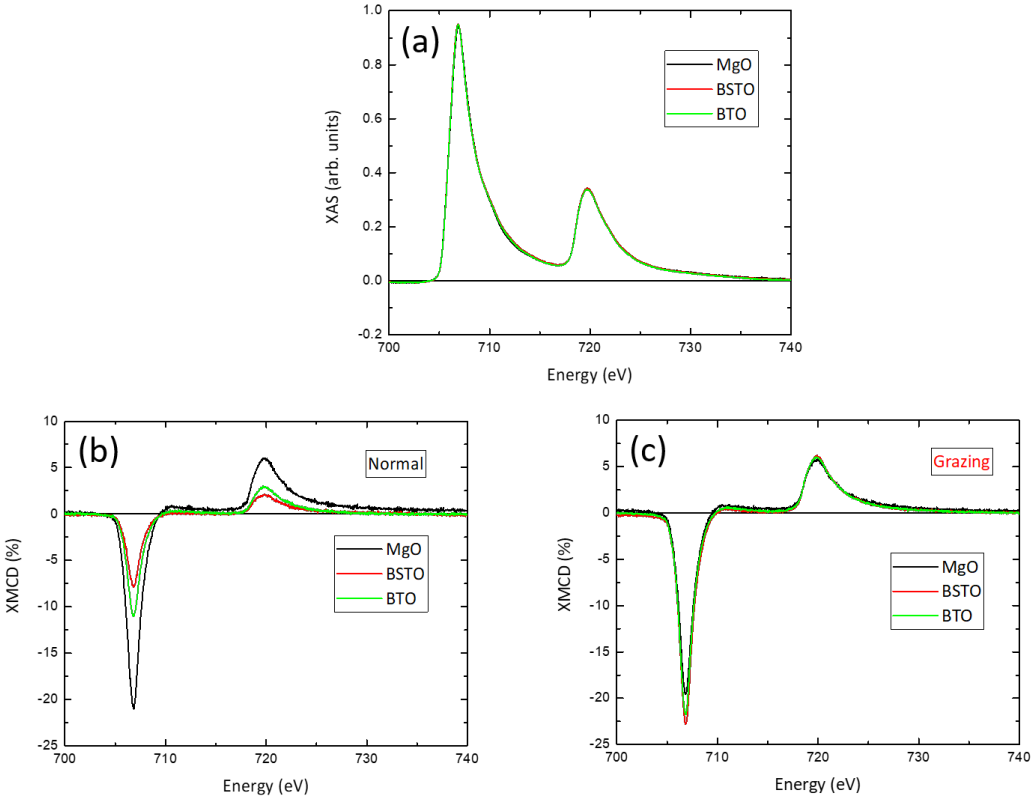

Figure 5.5 Comparison of (a) XAS (b) XMCD along normal incidence (c) XMCD along grazing incidence at Fe edge for the CoFeB/MgO, BSTO and BTO measured at room temperature in a magnetic field of 0.05 T.

21%. As shown in Fig. 5.6 (c) along the grazing incidence, the Co XMCD is higher for CoFeB/BSTO and BTO systems compared to the CoFeB/MgO system. There is no shift in the energy at the Co XAS for all the three systems. The two additional peaks in Co XAS correspond to the Ba $M_{4,5}$ edges.

The magnetization direction lies along the in-plane direction for CoFeB/BTO and BSTO system, whereas the CoFeB/MgO system has magnetization both along in-plane and out-of-plane direction. As discussed in the section 5.1.2 in Fig. 5.2 (c), we infer that there exists a Fe-O hybridization for the CoFeB/MgO system which leads to the out-of-plane magnetization. However, we observe an in-plane

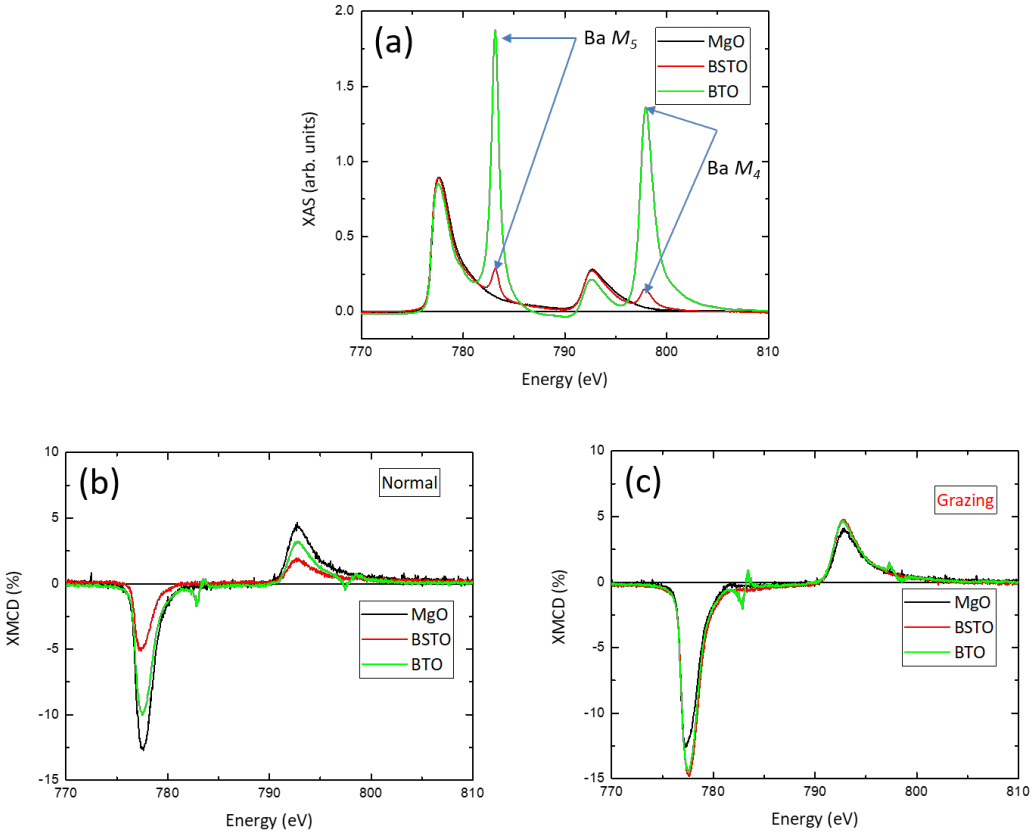

Figure 5.6 Comparison of (a) XAS (b) XMCD along normal incidence (c) XMCD along grazing incidence at Co edge for the CoFeB/MgO, BSTO and BTO measured at room temperature in a magnetic field of 0.05 T.

magnetization for CoFeB/BSTO and BTO system though there is no difference in the XAS spectra, hinting that no difference in Fe-O hybridization is observed. As MgO has a cubic structure, Fe or Co tries to occupy the oxygen sites in the cubic lattice of MgO as shown in Fig. 5.7 (a) [90]. On the other hand, BSTO and BTO have TiO_2 terminated surfaces and TiO_2 has a tetragonal structure. Fig. 5.7 (b) shows the growth of Fe on the TiO_2 terminated surface of BTO which is different from the Fe/Co growth on cubic MgO.

Sum rules were applied to calculate total moments of Fe and Co along grazing and normal incidence for all samples. As mentioned above the Co XAS superpose with

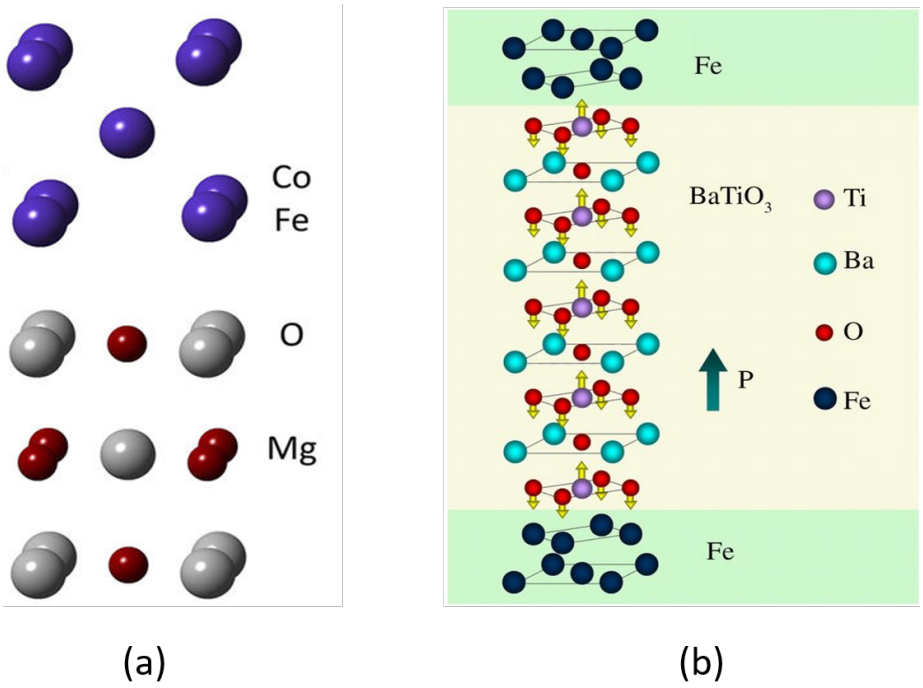

Figure 5.7 (a) Schematic for the growth of Fe or Co on MgO (b) Schematic for the growth of Fe on TiO_2 terminated surface of BTO. Figures taken from [90] and [138], respectively.

Ba $M_{4,5}$ edges, therefore calculating spin and orbital moments is difficult, since the XAS integral is difficult to calculate. So, the integrated XAS value of the Co XAS in CoFeB/MgO was used to calculate the moments of Co in CoFeB/BSTO and BTO. Though this is not a precise procedure, it provides a rough estimation of the Co moments. The n_h assumed for Fe and Co atoms were 3.31 and 2.49, respectively [102]. Fig. 5.8 (a)-(c) shows the total magnetic moment (m_{total}) as a function of magnetic field per Fe atom in the CoFeB/MgO, BSTO and BTO systems. It can be clearly seen that the total magnetic moment in saturation field is smaller compared to the bcc Fe [102]. Similarly, the total moment per Co atom as shown in Fig. 5.8 (d)-(f), for all the three systems is also smaller compared to the hcp Co [102]. The calculated m_{total} for Fe and Co atoms in CoFeB/MgO is comparable to the results shown by Ueno *et al.* [131] for Ta/CoFeB/MgO system. They observed smaller moments for Fe and Co moments are similar to ours. The saturation moments are

same for all the three systems along the normal and grazing incidence for Fe and Co atoms. The reason for such low moments compared to the bulk could be due to dead layers formed at the interface between the CoFeB/Ta interface as discussed in several publications [131, 132, 133].

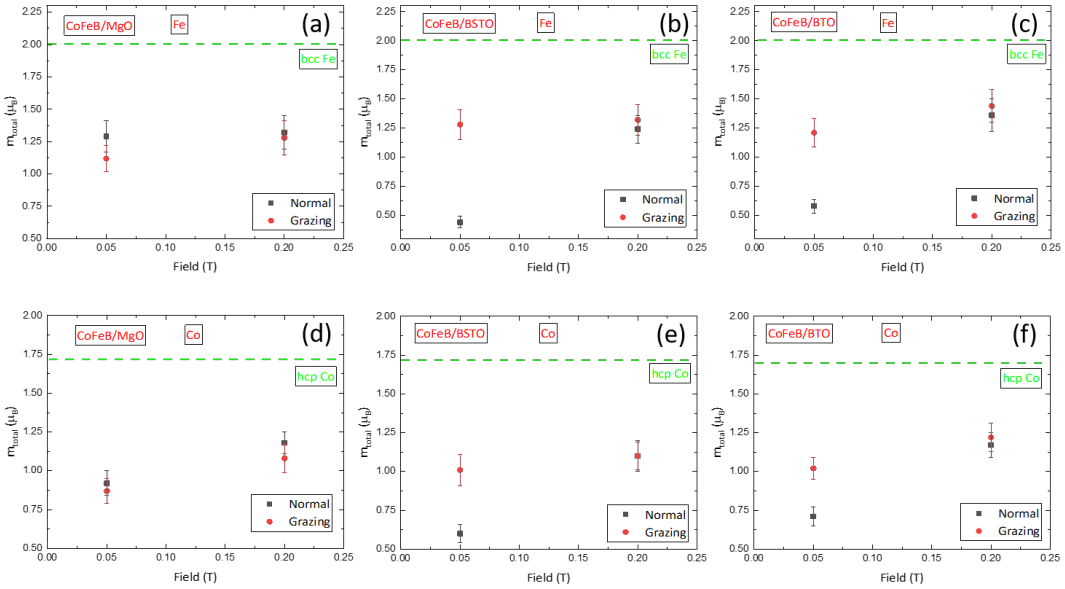

Figure 5.8 m_{total} as a function of magnetic field at the Fe edge along normal and grazing incidence for (a) CoFeB/MgO (b) CoFeB/BSTO, and (c) CoFeB/BTO. Similarly at the Co edge (d) CoFeB/MgO (e) CoFeB/BSTO, and (f) CoFeB/BTO. Measured at room temperature.

Fig. 5.9, shows the $m_{orb}/m_{s,eff}$, referred to as the relative orbital moment hereafter, along the grazing and normal incidence for Fe and Co atoms for CoFeB/MgO, CoFeB/BSTO and CoFeB/BTO systems. The relative orbital moment for Fe and Co atoms is larger compared to the bcc Fe and hcp Co [102] along the normal and grazing incidence. Along the normal incidence the relative orbital moment of Fe in CoFeB/BTO is larger than that of the CoFeB/MgO and BSTO. But along the grazing incidence the relative orbital moment of Fe in CoFeB/BTO is smaller compared to the normal incidence as shown in Fig. 5.9 (a). Whereas, the relative orbital moment

of Fe in CoFeB/MgO and BSTO are same within the error bar. These calculated relative orbital moments for Fe atom in CoFeB/MgO and BSTO are comparable to the relative orbital moment of Fe in CoFeB/MgO shown by Ueno *et al.* [131]. The relative orbital moment of Co for all the three systems is larger compared to the hcp Co [102] both along the grazing and normal incidence. The $m_{orb}/m_{s,eff}$ for Co atom is same for all the three systems and does not change along normal and grazing incidence. These results suggest that the orbital moments are enhanced for the Fe and Co atom in CoFeB compared to the Fe bcc and Co hcp. This could be originating from the interfaces, with the different oxide layers. As the symmetry of the ultra-thin magnetic films is broken at the interface with the oxides, this leads to an increase in the orbital moments. In the case of ultra-thin magnetic films like 1.2 *nm* thin CoFeB, there is a competition between the shape, interface and magnetocrystalline anisotropy. The shape anisotropy for all the systems is same but the interfacial anisotropy is dominant for CoFeB/MgO due to the growth of Fe or Co on the surface of MgO leading to an out-of-plane magnetization. But the interfacial anisotropy is dominated by shape anisotropy for growth of Fe or Co on the surface BSTO and BTO, leading to an in-plane magnetization.

5.3 Conclusions

The interfacial coupling between the CoFeB and three different oxides has been studied. The XMCD signal measured along the grazing and normal directions at the Fe and Co edges shows an magnetization both along in-plane and out-of-magnetization direction of the CoFeB/MgO system. The same thickness of CoFeB deposited on BSTO and BTO shows in-plane magnetization. This could be due to the different crystal structure of BSTO and BTO at the interface of CoFeB. The calculated moments for Fe and Co for all three systems along the grazing and

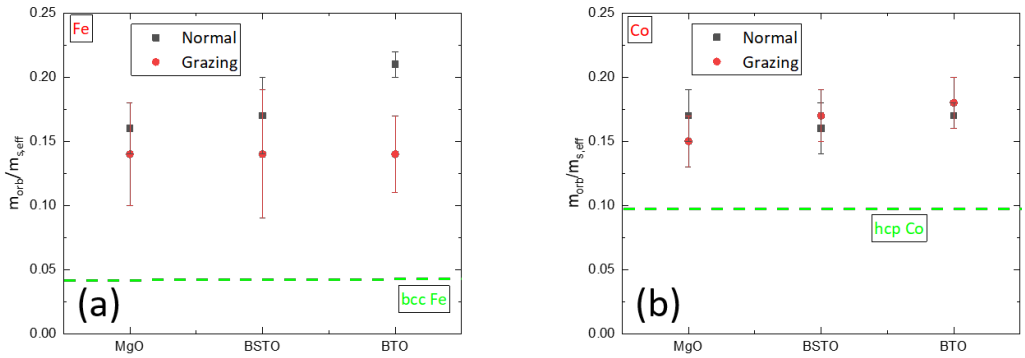

Figure 5.9 $m_{orb}/m_{s,eff}$ for CoFeB/MgO, BSTO and BTO systems (a) Fe (b) Co along the normal and grazing incidence measured at room temperature and in a magnetic field of 0.2 T.

normal incidence show smaller moments compared to the bulk metal, which could be due to a dead layer formed at the interface between CoFeB/Ta. The relative orbital moment for Fe and Co atoms in all the three system is larger compared to Fe bcc and Co hcp. This enhancement of the orbital moments is attributed to symmetry breaking at the interface with different oxides.

6 Effect of capping layers on the PMA of CoFeB/MgO system

While the previous chapter reported the change in magnetic anisotropy of CoFeB on different oxides, the following chapter investigates the effect of metal capping layers on the CoFeB/MgO system. Only few works have reported the effect of various capping layers like Mo, Ru, Pt, and Nb on the PMA of CoFeB/MgO system [11, 12, 87, 139, 140, 141]. Peng *et al.* [90, 142] used first principle calculations to calculate the magnetic anisotropy energy (MAE) for different capping materials on CoFe/MgO, showing that a proper capping material enhances PMA in the CoFe/MgO system. In this chapter, we show the change in magnetic properties of CoFeB/MgO by capping it with Ta, Pt and Ru materials. Using XMCD measurements, the magnetic moments of Fe and Co atoms were compared for all the three capping materials. Ru capping reduces the magnetic moments of Fe and Co atoms, whereas Pt capping increases the magnetic moments in comparison to the Ta capped system. XAS spectra were also measured at the Fe and Co edges for all three samples and the comparison shows a shift in energy of the XAS peak for Fe and Co. The Fe and Co moments were quantified through sum rule analysis of the XMCD spectra.

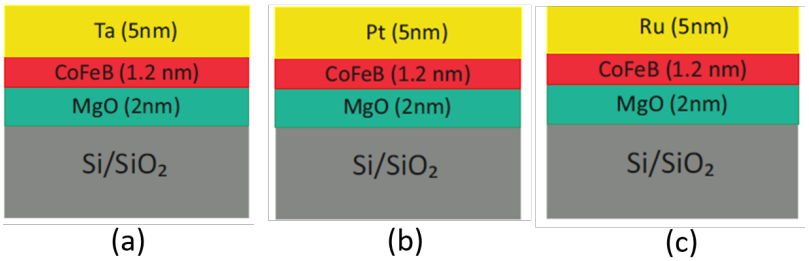

Figure 6.1 Schematic of samples with different capping materials on CoFeB/MgO (a) Ta capping (b) Pt capping (c) Ru capping.

6.1 Experimental details

6.1.1 Sample Preparation

All samples were deposited by magnetron sputtering at room temperature (discussed in section 3.3.2). A 2 *nm* layer of MgO was grown on thermally oxidized Si wafer using a power of 40 *W* for 20 minutes. CoFeB with thickness of 1.2 *nm* was sputtered *in-situ* on top of the MgO layer using a power of 79 *W* for 39 *s*. Capping materials of Ta, Pt and Ru of 5 *nm* thickness were deposited by DC sputtering using a power of 80 *W* for 50 *s*. The base pressure was better than 2 $\times 10^{-7}$ *mbar* and the working argon pressure was 2.7 *mbar*. Schematics of the samples are shown in the Fig. 6.1. The grown multilayers with different capping materials were annealed in magnetic field for half an hour on the heating stage of the sputtering machine at 723 *K*.

SQUID measurements were employed to determine the magnetization direction of CoFeB/MgO for all capping materials. The XAS and XMCD measurements were made at the Surface/Interface: Microscopy (SIM) beamline in TEY mode. A short introduction to the SIM beamline is given below.

6.1.2 XAS Experiments

The SIM beamline is equipped with two undulators to produce a high flux of soft X-rays with variable polarization. The X-ray energy range is from $200 - 2000\ eV$. The permanent end-station is the Photo-Emission Electron Microscope (PEEM), but different end-stations can be attached behind the PEEM. We used an XMCD chamber for TEY measurements, where electro-magnets are used to apply a magnetic field of $130\ mT$. The electromagnets can be rotated independent of the chamber in order to apply magnetic field in different directions. In our measurements the magnetic field was applied along the beam direction. The sample temperature can be varied from $5 - 450\ K$. All measurements shown here were carried out at room temperature. The beam spot was unfocused for the measurements and the spot size was $0.5 \times 0.5\ mm^2$. The XMCD spectra and hysteresis curve were detected in TEY in both normal incidence (sample surface is perpendicular to beam direction) and grazing incidence (sample surface is rotated 60° from the beam direction). The pressure in the end-station was in the low $10^{-7}\ mbar$ range. More details about SIM beamline can be found in this paper [143].

6.2 Results and discussions

6.2.1 SQUID measurements

The magnetization direction of the samples were determined using SQUID measurements. The Ta/CoFeB/MgO system was measured along the out-of-plane direction and the hysteresis curve at room temperature is shown in Fig. 6.2 (a).

The hysteresis curves were measured for Pt and Ru capped samples along out-of-plane and in-plane direction as shown in Fig. 6.2 (b) and (c), respectively. The easy axis of the magnetization is along the in-plane direction for the Pt and Ru

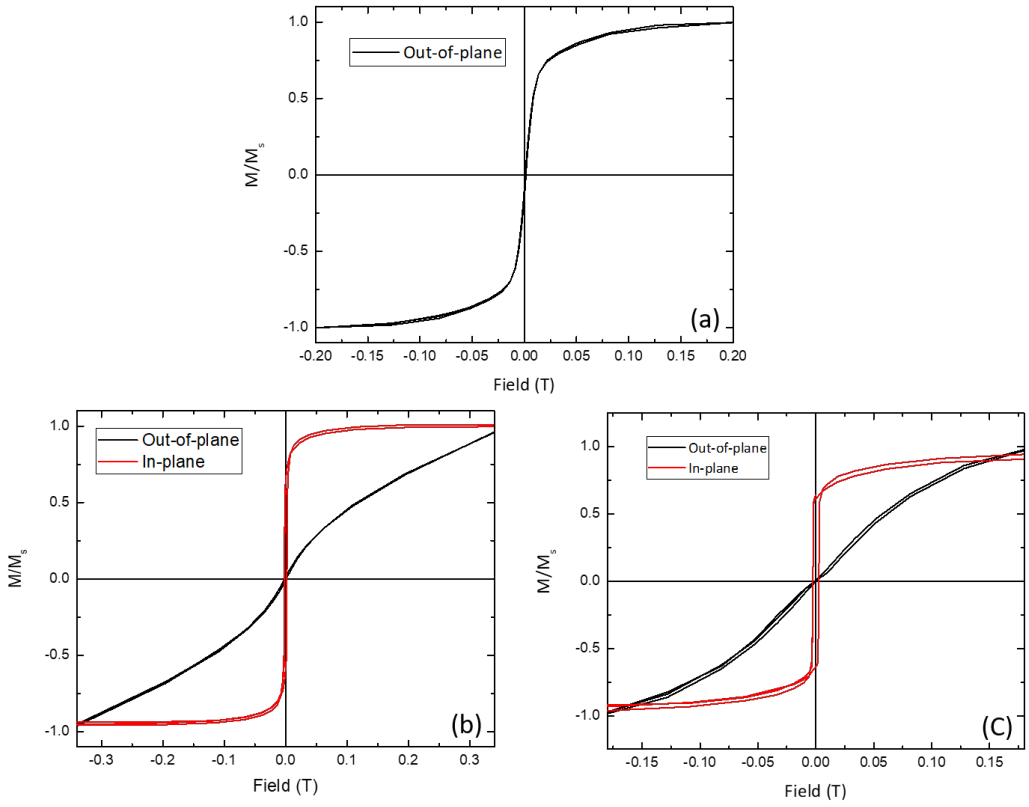

Figure 6.2 SQUID magnetization measurements for (a) Ta/CoFeB/MgO along out-of-plane, (b) Pt/CoFeB/MgO along out-of-plane and in-plane direction, and (c) Ru/CoFeB/MgO along out-of-plane and in-plane direction.

capped CoFeB/MgO, whereas Ta/CoFeB/MgO system shows magnetization along the out-of-plane direction and we expect the same behavior as reported for 3 *nm* Ta/CoFeB/MgO system in the previous chapter. In order to understand the change in the remanent moments for these three systems, the XMCD technique was employed to probe the Fe and Co edges which is discussed in the subsequent section.

6.2.2 XMCD and XAS measurements

XMCD and XAS was measured along grazing and normal incidence at room temperature and in an applied magnetic field of 0.05 T at the Fe edge for the three systems as shown in Fig. 6.3. For the Ta/CoFeB/MgO system the out-of-plane Fe XMCD is much larger compared to Pt/CoFeB/MgO and Ru/CoFeB/MgO as depicted in Fig. 6.3 (a). Along grazing incidence, as shown in Fig. 6.3 (b), we observe an increase in the Fe XMCD for Pt/CoFeB/MgO as compared to Ta/CoFeB/MgO system and a small Fe XMCD for Ru/CoFeB/MgO system. Fig. 6.3 (c) shows the XAS at the Fe edge for the three systems. It can be clearly seen that there is an energy shift at the Fe edge for the Ru capped systems in comparison to the Ta capped. More interestingly, we observe a shoulder at the Fe L_3-edge for the Ru/CoFeB/MgO system.

Fig. 6.4 shows the shift in the L_3-edge energy (ΔE) for Pt and Ru capping relative to the Ta capping. The L_3-edge energy is determined by taking the second order differentiation of the XAS as depicted in Fig. 6.4. ΔE for the Pt and Ru capped at the Fe edge is shown in the table 6.5. The Ru capped system shows a shift of Fe L_3-edge to higher energy.

Correspondingly Co XAS and XMCD were measured along the grazing and normal incidence for all the three systems as shown in Fig. 6.6. Fig. 6.6 (a) shows that along normal incidence Co XMCD for Ta/CoFeB/MgO is larger as compared to the other two capping systems. Whereas, along grazing incidence, a drastic increase in XMCD is observed for Co XMCD in Pt/CoFeB/MgO system and the XMCD for Co in Ru/CoFeB/MgO system is slightly larger compared to Ta/CoFeB/MgO system as shown in Fig. 6.3 (b). Like the Fe XAS, Co XAS was measured for all three systems as depicted in Fig. 6.6 (c). We see a clear energy shift of the Co L_3 XAS for Pt and Ru capping relative to Ta capping. Unlike the observed shoulder at the Fe L_3 edge for the Ru/CoFeB/MgO, no shoulder was observed at the Co L_3 edge. The second

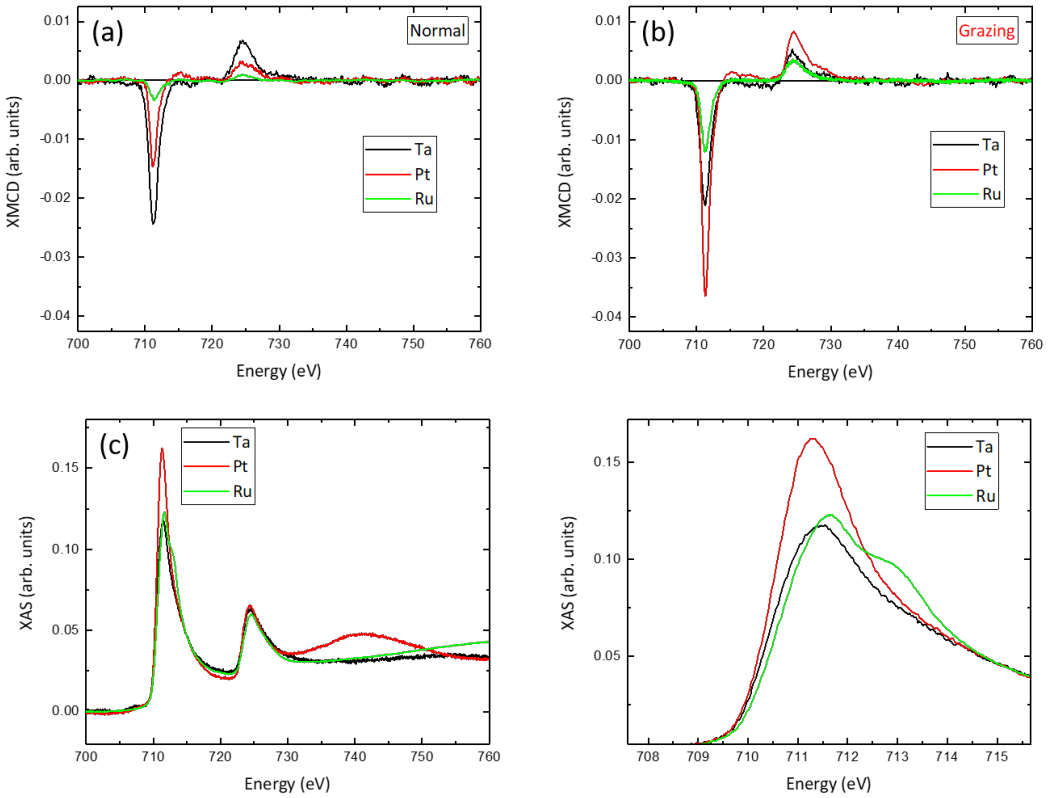

Figure 6.3 XMCD for Ta/CoFeB/MgO (black line), Pt/CoFeB/MgO (red line), and Ru/CoFeB/MgO (green line) measured at room temperature in 0.05 T at Fe $L_{2,3}$-edge (a) in normal incidence (b) in grazing incidence. (c) XAS for all three systems and the right graph shows the shift in energy at the Fe L_3-edge.

order differentiation of the Co L_3-edge XAS is shown in Fig.6.7 and the ΔE for the Pt/Ru capped sample relative to the Ta capped is shown in table 6.8. The L_3 Co edge for Pt capped is shifted by 0.35 eV to lower energy compared to Ta capped.

Sum rules were applied to determine the moments for Fe and Co atoms for all three capping systems. The n_h used to calculated the sum rules for Fe and Co are 3.39 and 2.49, respectively [102]. Fig. 6.9 shows the m_{total} for Fe and Co atoms in Ta, Pt and Ru/CoFeB/MgO. The calculated moments for Fe atoms for all three capping materials are smaller than for bcc Fe [102] as shown in Fig. 6.9 (a). The

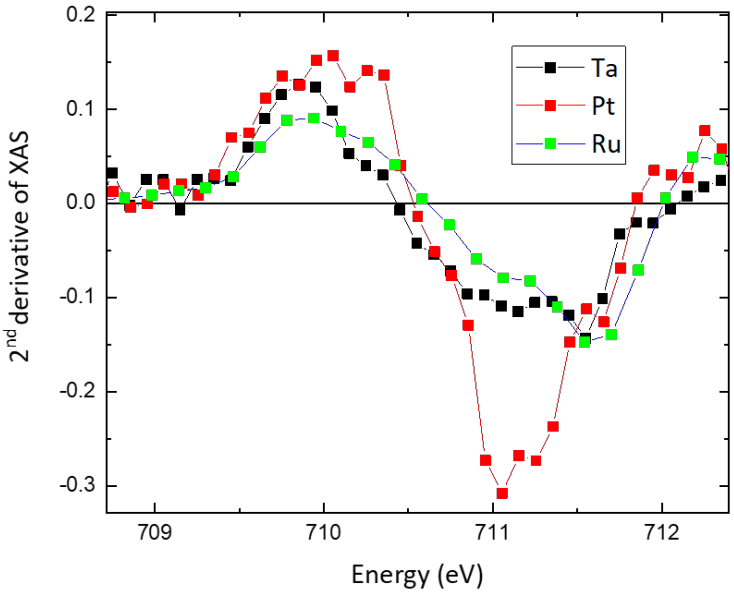

Figure 6.4 Second order differentiation of the XAS showing the inflexion point of the Fe L_3-edge peak.

moment of Fe for the Ta/CoFeB/MgO are in agreement with the previous reported results of Ta/CoFeB/MgO [131]. The Fe moment for the Pt/CoFeB/MgO along the grazing incidence are larger compared to Fe moments for Ta/CoFeB/MgO. On the other hand, the Fe moment is much smaller for the Ru capped/CoFeB/MgO. In Fig. 6.9 (b), the Co moments are shown for all capping layers in CoFeB/MgO system. Pt/CoFeB/MgO system has Co moment equivalent to the hcp Co [102] and much larger compared to the Ta and Ru capping materials. Ru/CoFeB/MgO has similar moment compared to the Ta/CoFeB/MgO system along the grazing incidence.

Table 6.5 ΔE for all the capping system at the Fe L_3-edge.

Energy (eV)	Pt capped	Ru capped
ΔE	0.10(5)	0.17(8)

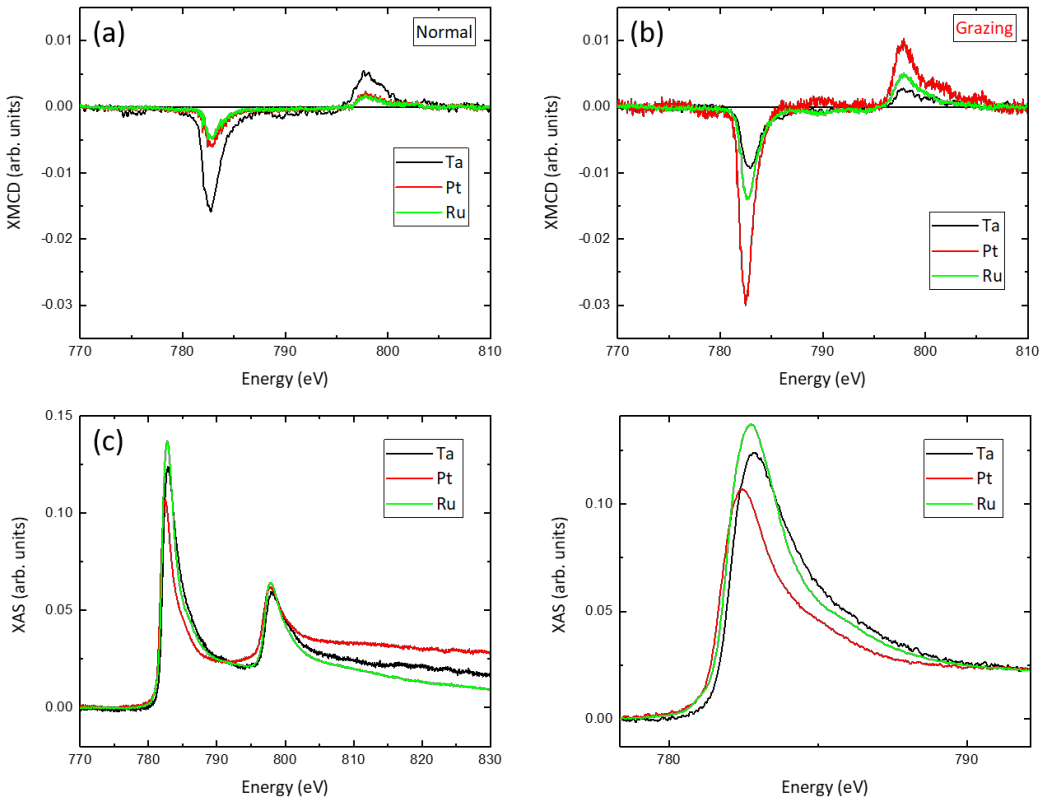

Figure 6.6 XMCD for Ta/CoFeB/MgO (black line), Pt/CoFeB/MgO (red line), and Ru/CoFeB/MgO (green line) measured at room temperature in 0.05 T at Fe $L_{2,3}$-edge (a) in normal incidence (b) in grazing incidence. (c) XAS for all three systems and the right graph shows the shift in energy at the Co L_3-edge.

The calculated moments for Ta/CoFeB/MgO system are smaller compared to the bcc Fe and hcp Co and it is due to the dead layer formed at the CoFeB/Ta interface [132, 133]. Previous work on Ru capping on CoFeB reported a low interfacial magnetic anisotropy and an in-plane magnetization [88, 90, 139, 142]. Lee *et al.* [139] showed a positive bulk crystalline anisotropy for Ru/CoFeB/MgO leading to an in-plane magnetization which they attributed to the strain in the Ru cap layer. As mentioned previously, the calculated moments for the Ru/CoFeB/MgO system are small and we believe that this could be due to charge transfer from

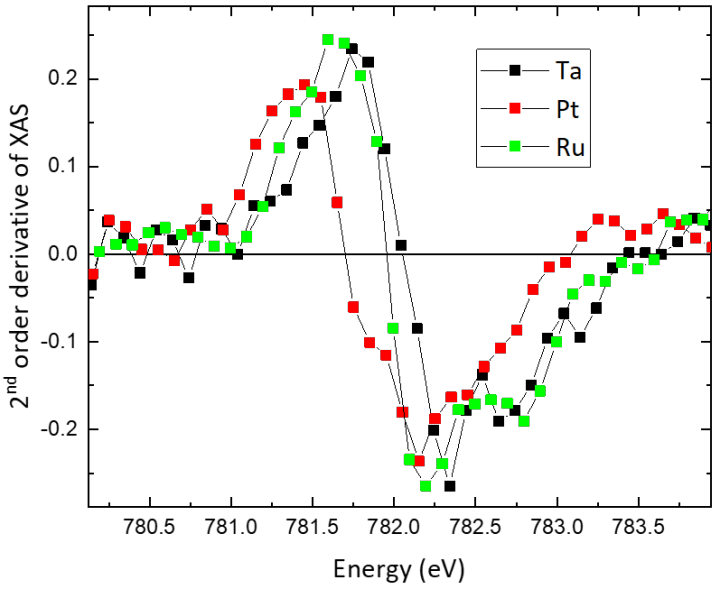

Figure 6.7 Second order differentiation of the XAS showing the inflexion point of the Co L_3-edge peak.

Table 6.8 ΔE for all the capping system at the Co L_3-edge.

Energy (eV)	Pt capped	Ru capped
ΔE	-0.35(5)	0.10(5)

the Ru capping layer to the Fe or vice-versa. Liu *et al.* [144] mentioned that Ru has rich electronic properties and it can easily donate and accept electrons. So we believe that Ru accepts electrons from Fe leading to a change in the electronic state of Fe as reflected by the shoulder at the Fe L_3-edge. Whereas, the Co XAS for the Ru/CoFeB/MgO does not show a change in the electronic of Co unlike Fe. In addition, we also measured XAS at Fe edge for the as deposited Ru/CoFeB/MgO system and no shoulder was observed at the Fe edge. This means that by annealing we observe an hybridization between Ru and Fe leading to a change in electronic state of Fe. On the other hand, we observe an increase in the Co moments for the

Pt/CoFeB/MgO systems and it could be due to no magnetic dead layer existing at the Pt/CoFeB interface as previous work reports no magnetic dead layer at the Pt/Co interface [131]. Ueno *et al.* [131] reported a shift in the Co XAS to lower energy for Pt/Co/AlO_x system and attribute this to the Co oxidation the interface. In our case, the shift in the Co XAS for the Pt/CoFeB/MgO to lower energy could be due to the interaction of Pt and Co orbitals and not due to the Co oxidation at the interface. If it is due to oxidation of Co, then a shift in the Co L_3 XAS to higher energy is observed as shown by Regan *et. al.* [145]. The reason for in-plane magnetization in the Pt/CoFeB/MgO system could be due to the 1.2 thickness of CoFeB, as previous works reported an out-of-plane magnetization for Pt capped $0.6 - 0.85$ *nm* thickness of CoFeB [6, 89, 146]. Theoretical calculations for the XAS would give a better understanding for the shift in the energy peaks and change in the magnetic moments at the Fe and Co edges.

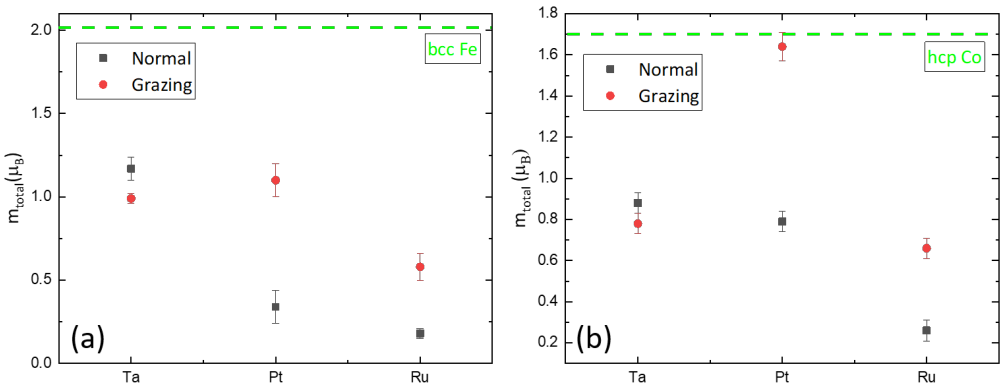

Figure 6.9 m_{total} for all the capping materials along grazing and normal incidence (a) per Fe atom (b) per Co atom. The green lines are the m_{total} for bcc Fe and hcp Co.

6.3 Conclusions

We demonstrated and studied the interfacial effect of metal capping materials with a CoFeB magnetic layer using XMCD. No out-of-plane magnetization was observed for 5 *nm* thin Ru and Pt capping materials as compared to 5 *nm* thin Ta capping. Co and Fe shows an increase in the XMCD signal for the Pt capping. We also observe a shift of Fe and Co L_3-edge XAS to lower energy. We observe a reduction in XMCD for the Ru capping which is attributed to hybridization between Ru and Fe atoms, which is reflected in the shoulder at the Fe L_3-edge. The magnetic moments for the Co atoms in the Pt capped system is equivalent to the hcp Co, but not for Fe atoms. We observe that capping layer effects the PMA in CoFeB/MgO system.

7 Conclusions

In this thesis, the changes in magnetic properties of ultra-thin magnetic films interfaced to different materials has been studied. The magnetic properties were investigated by measuring the XMCD at the Fe and Co edges and the electronic state of Fe and Co was probed by XAS.

In the first part of this work, magneto-electrical coupling between the ultra-thin Fe films on PMN-PT has been shown. For the Cr capped/Fe (0.3 – 3 *nm*)/PMN-PT, the easy axis was along the in-plane direction. By switching the FE polarization of PMN-PT from P_{up} to P_{down}, the magnetic moment of 1.5 *nm* thin Fe decreases. On the other hand, for thicker 3 *nm* thin Fe, a smaller change in magnetic moment was observed with FE switching. No remanent moment was observed for 0.3 *nm* thin Fe. The saturation moments do not change with FE polarization but only the remanent moments, which is in agreement with a change in magnetic anisotropy. Due to change in film thickness, while the probing depth of X-rays remains same, the measured moment change is larger for the 1.5 *nm* thin Fe as compared to the 3 *nm* thin Fe. As the change in magnetic moments occurs at the interfacial layer, we attribute this effect to charge modulation at the Fe/PMN-PT interface.

We have also studied Pd capped/Fe (1.5 *nm*)/PMN-PT system. In this system there is no strong anisotropy. Fe exhibits remanent magnetization both along the out-of-plane and in-plane direction. By switching the FE polarization from P_{up} to P_{down}, the remanent moment along in-plane increases while the out-of-plane moment

decreases. No change in saturation moment is observed with FE polarization but the total moments in saturation field are higher compared to the bcc Fe [102]. The electronic state of Fe does not show any change with FE polarization and it shows a metallic behavior. Further research will be required to demonstrate the reason for smaller magnetic moments of Fe compared to the bcc Fe.

In the second part of this work the magnetic properties of 1.2 *nm* thin CoFeB with different oxide interface like MgO, BSTO and BTO has been studied. XMCD signal measured at Fe and Co edges shows the isotropic behavior of Ta/CoFeB/MgO system, whereas, the magnetization is along the in-plane direction for Ta/CoFeB/BSTO and Ta/CoFeB/BTO system. The shape of the XAS at the Fe and Co edge is same for all the systems. The magnetic moments for Fe and Co are smaller compared to bcc Fe and hcp Co for all the systems and it could be due to a dead layer formed at the interface. An increase in the orbital moments for Fe and Co has been observed and it is attributed to the interface effect. BSTO has a ferroelectric phase transition the temperature of which varies with percentage of Ba in STO [59] and it would be interesting to study the change in magnetic moments of CoFeB at different temperatures for CoFeB/BSTO system.

In the last part of the thesis, the effect of metal capping on the magnetic properties of the CoFeB/MgO system has been studied. Pt and Ru were used as the capping material and the results were compared to the Ta/CoFeB/MgO system. We observe in-plane magnetization for the Pt and Ru capped samples unlike those with a Ta cap. XMCD measurements show that Fe moment are smaller for the Ru/CoFeB/MgO system and larger for Pt/CoFeB/MgO in comparison to the Ta/CoFeB/MgO system. But the total moment of Fe in all the three systems is smaller compared to the bcc Fe. The Co moments for Pt/CoFeB/MgO are the same as the hcp Co and larger than Ta/CoFeB/MgO system. Ru/CoFeB/MgO shows Co moments slightly larger than Ta/CoFeB/MgO. We also observe a shift in the energy for the XAS to

lower energy for Pt capped at Fe and Co edges in comparison to Ta capped. A shoulder at the Fe L_3-edge for Ru/CoFeB/MgO is observed and it is attributed to the interaction of Ru and Fe orbitals. Theoretical calculations have to be carried out to understand the shift in the energy and how it is related to change in the magnetic moments of Fe and Co for different capping materials. Concluding, this thesis has shown the control of magnetic properties of ultra-thin ferromagnetic films with FE polarization driven by charge modulation at the FM/FE interface. Using XAS and XMCD measurements, the magnetic moments were calculated using sum rules. The change in magnetic moments of the ultra-thin films with FE polarization and with different interfaces like oxides and metals has been studied. By our measurements we quantify the change in magnetic properties of ultra-thin FM magnetic films by varying the interfacial coupling.

Bibliography

[1] J. A. C. Bland and B. Heinrich, *Ultrathin Magnetic Structures I: An Introduction to the Electronic, Magnetic and Structural Properties*, vol. **1**. Springer Science & Business Media, 2006.

[2] J. Stöhr, *NEXAFS spectroscopy*, vol. **5**. Springer Science & Business Media, 2013.

[3] J. Stöhr and Y. Wu, *X-Ray Magnetic Circular Dichroism: Basic Concepts and Theory for* 3D *Transition Metal Atoms*, pp. 221–250. Dordrecht: Springer Netherlands, 1994.

[4] N. A. Spaldin and M. Fiebig, "The renaissance of magnetoelectric multiferroics," *Science*, vol. **309**, no. 5733, pp. 391–392, 2005.

[5] S. Valencia, A. Crassous, L. Bocher, V. Garcia, X. Moya, R. Cherifi, C. Deranlot, K. Bouzehouane, S. Fusil, A. Zobelli, *et al.*, "Interface-induced room-temperature multiferroicity in $BaTiO_3$," *Nature Materials*, vol. **10**, no. 10, pp. 753–758, 2011.

[6] S. Monso, B. Rodmacq, S. Auffret, G. Casali, F. Fettar, B. Gilles, B. Dieny, and P. Boyer, "Crossover from in-plane to perpendicular anisotropy in Pt/CoFe/AlO_x sandwiches as a function of Al oxidation: A very accurate control of the oxidation of tunnel barriers," *Applied Physics Letters*, vol. **80**, no. 22, pp. 4157–4159, 2002.

[7] S. Ikeda, K. Miura, H. Yamamoto, K. Mizunuma, H. Gan, M. Endo, S. Kanai, J. Hayakawa, F. Matsukura, and H. Ohno, "A perpendicular-anisotropy CoFeB – MgO magnetic tunnel junction," *Nature Materials*, vol. **9**, no. 9, pp. 721–724, 2010.

[8] L. E. Nistor, B. Rodmacq, C. Ducruet, C. Portemont, I. L. Prejbeanu, and B. Dieny, "Correlation between perpendicular anisotropy and magnetoresistance in magnetic tunnel junctions," *IEEE Transactions on Magnetics*, vol. **46**, pp. 1412–1415, June 2010.

[9] Y.-W. Oh, K.-D. Lee, J.-R. Jeong, and B.-G. Park, "Interfacial perpendicular magnetic anisotropy in CoFeB/MgO structure with various under layers," *Journal of Applied Physics*, vol. **115**, no. 17, p. 17C724, 2014.

[10] K. Tsumekawa, D. D. Djayaprawira, M. Nagai, H. Maehara, S. Yamagata, and N. Watanabe, "Effect of capping layer material on tunnel magnetoresistance in CoFeB – MgO – CoFeB magnetic tunnel junctions," in *INTERMAG Asia 2005. Digests of the IEEE International Magnetics Conference, 2005.*, pp. 1983–1984, April 2005.

[11] A. Natarajarathinam, Z. R. Tadisina, T. Mewes, S. Watts, E. Chen, and S. Gupta, "Influence of capping layers on CoFeB anisotropy and damping," *Journal of Applied Physics*, vol. **112**, no. 5, p. 053909, 2012.

[12] Y. Liu, K.-G. Zhu, H.-C. Zhong, Z.-Y. Zhu, T. Yu, and S.-D. Ma, "Effect of Mo capping layers thickness on the perpendicular magnetic anisotropy in MgO/CoFeB based top magnetic tunnel junction structure," *Chinese Physics B*, vol. **25**, no. 11, p. 117805, 2016.

[13] P. Weiss, "L'hypothèse du champ moléculaire et la propriété ferromagnétique," *Journal de Physique Théorique et Appliquée*, vol. **6**, no. 1, pp. 661–690, 1907.

[14] W. Heisenberg, "Zur theorie der magnetostriktion und der magnetisierungskurve," in *Original Scientific Papers Wissenschaftliche Originalar-*

beiten, pp. 598–609, Springer, 1985.

[15] J. C. Slater, "Cohesion in monovalent metals," *Physical Review*, vol. **35**, pp. 509–529, Mar 1930.

[16] J. C. Slater, "Atomic shielding constants," *Physical Review*, vol. **36**, pp. 57–64, Jul 1930.

[17] R. J. Tilley, *Understanding solids: the science of materials*. John Wiley & Sons, 2004.

[18] S. Blundell, *Magnetism in Condensed Matter (Oxford master series in condensed matter physics)*. Oxford University Press, 2001.

[19] V. Chaudhary and R. Ramanujan, "Magnetocaloric properties of Fe – Ni – Cr nanoparticles for active cooling," *Scientific Reports*, vol. **6**, 2016.

[20] A. Aharoni, *Introduction to the Theory of Ferromagnetism*, vol. **109**. Clarendon Press, 2000.

[21] R. C. O'handley, *Modern magnetic materials: principles and applications*. Wiley, 2000.

[22] J. M. Coey, *Magnetism and Magnetic Materials*. Cambridge University Press, 2010.

[23] M. Johnson, P. Bloemen, F. Den Broeder, and J. De Vries, "Magnetic anisotropy in metallic multilayers," *Reports on Progress in Physics*, vol. **59**, no. 11, p. 1409, 1996.

[24] M. Getzlaff, *Fundamentals of magnetism*. Springer Science & Business Media, 2007.

[25] B. Cullity, "Introduction to magnetic materials, addison-wesley, reading, ma, 1972," *D. Shectman, V. Van Hardeenand D. Jossel, Muter. Lett*, vol. **20**, p. 329, 1994.

[26] A. Hernando, V. Madurga, J. Barandiarán, and O. Nielsen, "Short range

order in $(Fe, Co, Ni)_{75}Si_{15}B_{10}$ amorphous alloys determined from magnetic anisotropy," *Solid State Communications*, vol. **54**, no. 12, pp. 1059–1063, 1985.

[27] C. Miguel, A. Zhukov, and J. González, "Stress and/or field induced magnetic anisotropy in the amorphous $Fe_{73.5}Cu_1Nb_3Si_{15.5}B_7$ alloy: Influence on the coercivity, saturation magnetostriction and magneto-impedance response," *Physica Status Solidi (a)*, vol. **194**, no. 1, pp. 291–303, 2002.

[28] L. Néel, "Anisotropie magnétique superficielle et surstructures d'orientation," *Journal de Physique et le Radium*, vol. **15**, no. 4, pp. 225–239, 1954.

[29] U. Gradmann and J. Müller, "Flat ferromagnetic, epitaxial 48ni/52fe (111) films of few atomic layers," *Physica Status Solidi (b)*, vol. **27**, no. 1, pp. 313–324, 1968.

[30] P. Carcia, A. Meinhaldt, and A. Suna, "Perpendicular magnetic anisotropy in Pd/Co thin film layered structures," *Applied Physics Letters*, vol. **47**, no. 2, pp. 178–180, 1985.

[31] F. J. A. den Broeder, D. Kuiper, A. P. van de Mosselaer, and W. Hoving, "Perpendicular magnetic anisotropy of Co – Au multilayers induced by interface sharpening," *Physical Review Letters*, vol. **60**, pp. 2769–2772, Jun 1988.

[32] F. den Broeder, W. Hoving, and P. Bloemen, "Magnetic anisotropy of multilayers," *Journal of Magnetism and Magnetic Materials*, vol. **93**, no. Supplement C, pp. 562 – 570, 1991.

[33] M. Endo, S. Kanai, S. Ikeda, F. Matsukura, and H. Ohno, "Electric-field effects on thickness dependent magnetic anisotropy of sputtered $MgO/Co_{40}Fe_{40}B_{20}/Ta$ structures," *Applied Physics Letters*, vol. **96**, no. 21, p. 212503, 2010.

[34] J. F. Nye and R. Lindsay, "Physical properties of crystals," *Physics Today*,

vol. **10**, p. 26, 1957.

[35] J. Valasek, "Piezo-electric and allied phenomena in rochelle salt," *Physical Review*, vol. **17**, no. 4, p. 475, 1921.

[36] T. Shimizu, K. Katayama, T. Kiguchi, A. Akama, T. J. Konno, O. Sakata, and H. Funakubo, "The demonstration of significant ferroelectricity in epitaxial Y-doped HfO_2 film," *Scientific Reports*, vol. **6**, p. 32931, 2016.

[37] R. Zhang, B. Jiang, and W. Cao, "Elastic, piezoelectric, and dielectric properties of multidomain $0.67Pb(Mg_{1/3}Nb_{2/3})O_3 - 0.33PbTiO_3$ single crystals," *Journal of Applied Physics*, vol. **90**, no. 7, pp. 3471–3475, 2001.

[38] D. Fu, H. Taniguchi, M. Itoh, S.-y. Koshihara, N. Yamamoto, and S. Mori, "Relaxor $Pb(Mg_{1/3}Nb_{2/3})O_3$: A ferroelectric with multiple inhomogeneities," *Physical Review Letters*, vol. **103**, p. 207601, Nov 2009.

[39] J. Tichỳ, J. Erhart, E. Kittinger, and J. Prívratská, *Fundamentals of piezoelectric sensorics: mechanical, dielectric, and thermodynamical properties of piezoelectric materials*. Springer Science & Business Media, 2010.

[40] D. Damjanovic, "Ferroelectric, dielectric and piezoelectric properties of ferroelectric thin films and ceramics," *Reports on Progress in Physics*, vol. **61**, no. 9, p. 1267, 1998.

[41] Y. Guo, H. Luo, D. Ling, H. Xu, T. He, and Z. Yin, "The phase transition sequence and the location of the morphotropic phase boundary region in (1-x)$[Pb(Mg_{1/3}Nb_{2/3})O_3]$-x$PbTiO_3$ single crystal," *Journal of Physics: Condensed Matter*, vol. **15**, no. 2, p. L77, 2003.

[42] W. Qiang, C. Changqing, and S. Yapeng, "Electromechanical coupling multi-axial experimental and micro-constitutive model study of $Pb(Mg_{1/3}Nb_{2/3})O_3 - 0.32PbTiO_3$ ferroelectric single crystal," in *Advances in Ferroelectrics*, InTech, 2012.

[43] D. Rajaram Patil, Y. Chai, R. C. Kambale, B.-G. Jeon, K. Yoo, J. Ryu, W.-H. Yoon, D.-S. Park, D.-Y. Jeong, S.-G. Lee, *et al.*, "Enhancement of resonant and non-resonant magnetoelectric coupling in multiferroic laminates with anisotropic piezoelectric properties," *Applied Physics Letters*, vol. **102**, no. 6, p. 062909, 2013.

[44] S. Zhang, N. P. Sherlock, R. J. M. Jr., and T. R. Shrout, "Crystallographic dependence of loss in domain engineered relaxor-PT single crystals," *Applied Physics Letters*, vol. **94**, no. 16, p. 162906, 2009.

[45] A. Von Hippel, "Ferroelectricity, domain structure, and phase transitions of barium titanate," *Reviews of Modern Physics*, vol. **22**, no. 3, p. 221, 1950.

[46] C. Carter, "Barry y norton m., grant. ceramic materials," *Science and Engineering. Springer*, 2007.

[47] S. Roberts, "Dielectric and piezoelectric properties of barium titanate," *Physical Review*, vol. **71**, pp. 890–895, Jun 1947.

[48] Y. Kim, D. Kim, J. Kim, Y. Chang, T. Noh, J. Kong, K. Char, Y. Park, S. Bu, J.-G. Yoon, *et al.*, "Critical thickness of ultra-thin ferroelectric Ba$Ti$$O_3$ films," *Applied Physics Letters*, vol. **86**, no. 10, p. 102907, 2005.

[49] N. Pertsev, A. Zembilgotov, and A. Tagantsev, "Effect of mechanical boundary conditions on phase diagrams of epitaxial ferroelectric thin films," *Physical Review Letters*, vol. **80**, no. 9, p. 1988, 1998.

[50] A. Zembilgotov, N. Pertsev, H. Kohlstedt, and R. Waser, "Ultrathin epitaxial ferroelectric films grown on compressive substrates: Competition between the surface and strain effects," *Journal of Applied Physics*, vol. **91**, no. 4, pp. 2247–2254, 2002.

[51] O. Trithaveesak, J. Schubert, and C. Buchal, "Ferroelectric properties of epitaxial $BaTiO_3$ thin films and heterostructures on different substrates,"

Journal of Applied Physics, vol. **98**, no. 11, p. 114101, 2005.

[52] A. Zembilgotov, N. Pertsev, H. Kohlstedt, and R. Waser, "Ultrathin epitaxial ferroelectric films grown on compressive substrates: Competition between the surface and strain effects," *Journal of Applied Physics*, vol. **91**, no. 4, pp. 2247–2254, 2002.

[53] H. Tabata, H. Tanaka, and T. Kawai, "Formation of artificial $BaTiO_3/SrTiO_3$ superlattices using pulsed laser deposition and their dielectric properties," *Applied Physics Letters*, vol. **65**, no. 15, pp. 1970–1972, 1994.

[54] J. Lee, L. Kim, J. Kim, D. Jung, and U. V. Waghmare, "Dielectric properties of $BaTiO_3/SrTiO_3$ ferroelectric thin film artificial lattice," *Journal of Applied Physics*, vol. **100**, no. 5, p. 051613, 2006.

[55] E. N. Bunting, G. R. Shelton, and A. S. Creamer, "Properties of barium-strontium titanate dielectrics," *Journal of the American Ceramic Society*, vol. **30**, no. 4, pp. 114–125, 1947.

[56] C. Peng and S. Krupanidhi, "Structures and electrical properties of barium strontium titanate thin films grown by multi-ion-beam reactive sputtering technique," *Journal of Materials Research*, vol. **10**, no. 3, pp. 708–726, 1995.

[57] L. Knauss, J. Pond, J. Horwitz, D. Chrisey, C. Mueller, and R. Treece, "The effect of annealing on the structure and dielectric properties of $Ba_xSr_{1-x}TiO_3$ ferroelectric thin films," *Applied Physics Letters*, vol. **69**, no. 1, pp. 25–27, 1996.

[58] W. Chang, J. S. Horwitz, A. C. Carter, J. M. Pond, S. W. Kirchoefer, C. M. Gilmore, and D. B. Chrisey, "The effect of annealing on the microwave properties of $Ba_{0.5}Sr)_{0.5}TiO_3$ thin films," *Applied Physics Letters*, vol. **74**, no. 7, pp. 1033–1035, 1999.

[59] A. Ioachim, M. Toacsan, M. Banciu, L. Nedelcu, A. Dutu, S. Antohe, C. Berbecaru, L. Georgescu, G. Stoica, and H. Alexandru, "Transitions of barium

strontium titanate ferroelectric ceramics for different strontium content," *Thin Solid Films*, vol. **515**, no. 16, pp. 6289–6293, 2007.

[60] Y. H. Fan, S. H. Yu, R. Sun, L. Li, R. X. Du, Y. S. Yin, and Y. B. Yao, "Synthesis and properties of barium strontium titanate thin films on copper foils," in *Advanced Materials Research*, vol. **47**, pp. 562–565, Trans Tech Publ, 2008.

[61] R. Ramesh and N. A. Spaldin, "Multiferroics: progress and prospects in thin films," *Nature Materials*, vol. **6**, no. 1, pp. 21–29, 2007.

[62] W. Eerenstein, M. Wiora, J. Prieto, J. Scott, and N. Mathur, "Giant sharp and persistent converse magnetoelectric effects in multiferroic epitaxial heterostructures," *Nature Materials*, vol. **6**, no. 5, p. 348, 2007.

[63] C. Thiele, K. Dörr, O. Bilani, J. Rödel, and L. Schultz, "Influence of strain on the magnetization and magnetoelectric effect in $La_{0.7}A_{0.3}MnO_3$/PMN − PT(001)(A = Sr, Ca)," *Physical Review B*, vol. **75**, no. 5, p. 054408, 2007.

[64] S. Ren and M. Wuttig, "Magnetoelectric nano-$Fe_3O_4/CoFe_2O_4||PbZr_{0.53}Ti_{0.47}O_3$ composite," *Applied Physics Letters*, vol. **92**, no. 8, p. 083502, 2008.

[65] C. Vaz, J. Hoffman, Y. Segal, J. Reiner, R. Grober, Z. Zhang, C. Ahn, and F. Walker, "Origin of the magnetoelectric coupling effect in $Pb(Zr_{0.2}Ti_{0.8})O_3/La_{0.8}Sr_{0.2}MnO_3$ multiferroic heterostructures," *Physical Review Letters*, vol. 104, no. **12**, p. 127202, 2010.

[66] J. M. Rondinelli, M. Stengel, and N. A. Spaldin, "Carrier-mediated magnetoelectricity in complex oxide heterostructures," *Nature Nanotechnology*, vol. **3**, no. 1, pp. 46–50, 2008.

[67] T. Cai, S. Ju, J. Lee, N. Sai, A. A. Demkov, Q. Niu, Z. Li, J. Shi, and E. Wang, "Magnetoelectric coupling and electric control of magnetization in ferromagnet/ferroelectric/normal-metal superlattices," *Physical Review B*,

vol. **80**, no. 14, p. 140415, 2009.

[68] T. Zhao, S. Shinde, S. Ogale, H. Zheng, T. Venkatesan, R. Ramesh, and S. D. Sarma, "Electric field effect in diluted magnetic insulator anatase Co : TiO_2," *Physical Review Letters*, vol. **94**, no. 12, p. 126601, 2005.

[69] X. He, Y. Wang, N. Wu, A. N. Caruso, E. Vescovo, K. D. Belashchenko, P. A. Dowben, and C. Binek, "Robust isothermal electric control of exchange bias at room temperature," *Nature Materials*, vol. **9**, no. 7, pp. 579–585, 2010.

[70] C. A. F. Vaz and U. Staub, "Artificial multiferroic heterostructures," *Journal of Materials Chemistry C*, vol. **1**, no. 41, pp. 6731–6742, 2013.

[71] S. Sahoo, S. Polisetty, C.-G. Duan, S. S. Jaswal, E. Y. Tsymbal, and C. Binek, "Ferroelectric control of magnetism in $BaTio_3Fe$ heterostructures via interface strain coupling," *Physical Review B*, vol. **76**, p. 092108, Sep 2007.

[72] Z. G. Sheng, J. Gao, and Y. P. Sun, "Coaction of electric field induced strain and polarization effects in $la_{0.7}ca_{0.3}mno_3$/PMN − PT structures," *Physical Review B*, vol. **79**, p. 174437, May 2009.

[73] J. J. Yang, Y. G. Zhao, H. F. Tian, L. B. Luo, H. Y. Zhang, Y. J. He, and H. S. Luo, "Electric field manipulation of magnetization at room temperature in multiferroic $CoFe_2O_4$/$Pb(Mg_{1/3}Nb_{2/3})_{0.7}Ti_{0.33}$ heterostructures," *Applied Physics Letters*, vol. **94**, no. 21, p. 212504, 2009.

[74] M. Liu, O. Obi, J. Lou, Y. Chen, Z. Cai, S. Stoute, M. Espanol, M. Lew, X. Situ, K. S. Ziemer, V. G. Harris, and N. X. Sun, "Giant electric field tuning of magnetic properties in multiferroic ferrite/ferroelectric heterostructures," *Advanced Functional Materials*, vol. **19**, no. 11, pp. 1826–1831, 2009.

[75] M. Liu, O. Obi, J. Lou, S. Stoute, Z. Cai, K. Ziemer, and N. X. Sun, "Strong magnetoelectric coupling in ferrite/ferroelectric multiferroic heterostructures derived by low temperature spin-spray deposition," *Journal of Physics D:*

Applied Physics, vol. **42**, no. 4, p. 045007, 2009.

[76] H. Béa, M. Bibes, A. Barthélémy, K. Bouzehouane, E. Jacquet, A. Khodan, J.-P. Contour, S. Fusil, F. Wyczisk, A. Forget, D. Lebeugle, D. Colson, and M. Viret, "Influence of parasitic phases on the properties of $BiFeO_3$ epitaxial thin films," *Applied Physics Letters*, vol. **87**, no. 7, p. 072508, 2005.

[77] Y.-H. Chu, L. W. Martin, M. B. Holcomb, M. Gajek, S.-J. Han, Q. He, N. Balke, C.-H. Yang, D. Lee, W. Hu, *et al.*, "Electric-field control of local ferromagnetism using a magnetoelectric multiferroic," *Nature Materials*, vol. **7**, no. 6, pp. 478–482, 2008.

[78] C.-G. Duan, S. S. Jaswal, and E. Y. Tsymbal, "Predicted magnetoelectric effect in Fe/batio$_3$ multilayers: Ferroelectric control of magnetism," *Physical Review Letters*, vol. **97**, p. 047201, Jul 2006.

[79] M. Fechner, I. V. Maznichenko, S. Ostanin, A. Ernst, J. Henk, P. Bruno, and I. Mertig, "Magnetic phase transition in two-phase multiferroics predicted from first principles," *Physical Review B*, vol. **78**, p. 212406, Dec 2008.

[80] H. J. Molegraaf, J. Hoffman, C. A. Vaz, S. Gariglio, D. Van Der Marel, C. H. Ahn, and J.-M. Triscone, "Magnetoelectric effects in complex oxides with competing ground states," *Advanced Materials*, vol. **21**, no. 34, pp. 3470–3474, 2009.

[81] C. Song, B. Cui, J. Peng, H. Mao, and F. Pan, "Electrical control of magnetism in oxides," *Chinese Physics B*, vol. **25**, no. 6, p. 067502, 2016.

[82] C. Song, B. Cui, F. Li, X. Zhou, and F. Pan, "Recent progress in voltage control of magnetism: Materials, mechanisms, and performance," *Progress in Materials Science*, vol. **87**, no. Supplement C, pp. 33 – 82, 2017.

[83] T. Liu, Y. Zhang, J. Cai, and H. Pan, "Thermally robust mo/cofeb/mgo trilayers with strong perpendicular magnetic anisotropy," *Scientific Reports*, vol. **4**,

2014.

[84] R. Shimabukuro, K. Nakamura, T. Akiyama, and T. Ito, "Electric field effects on magnetocrystalline anisotropy in ferromagnetic Fe monolayers," *Physica E: Low-dimensional Systems and Nanostructures*, vol. **42**, no. 4, pp. 1014–1017, 2010.

[85] A. Hindmarch, K. Dempsey, D. Ciudad, E. Negusse, D. Arena, and C. Marrows, "Fe diffusion, oxidation, and reduction at the CoFeB/MgO interface studied by soft x-ray absorption spectroscopy and magnetic circular dichroism," *Applied Physics Letters*, vol. **96**, no. 9, p. 092501, 2010.

[86] H. Meng, W. H. Lum, R. Sbiaa, S. Y. H. Lua, and H. K. Tan, "Annealing effects on CoFeB − MgO magnetic tunnel junctions with perpendicular anisotropy," *Journal of Applied Physics*, vol. **110**, no. 3, p. 033904, 2011.

[87] T. Liu, J. W. Cai, and L. Sun, "Large enhanced perpendicular magnetic anisotropy in CoFeB/MgO system with the typical ta buffer replaced by an hf layer," *AIP Advances*, vol. **2**, no. 3, p. 032151, 2012.

[88] D. C. Worledge, G. Hu, D. W. Abraham, J. Z. Sun, P. L. Trouilloud, J. Nowak, S. Brown, M. C. Gaidis, E. J. O'Sullivan, and R. P. Robertazzi, "Spin torque switching of perpendicular Ta/CoFeB/MgO-based mtjs," *Applied Physics Letters*, vol. **98**, no. 2, p. 022501, 2011.

[89] Z. Zhu, S. Chen, B. Zhao, Q. Y. Jin, J. Chen, and Z. Zhang, "Control of perpendicular magnetic anisotropy and spin pumping damping in MgO/CoFeB/Ta/Pt structures," *Journal of Physics D: Applied Physics*, vol. **50**, no. 35, p. 355001, 2017.

[90] S. Peng, M. Wang, H. Yang, L. Zeng, J. Nan, J. Zhou, Y. Zhang, A. Hallal, M. Chshiev, K. L. Wang, *et al.*, "Origin of interfacial perpendicular magnetic anisotropy in MgO/CoFe/metallic capping layer structures," *Scientific Reports*, vol. **5**, p. 18173, 2015.

[91] E. Beaurepaire, F. Scheurer, G. Krill, and J.-P. Kappler, *Magnetism and Synchrotron Radiation*, vol. 34. Springer, 2001.

[92] C. S. Schnohr and M. C. Ridgway, *X-ray absorption spectroscopy of semiconductors*. Springer, 2015.

[93] J. Nelsen and D. McMorrow, "Elements of modern x-ray physics," 2001.

[94] M. Abbate, J. Goedkoop, F. De Groot, M. Grioni, J. Fuggle, S. Hofmann, H. Petersen, and M. Sacchi, "Probing depth of soft x-ray absorption spectroscopy measured in total-electron-yield mode," *Surface and Interface Analysis*, vol. **18**, no. 1, pp. 65–69, 1992.

[95] R. Nakajima, J. Stöhr, and Y. U. Idzerda, "Electron-yield saturation effects in l-edge x-ray magnetic circular dichroism spectra of Fe, Co, *and* Ni," *Physical Review B*, vol. **59**, pp. 6421–6429, Mar 1999.

[96] J. Stöhr and H. C. Siegmann, *Magnetism: from fundamentals to nanoscale dynamics*, vol. 152. Springer Science & Business Media, 2007.

[97] E. U. Condon and G. H. Shortley, *The theory of atomic spectra*. Cambridge University Press, 1951.

[98] J. C. Slater, "Quantum theory of atomic structure," tech. rep., 1960.

[99] G. van der Laan and A. I. Figueroa, "X-ray magnetic circular dichroism—a versatile tool to study magnetism," *Coordination Chemistry Reviews*, vol. **277-278**, no. Supplement C, pp. 95 – 129, 2014. Following Chemical Structures using Synchrotron Radiation.

[100] B. T. Thole, P. Carra, F. Sette, and G. van der Laan, "X-ray circular dichroism as a probe of orbital magnetization," *Physical Review Letters*, vol. **68**, pp. 1943–1946, Mar 1992.

[101] P. Carra, B. T. Thole, M. Altarelli, and X. Wang, "X-ray circular dichroism and local magnetic fields," *Physical Reviews Letters*, vol. **70**, pp. 694–697, Feb 1993.

[102] C. T. Chen, Y. U. Idzerda, H.-J. Lin, N. V. Smith, G. Meigs, E. Chaban, G. H. Ho, E. Pellegrin, and F. Sette, "Experimental confirmation of the x-ray magnetic circular dichroism sum rules for iron and cobalt," *Physical Review Letters*, vol. **75**, pp. 152–155, Jul 1995.

[103] C. Piamonteze, P. Miedema, and F. M. F. de Groot, "The accuracy of the spin sum rule in xmcd," *Journal of Physics: Conference Series*, vol. **190**, no. 1, p. 012015, 2009.

[104] S. Sasaki, K. Miyata, and T. Takada, "A new undulator for generating variably polarized radiation," *Japanese Journal of Applied Physics*, vol. **31**, no. 12B, p. L1794, 1992.

[105] C. Piamonteze, U. Flechsig, S. Rusponi, J. Dreiser, J. Heidler, M. Schmidt, R. Wetter, M. Calvi, T. Schmidt, H. Pruchova, *et al.*, "X-treme beamline at sls: X-ray magnetic circular and linear dichroism at high field and low temperature," *Journal of Synchrotron Radiation*, vol. **19**, no. 5, pp. 661–674, 2012.

[106] P. Kelly and R. Arnell, "Magnetron sputtering: a review of recent developments and applications," *Vacuum*, vol. **56**, no. 3, pp. 159–172, 2000.

[107] S. Swann, "Magnetron sputtering," *Physics in Technology*, vol. **19**, no. 2, p. 67, 1988.

[108] J. Clarke and A. I. Braginski, *The SQUID Handbook: Applications of SQUIDs and SQUID Systems*. John Wiley & Sons, 2006.

[109] R. Fagaly, "Superconducting quantum interference device instruments and applications," *Review of Scientific Instruments*, vol. **77**, no. 10, p. 101101, 2006.

[110] J. Heidler, M. Fechner, R. V. Chopdekar, C. Piamonteze, J. Dreiser, C. A. Jenkins, E. Arenholz, S. Rusponi, H. Brune, N. A. Spaldin, and F. Nolting, "Magnetoelectroelastic control of magnetism in an artificial multiferroic,"

Physical Review B, vol. **94**, no. 1, p. 014401, 2016.

[111] J. Vogel, A. Fontaine, V. Cros, F. Petroff, J.-P. Kappler, G. Krill, A. Rogalev, and J. Goulon, "Palladium magnetism in Pd/Fe multilayers studied by xmcd at the $PdL_{2,3}$ edges," *Journal of Magnetism and Magnetic Materials*, vol. **165**, no. 1-3, pp. 96–99, 1997.

[112] S. R. V. Avula, J. Heidler, J. Dreiser, J. Vijayakumar, L. Howald, F. Nolting, and C. Piamonteze, "Study of magneto-electric coupling between ultra-thin films and PMN – PT using x-ray magnetic circular dichroism," *Journal of Applied Physics*, vol. **123**, no. 6, p. 064103, 2018.

[113] G. Radaelli, D. Petti, E. Plekhanov, I. Fina, P. Torelli, B. Salles, M. Cantoni, C. Rinaldi, D. Gutiérrez, G. Panaccione, *et al.*, "Electric control of magnetism at the Fe/$BaTiO_3$ interface," *Nature Communications*, vol. **5**, p. 3404, 2014.

[114] S. Gautam, K. Asokan, J. Pal Singh, F.-H. Chang, H.-J. Lin, and K. Hwa Chae, "Electronic structure of Fe/MgO/Fe multilayer stack by xmcd," *Journal of Applied Physics*, vol. **115**, no. 17, p. 17C109, 2014.

[115] T. J. Regan, H. Ohldag, C. Stamm, F. Nolting, J. Lüning, J. Stöhr, and R. L. White, "Chemical effects at metal/oxide interfaces studied by x-ray-absorption spectroscopy," *Physical Review B*, vol. **64**, p. 214422, Nov 2001.

[116] S. Zhang, "Spin-dependent surface screening in ferromagnets and magnetic tunnel junctions," *Physical Review Letters*, vol. **83**, pp. 640–643, 1999.

[117] C. Liu and S. D. Bader, "Morphology of Fe/Pd(100) films studied using photo emission from physisorbed xe," *Physical Review B*, vol. **44**, pp. 2205–2208, Aug 1991.

[118] C. Liu and S. Bader, "Magnetic properties of ultrathin epitaxial films of iron," *Journal of Magnetism and Magnetic Materials*, vol. **93**, no. Supplement C, pp. 307 – 314, 1991.

[119] T. Ueno, M. Sawada, K. Furumoto, T. Tagashira, S. Tohoda, A. Kimura, S. Haraguchi, M. Tsujikawa, T. Oda, H. Namatame, and M. Taniguchi, "Interface atomic structures and magnetic anisotropy of Fe and Pd/*Fe* mono atomic films on Pd(001)," *Physical Review B*, vol. **85**, p. 224406, Jun 2012.

[120] X. Le Cann, C. Boeglin, B. Carriere, and K. Hricovini, "Magnetic linear and circular dichroism in core-level photoemission and magnetic circular x-ray dichroism in absorption for ultrathin films Fe/Pd(100)," *Physical Review B*, vol. **54**, no. 1, p. 373, 1996.

[121] J. Bland, C. Daboo, B. Heinrich, Z. Celinski, and R. Bateson, "Enhanced magnetic moments in bcc Fe films," *Physical Review B*, vol. **51**, no. 1, p. 258, 1995.

[122] Z. Celinski, B. Heinrich, J. F. Cochran, W. B. Muir, A. S. Arrott, and J. Kirschner, "Growth and magnetic studies of lattice expanded Pd in ultrathin Fe(001)/Pd(001)/Fe(001) structures," *Physical Review Letters*, vol. **65**, pp. 1156–1159, Aug 1990.

[123] D. Stoeffler, K. Ounadjela, J. Sticht, and F. Gautier, "Magnetic polarization of the pd spacer and inter layer magnetic couplings in Fe/Pd (001) superlattices: First principles calculations," *Physical Review B*, vol. **49**, pp. 299–309, Jan 1994.

[124] P. Kamp, A. Marty, B. Gilles, R. Hoffmann, S. Marchesini, M. Belakhovsky, C. Boeglin, H. Dürr, S. Dhesi, G. Van der Laan, *et al.*, "Correlation of spin and orbital anisotropies with chemical order in $Fe_{0.5}Pd_{0.5}$ alloy films using magnetic circular x-ray dichroism," *Physical Review B*, vol. **59**, no. 2, p. 1105, 1999.

[125] L. Baldrati, C. Rinaldi, A. Manuzzi, M. Asa, L. Aballe, M. Foerster, N. Biškup, M. Varela, M. Cantoni, and R. Bertacco, "Electrical switching of magnetization in the artificial multiferroic CoFeB/$BaTiO_3$," *Advanced Electronic Materials*, vol. **2**, no. 7, 2016.

[126] S. P. Muff, *Manipulation of the Two-Dimensional States at Titanates Surfaces studied by* ARPES. PhD thesis, EPFL, Laussane, 2017.

[127] P. G. Gowtham, G. M. Stiehl, D. C. Ralph, and R. A. Buhrman, "Thickness-dependent magnetoelasticity and its effects on perpendicular magnetic anisotropy in Ta/CoFeB/MgO thin films," *Physical Review B*, vol. **93**, p. 024404, Jan 2016.

[128] K. Lee, J. J. Sapan, S. H. Kang, and E. E. Fullerton, "Perpendicular magnetization of CoFeB on single-crystal MgO," *Journal of Applied Physics*, vol. **109**, no. 12, p. 123910, 2011.

[129] J. Bae, W. Lim, H. Kim, T. Lee, K. Kim, and T. Kim, "Compositional change of mgo barrier and interface in CoFeB/MgO/CoFeB tunnel junction after annealing," *Journal of Applied Physics*, vol. **99**, no. 8, p. 08T316, 2006.

[130] W. C. Tsai, S. C. Liao, H. C. Hou, C. T. Yen, Y. H. Wang, H. M. Tsai, F. H. Chang, H. J. Lin, and C.-H. Lai, "Investigation of perpendicular magnetic anisotropy of CoFeB by x-ray magnetic circular dichroism," *Applied Physics Letters*, vol. **100**, no. 17, p. 172414, 2012.

[131] T. Ueno, J. Sinha, N. Inami, Y. Takeichi, S. Mitani, K. Ono, and M. Hayashi, "Enhanced orbital magnetic moments in magnetic heterostructures with interface perpendicular magnetic anisotropy," *Scientific Reports*, vol. **5**, 2015.

[132] W. Wang, Y. Yang, H. Naganuma, Y. Ando, R. Yu, and X. Han, "The perpendicular anisotropy of $Co_{40}Fe_{40}B_{20}$ sandwiched between ta and mgo layers and its application in CoFeB/MgO/CoFeB tunnel junction," *Applied Physics Letters*, vol. **9**9, no. 1, p. 012502, 2011.

[133] S. Y. Jang, C.-Y. You, S. H. Lim, and S. R. Lee, "Annealing effects on the magnetic dead layer and saturation magnetization in unit structures relevant to a synthetic ferrimagnetic free structure," *Journal of Applied Physics*, vol. **109**, no. 1, p. 013901, 2011.

[134] V. Sokalski, M. T. Moneck, E. Yang, and J.-G. Zhu, "Optimization of Ta thickness for perpendicular magnetic tunnel junction applications in the MgO – FeCoB – Ta system," *Applied Physics Letters*, vol. **101**, no. 7, p. 072411, 2012.

[135] M. Yamanouchi, R. Koizumi, S. Ikeda, H. Sato, K. Mizunuma, K. Miura, H. Gan, F. Matsukura, and H. Ohno, "Dependence of magnetic anisotropy on MgO thickness and buffer layer in $Co_{20}Fe_{60}B_{20}$ – MgO structure," *Journal of Applied Physics*, vol. **109**, no. 7, p. 07C712, 2011.

[136] V. Sokalski, D. M. Bromberg, M. T. Moneck, E. Yang, and J.-G. Zhu, "Increased perpendicular tmr in FeCoB/MgO/FeCoB magnetic tunnel junctions by seed layer modifications," *IEEE Transactions on Magnetics*, vol. **49**, no. 7, pp. 4383–4385, 2013.

[137] Y. Liu, L. Hao, and J. Cao, "Effect of annealing conditions on the perpendicular magnetic anisotropy of Ta/CoFeB/MgO multilayers," *AIP Advances*, vol. **6**, no. 4, p. 045008, 2016.

[138] J. D. Burton and E. Y. Tsymbal, "Magnetoelectric interfaces and spin transport," *Philosophical Transactions of the Royal Society of London A: Mathematical, Physical and Engineering Sciences*, vol. **370**, no. 1977, pp. 4840–4855, 2012.

[139] D. S. Lee, H. T. Chang, C. W. Cheng, and G. Chern, "Perpendicular magnetic anisotropy in MgO/CoFeB/Nb and a comparison of the cap layer effect," *IEEE Transactions on Magnetics*, vol. **50**, pp. 1–4, July 2014.

[140] H. Głowiński, A. Żywczak, J. Wrona, A. Krysztofik, I. Gościańska, T. Stobiecki, and J. Dubowik, "CoFeB/MgO/CoFeB structures with orthogonal easy axes: perpendicular anisotropy and damping," *Journal of Physics: Condensed Matter*, vol. **29**, no. 48, p. 485803, 2017.

[141] T.-I. Cheng, C.-W. Cheng, and G. Chern, "Perpendicular magnetic anisotropy induced by a cap layer in ultra thin MgO/CoFeB/Nb," *Journal of Applied*

Physics, vol. **112**, no. 3, p. 033910, 2012.

[142] S. Peng, W. Zhao, J. Qiao, L. Su, J. Zhou, H. Yang, Q. Zhang, Y. Zhang, C. Grezes, P. K. Amiri, and K. L. Wang, "Giant interfacial perpendicular magnetic anisotropy in MgO/CoFe/capping layer structures," *Applied Physics Letters*, vol. **110**, no. 7, p. 072403, 2017.

[143] U. Flechsig, F. Nolting, A. F. Rodríguez, J. Krempaský, C. Quitmann, T. Schmidt, S. Spielmann, and D. Zimoch, "Performance measurements at the sls sim beamline," *AIP Conference Proceedings*, vol. **1234**, no. 1, pp. 319–322, 2010.

[144] Y. Liu, J. Zhang, S. Wang, S. Jiang, Q. Liu, X. Li, Z. Wu, and G. Yu, "Ru catalyst-induced perpendicular magnetic anisotropy in '*mathrmMgO*/*CoFeB*/*Ta*/*MgO* multilayered films," *ACS Applied Materials & Interfaces*, vol. **7**, no. 48, pp. 26643–26648, 2015.

[145] T. J. Regan, H. Ohldag, C. Stamm, F. Nolting, J. Lüning, J. Stöhr, and R. L. White, "Chemical effects at metal/oxide interfaces studied by x-ray-absorption spectroscopy," *Physical Review B*, vol. **64**, p. 214422, Nov 2001.

[146] H. K. Gweon, S. J. Yun, and S. H. Lim, "A very large perpendicular magnetic anisotropy in Pt/Co/MgO trilayers fabricated by controlling the MgO sputtering power and its thickness," *Scientific Reports*, vol. **8**, no. 1, p. 1266, 2018.

Acknowledgements

First and foremost, I extend my gratitude to my supervisor Dr. Cinthia Piamonteze for giving me an opportunity to spend a gainful and an exciting environment to work. She introduced me to secrets of synchrotron sources, XAS, XMCD and vacuum systems. Cinthia, influenced me in systematic approach to experiments and solving problems. I also thank her two little ones (Luana and Lino, who were born during my Phd) for letting their beloved mom to give time for me. Without her experience, guidance and knowledge the work in this thesis could not have been possible. Thank you a lot for being patient with me. In short, she is simply "Supercalifragilisticexpialidocious". I also would like thank Prof. Dr. Frithjof Nolting "Enchanting" for his impeccable insights and steady interest in the progress of the projects. He spend countless amount of time in reviewing this thesis and providing useful inputs. I extend my thanks to Prof. Dr. Arantxa Fraile Rodríguez for reviewing this thesis and being the part of the committee.

The experiments at the X-treme beamline would not have been successful without crucial help from the present and former colleagues. Firstly, I thank Dr. Jan Dreiser "Super Cool" for sharing his experience and explaining basic physics for the experimental setup and in general. He was super helpful in using the STM and the sharing the knowledge of the sample preparation chamber. Secondly, I would like thank Stefan Zeugin "Superman of beamline" for constant technical support before and during the beam time. He designed the electrical contacts

on the Omicron plates for easier switching of samples *in-situ* and fixing the end-station/sample preparation chamber from time to time. Special thanks to Jakoba Heidler, Michal Studniarek and Niéli Daffé for their constant support during beam time and enthusiastic participation in the discussions on several topics.

I am grateful to Dr. Eugenie Kirk for growing uncountable samples (calibrating the thickness of CoFeB), SQUID measurements and for the reviewing this thesis very precisely. I also thank Dr. Anna Suszka for training me in using the sputtering machine and Dr. Nicholas Bingham for training me to use the SQUID equipment. Special thanks to Milan and Stefan for providing the BSTO and BTO thin films. I also thank, Rolf for allocating time for AFM.

I feel very lucky for being the part of MM group and has always been a pleasure to have MM team around. Thank you, Jaianth for being the part of my project and for helping me during the beam time. I thank Mahesh for your alacrity and sharing your knowledge both scientifically and technically. Many thanks to Dr. Armin Kleibert for helping in the measurements at the SIM beamline and for setting up the small XMCD chamber. Thank you, Ludovic for your help during the beam time. I extend my gratitude to Pascal Schifferle and Patrick Ascher " The Saviors" of the MM group. I also thank Dr. Urs Staub for your enthusiasm and constructive criticism during the science talks and 5 min presentations. Thank you, Dr. Carlos Vaz for providing useful insights to the results. I specially thank Martina Füglister and Charlotte Heer for completing all the formalities at PSI and making life easier at PSI. I would like to thank David (conference partner), Tanya, Nazaret, Zeh, Sergii, Martin (Decker and Schön), Manuel and Porer for your support and making my stay unforgettable time at PSI and outside.

I acknowledge Ursina for being supportive, understanding and being patient during my thesis writing and also like to thank my Badminton Club Vindonissa for the fun and stress relieving time after a hard day at work. I extend my thanks

to Dr. Durga Rao and Dr. Sudhakar for their constant support and sharing their exprience.

Last but not least, I thank my dear parents for their unconditional and everlasting support to me all life. This thesis is dedicated to my beloved late brother.

Curriculum Vitae

Full Name	Sridhar Reddy Avula Venkata
Date of Birth	June 19, 1988
Place of Birth	Hyderabad, India
Address	Dahlienweg 8, CH-5210, Windisch, Switzerland

Education and Training

2014-2018 **Doctoral Studies** at University of Basel (carried out at the Paul Scherrer Institute, Villigen). Supervised by Dr. Cinthia Piamonteze and Prof. Dr. Frithjof Nolting.

2011-2014 **Master of Science** (Material Science and Engineering), University of Kiel, Kiel (Germany).

2012-2013 **Research Assistant** (Nano-scale magnetic domains, University of Kiel) under Prof. Dr. Jeffrey McCord.

2010-2011 **Process Engineer** at Vedanta Aluminum Limited, Odhisa (India).

2006-2010 **Bachelor of Engineering** (Materials Engineering), Malaviya National Institute of Technology (NIT), Jaipur (India).

Conferences and Schools

August 2017	Swiss Physical Society, Geneva (talk).
April 2017	Intermag, Dublin (talk).
August 2016	Joint European Magnetic Symposia (JEMS), Glasgow (poster).
July 2016	Vacuum Ultraviolet and X-ray Physics (VUVX), Zürich (poster).
June 2016	Swiss NanoConvention, Basel (poster).
August 2014	PSI summer school, Zug.
July 2014	Swiss Physical Society, Fribourg.

Publications

Published in peer-reviewed journals

(i) Study of magneto-electric coupling between ultra-thin Fe films and PMN-PT using X-ray magnetic circular dichroism; **S. R. V. Avula**, J. Heidler, J. Dreiser, J. Vijayakumar, L. Howald, F. Nolting and C. Piamonteze; Journal of Applied Physics **123**, 064103 (2018).

(ii) Interplay of Fe and Tm moments through the spin-reorientation transition in $TmFeO_3$; U. Staub, L. Rettig, E. M. Bothschafter, Y. W. Windsor, M. Ramakrishnan, **S. R. V. Avula**, J. Dreiser, C. Piamonteze, V. Scagnoli, S.Mukherjee, C. Niedermayer, M. Medarde, E. Pomjakushina; Physical Review B **96**, 174408 (2018).

(iii) Magnetic properties of strained multiferroic $CoCr_2O_4$: a soft X-ray study; Y. W. Windsor, C. Piamonteze, M. Ramakrishnan, A. Scaramucci, L. Rettig, J. A. Huever, E. M. Bothschafter, A. Albreca, **S. R. V. Avula**, B. Noheda and U. Staub; Physical Review B **95**, 224413 (2017).